Hierarchical Multiscale Adaptive Variable Fidelity Wavelet-based Turbulence Modeling with Lagrangian Spatially Variable Thresholding

by

Alireza Nejadmalayeri

B.S., Amirkabir University of Technology (Tehran Polytechnic), 1999

M.S., Wichita State University, 2007

A thesis submitted to the

Faculty of the Graduate School of the

University of Colorado in partial fulfillment

of the requirements for the degree of

Doctor of Philosophy

Department of Mechanical Engineering

2012

This thesis entitled:
Hierarchical Multiscale Adaptive Variable Fidelity Wavelet-based Turbulence Modeling with Lagrangian Spatially Variable Thresholding
written by Alireza Nejadmalayeri
has been approved for the Department of Mechanical Engineering

_____

Prof. Oleg V. Vasilyev

_____

Prof. Gregory Beylkin

_____

Prof. Henry Tufo

_____

Prof. Kurt Karl Maute

_____

Prof. Alireza Doostan

Date _____

The final copy of this thesis has been examined by the signatories, and we find that both the content and the form meet acceptable presentation standards of scholarly work in the above mentioned discipline.

Nejadmalayeri, Alireza (Ph.D., Mechanical Engineering)

Hierarchical Multiscale Adaptive Variable Fidelity Wavelet-based Turbulence Modeling with Lagrangian Spatially Variable Thresholding

Thesis directed by Prof. Oleg V. Vasilyev

The current work develops a wavelet-based adaptive variable fidelity approach that integrates Wavelet-based Direct Numerical Simulation (WDNS), Coherent Vortex Simulations (CVS), and Stochastic Coherent Adaptive Large Eddy Simulations (SCALES). The proposed methodology employs the notion of spatially and temporarily varying wavelet thresholding combined with hierarchical wavelet-based turbulence modeling. The transition between WDNS, CVS, and SCALES regimes is achieved through two-way physics-based feedback between the modeled SGS dissipation (or other dynamically important physical quantity) and the spatial resolution. The feedback is based on spatio-temporal variation of the wavelet threshold, where the thresholding level is adjusted on the fly depending on the deviation of local significant SGS dissipation from the user prescribed level. This strategy overcomes a major limitation for all previously existing wavelet-based multi-resolution schemes: the global thresholding criterion, which does not fully utilize the spatial/temporal intermittency of the turbulent flow. Hence, the aforementioned concept of physics-based spatially variable thresholding in the context of wavelet-based numerical techniques for solving PDEs is established. The procedure consists of tracking the wavelet thresholding-factor within a Lagrangian frame by exploiting a Lagrangian Path-Line Diffusive Averaging approach based on either linear averaging along characteristics or direct solution of the evolution equation. This innovative technique represents a framework of continuously variable fidelity wavelet-based space/time/model-form adaptive multiscale methodology. This methodology has been tested and has provided very promising results on a benchmark with time-varying user prescribed level of SGS dissipation. In addition, a longtime effort to develop a novel parallel adaptive wavelet collocation method for numerical solution of PDEs has been completed during the course of the current work. The scalability and speedup studies of

this powerful parallel PDE solver are performed on various architectures. Furthermore, Reynolds scaling of active spatial modes of both CVS and SCALES of linearly forced homogeneous turbulence at high Reynolds numbers is investigated for the first time. This computational complexity study, by demonstrating very promising slope for Reynolds scaling of SCALES even at constant level of fidelity for SGS dissipation, proves the argument that SCALES as a dynamically adaptive turbulence modeling technique, can offer a plethora of flexibilities in hierarchical multiscale space/time adaptive variable fidelity simulations of high Reynolds number turbulent flows.

Dedication

To the turbulence community.

Acknowledgements

I express my sincere gratitude to the National Science Foundation for supporting me in my graduate studies.

Appreciation of the everlasting help and support of my beloved devoted parents, wife, and brothers is beyond words.

I would like to eternally thank my advisor, Professor Oleg V. Vasilyev, for bringing me into the small club of developers of wavelet-based turbulence modeling methodologies. I have not heard of any PhD advisor, who offers their PhD student to work long distance for two years. I am not sure how to acknowledge this extreme level of trust in me.

I would like to give a special thanks to Professor Gregory Beylkin for his great scientific and academic insights; from whom I learned one of the most insightful educational doctrine I have been exposed in my longtime academic life. I am also so thankful of my other committee members, Professor Henry Tufo, Professor Kurt Karl Maute, and Professor Alireza Doostan for all their help, support and effort.

I am extremely grateful for the extraordinary help and support of Mrs. Sharon E. Anderson, graduate advisor of the department of mechanical engineering. Her gracious style of assistance to facilitate the difficulties is unique. Her friendly chats would not be easy to find elsewhere.

I express my special thanks to my colleague, Dr. Alexei Vezolainen, for all his help and support. I also thank my other colleagues in Professor Vasilyev's group, Professor Shanon M. Reckinger for all her passion during dark days of debugging the parallel code, Eric Brown-Dymkoski for his frequent English language assistance and very long political debates, Scott Reckinger, Christopher

M. Bonilha, Nurlybek Kasimov, and Mikael Ian Pryor: thank you all for the discussions and help, the lab nights and days without you all could be miserable.

I am very pleased with all assistance of the Research Computing facilities and Janus supercomputer administrators and staffs at the University of Colorado at Boulder.

Contents

Chapter

Tables

Table

Figures

Figure

Chapter 1

Introduction

Humorous fable by Horace Lamb, British physicist and applied mathematician, in 1932 just two years before his death in 1934 goes as follows: "I am an old man now, and when I die and go to heaven there are two matters on which I hope for enlightenment. One is quantum electrodynamics, and the other is the turbulent motion of fluids. And about the former I am rather optimistic."

In the words of the legendary Nobel Prize-winning physicist, Richard Feynman, "Turbulence is the last great unsolved problem of classical physics."

George Papanicolaou from Stanford University, in an interview with Science Watch correspondent Gary Taubes, to answer the question, "Turbulence theory has not changed much in 30 years. Why is that? Why did Feynman call it the last great unsolved problem?" said: "Simply, turbulence is very hard. Every hard problem in classical physics finds itself embedded in turbulence. It is nonlinear, chaotic, stochastic. And there is no separation of scales – you must deal with a very large number of scales of irregularities. It's just a mess. In most other physics problems, you can get control by reducing them to simpler problems that you can understand. You can separate scales, for instance, and determine that certain scales are not important. You can limit the phenomena. Or perhaps the inhomogeneity, the chaotic behavior, is not there all the time, so you can somehow approach it. In turbulence all these things happen at once, and you don't know how to separate them out."

Papanicolaou still hopes he will be able to "find a way to create numerical computational methods that really use theoretical insight." He continued "One really interesting problem is to

think of clever ways to make numerical calculations that really straddle many scales. So far the numerical calculations have been rather straightforward – direct numerical calculation: write down the equations, put them on the computer, solve them. There have to be more intelligent ways of approaching this, to put more insight into the computer modeling. In the next 10 or 20 years, that's what's going to happen. The computational schemes are going to become increasingly intelligent, more adaptive. We are going to put into computer code the ability to recognize its environment and adapt, to become more efficient, and to be guided by the theory. The scant theory that exists right now is not employed in any intrinsic way when you use a computer to help make the problem more efficient. For turbulence it would be enormously important to be able to do that."

According to Marcel Lesieur [28]: "Turbulence is a dangerous topic which is often at the origin of serious fights in the scientific meetings devoted to it since it represents extremely different points of view, all of which have in common their complexity, as well as an inability to solve the problem. It is even difficult to agree on what exactly is the problem to be solved."

Lesieur schematically categorized the opposing points of view advocated during last 30 years into 3 communities as follow: 1) **Statistical**: tried to model the evolution of averaged quantities of the flow. This community, which had followed the glorious trail of Taylor and Kolmogorov, believed in the phenomenology of cascades, and strongly disputed the possibility of any coherence or order associated to turbulence; 2) **Coherence among Chaos**: considered turbulence from a purely deterministic point of view, by studying either the behavior of dynamical systems, or the stability of flows in various situations. Experimentalist and computer simulators who sought to identify coherent vortices in flows were also associated to this community; 3) **Emergence of third point of view** – with the concepts of renormalization group theory, multifractality, mixing, and Lagrangian approaches – pushed by physicists, has made the existence of the first two camps less clear.

This "very hard" (in words of Papanicolaou) and "dangerous" (according to Lesieur) topic by and large has been the center of attention of scientific-computing society and numerical-scheme developers community, although not all the attempts have made precise attention to even a few

existing scant theories. The goal of this work is to try to propose improvement techniques in an attempt to construct a numerical scheme, which address all aforementioned challenges: mainly to distinguish different scales and to treat them in different consistent fashion while not forgetting even the ignored scales or better to say, being able to include even ignored scales within the same numerical framework in future works.

The high fidelity numerical techniques for computational simulation of turbulence are mainly categorized as Direct Numerical Simulation (DNS) and Large Eddy Simulation (LES). Direct Numerical Simulation [17] is the most accurate numerical approach for solving Navier-Stokes (N-S) equations using higher-order finite difference/spectral schemes. DNS resolves all the physically meaningful scales within the limit of continuum mechanics from integral length scale all the way down to the smallest dissipative Kolmogorov length scale; however, its formidable computational complexity, $\sim Re^{\frac{9}{4}}$ only for spatial scales, makes it an impossible solution for real flow applications at least by end of this century or perhaps until quantum computers become a reality – "Every time a new supercomputer comes out, people immediately test what it will do for the turbulence problem [1]." It is worth stressing that the largest DNS to date is limited to 4096^3 grid points at $Re \approx 10^6$ performed in 2002 [49].

To tackle the DNS challenges, the notion of Large Eddy Simulation [10, 41] proposed in which the resolved large scales are simulated deterministically directly (akin to the DNS) while the interaction of large (resolved) with small (unresolved, modeled) scales are modeled. The scales distinction is obtained by applying low-pass frequency filters to the Navier-Stokes equations. Throughout the filtering process, filtered Navier-Stokes equations have more unknowns than number of equations and hence Sub-Grid Scale (SGS) models close the system via modeling the SGS stresses tensor. Contrary to Reynolds Averaged Navier-Stokes (RANS) in which nonlinear Reynolds stresses representing the effect of turbulence at all scales on the mean flow is modeled, only a part of the nonlinear interactions is modeled in LES by means of modeling the effect of small unresolved scales on large resolved ones. The modeled interactions involve small scales which are generally in the inertial-range and, as a result, have more universal character than flow-dependent large-scales. In spite of

its success in enormous degree-of-freedom reduction and distinction of small/large scales, in LES only the large-scales are resolved versus energy-containing-motions, which are of more importance. Besides, LES of wall-bounded flows is still expensive if no-slip boundary conditions (BCs) are used.

Issues like strong temporal/spatial intermittency, localized small structures in spatial/time space, and large range of spatial scales (Integral-scale / Kolmogorov-scale: $\frac{L}{\eta=\sqrt[4]{\nu^3/\varepsilon}}$) require the need for multi-resolution schemes in turbulence simulations among which wavelet-based techniques are strong candidates due to the prominent wavelet properties including: windowed transform property (temporal/spatial localized change of scale); intrinsic adaptiveness of these schemes simply by switching on/off wavelet coefficients; signal de-noising; existence of fast transform; capability of identification of coherent structures (signature-recognition property); and capturing multiscale (multi-resolution) character of turbulence. Based on these outstanding properties, the idea of using wavelets in turbulence was proposed for the first time by Marie Farge [13].

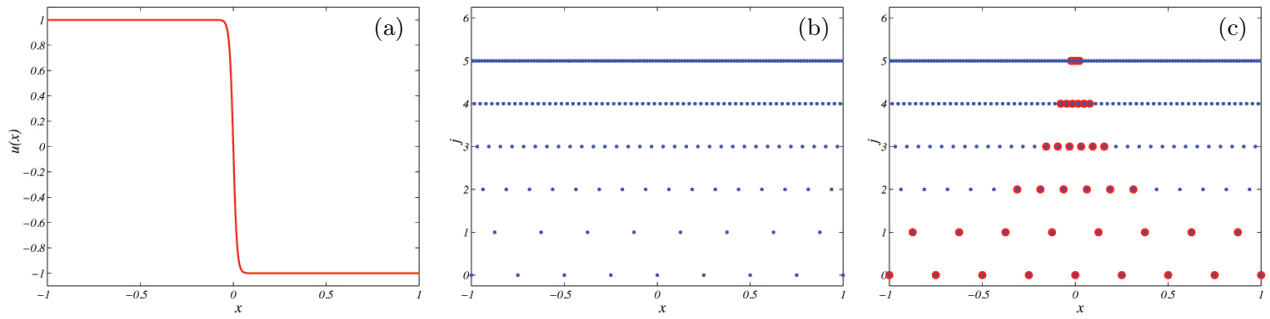

Figure 1.1: Schematic of Wavelet Threshold Filter [45]: (a) A hyperbolic tangent function; (b) Wavelet coefficient locations; (c) Wavelet-threshold filter locations.

The way wavelet transform works in general is to decompose a function, e.g. Figure 1.1(a), into wavelet-coefficients and wavelet-scaling-functions on different level of resolution at different locations on a dyadic grid, e.g. Figure 1.1(b). The way that wavelet-thresholding-filter works is to keep only the grid-points corresponding to the wavelet-coefficients above a priori defined thresholding factor, e.g. Figure 1.1(c), and there is no limitation on thresholding-factor at all, which is an arbitrary non-dimensional positive real-value scalar. The error of this filtering scales as thresholding-factor.

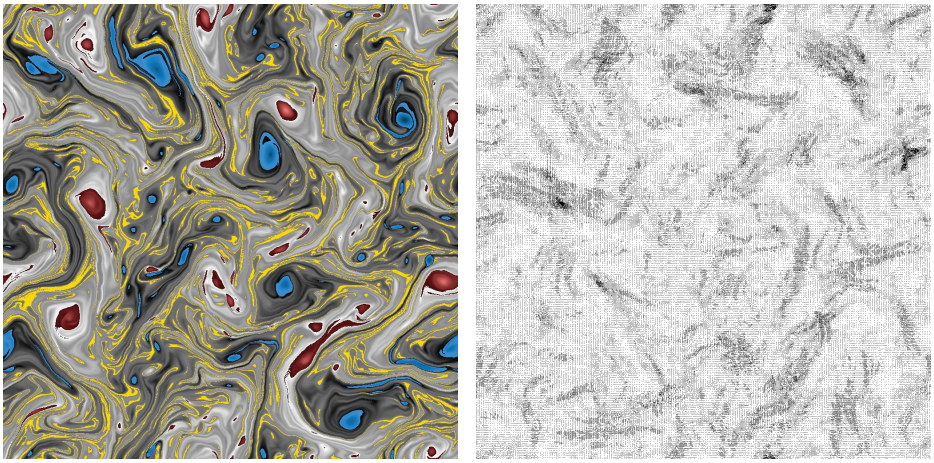

(a) Vorticity (b) Active wavelet locations

Figure 1.2: Wavelet transform of the Vorticity field. Courtesy of Marie Farge and Kai Schneider [14].

A very insightful and artistic illustration by Farge and Schneider [14], showed that by transforming the vorticity field into wavelet space, it can be realized that the high-concentration of active-wavelets are appeared only at few spatial locations, Figure 1.2. This illustrates the astonishing wavenumber compression, which is the first and most prominent beauty of wavelets in turbulence. In addition to compression, wavelet-threshold filtered velocity field corresponds to a wider range of wavenumbers compared with Fourier-cutoff filtered velocity field, Figure 1.3. That is because of the fact that each wavelet level (scale) corresponds to a range of wavenumbers, Figure 1.4. This implies the second major advantage of wavelets in turbulence, which is the multi-resolution nature of the wavelet-based filters.

The family of wavelet based turbulence models is mainly categorized into Wavelet based DNS (WDNS), Coherent Vortex Simulation (CVS), and Stochastic Coherent Adaptive Large Eddy Simulation (SCALES). WDNS – proposed for the first time by Fröhlich and Schneider [20] – is in fact an adaptive-DNS, where the wavelet-based numerical methods are used to solve the wavelet-filtered Navier-Stokes equations without any model with a sufficiently small threshold in order to ensure that the ignored-scales are not significant. As a result of wavelet filtering and due to

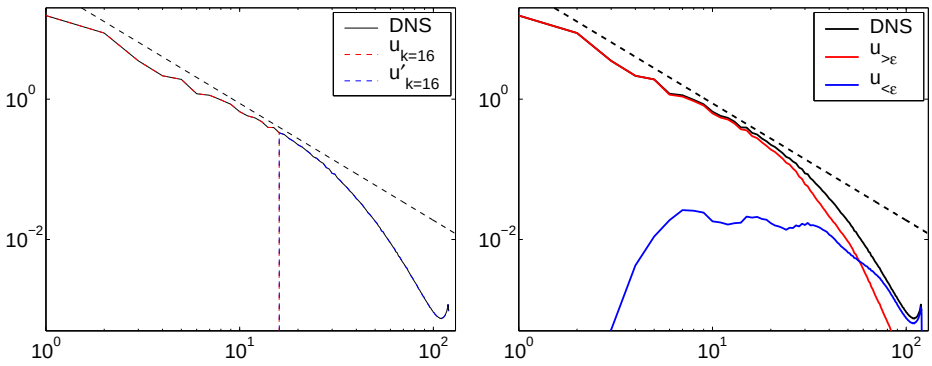

(a) Fourier Cutoff Filter (b) Wavelet Threshold Filter

Figure 1.3: Filtered DNS data on 256^3 grid at $Re_\lambda \approx 168$. Courtesy of Daniel E. Goldstein [24].

compression property of wavelets, the number of DOF (degree-of-freedom) is reduced compared with DNS using conventional approaches; however, still due to small threshold, it is still computationally very expensive and impractical for real high Reynolds number flow applications: the 2D spatial computational complexity scales as $Re^{\frac{7}{10}}$ compared with Re for non-adaptive computation [27].

Coherent Vortex Simulation (CVS) – proposed by Farge et al. [15] – is based on the idea that coherent modes are the ones, which are mostly responsible for the evolution of the turbulence as well as turbulent energy cascade and the fully developed turbulence is made of: 1) an organized coherent part; and 2) a random incoherent part. It was observed that by filtering the vorticity field using orthogonal wavelet bases with an ideal threshold level, the probability density function (PDF) of the unresolved filed is of the form of PDF of Gaussian white noise for homogeneous turbulence. Therefore, CVS (wavelet-filtered vorticity with an ideal threshold) is an approach to decompose the flow into deterministic and stochastic fields. Hence, in CVS the coherent-structures (the wavelet de-noised vorticity-field) are simulated directly while neglecting the effect of the incoherent-structures, since they provides no turbulent-dissipation.

CVS achieves a significant compression compared with DNS; however, number of remaining active modes are still large and the process of calculating the optimal threshold at each time-step is quite expensive since it requires the variance of the incoherent modes. Furthermore, the wavelet-

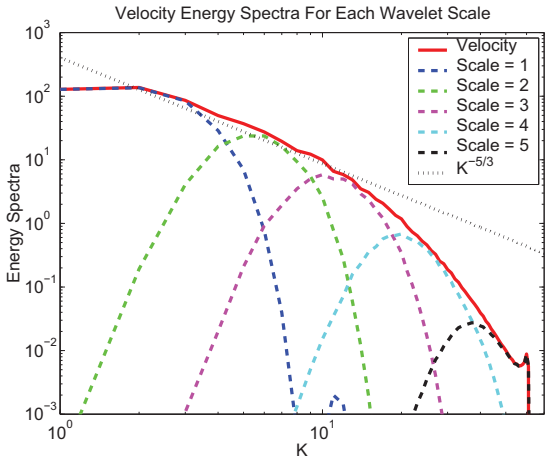

Figure 1.4: Velocity Energy Spectra For Each Wavelet Scale. Courtesy of Daniel E. Goldstein [24].

based coherent vortex extraction for inhomogeneous turbulence is still an open question [40].

Stochastic Coherent Adaptive Large Eddy Simulation (SCALES) – proposed by Goldstein and Vasilyev [24] – is a recent wavelet-based methodology for numerical simulations of turbulent flows that resolves energy containing turbulent motions using wavelet multi-resolution decomposition and self-adaptivity. In the original formulation of this technique, the extraction of the most energetic structures is achieved using wavelet thresholding filter with a priori prescribed threshold level.

SCALES is a methodology, which inherits the advantages of both Coherent Vortex Simulations (CVS) [15] and Large Eddy Simulation (LES), while overcoming the shortcomings of both. Unlike coherent/incoherent and large/small structures decomposition in CVS and LES respectively, in SCALES the separation is between more and less energetic structures. Therefore, unlike CVS, the effect of background flow can not be ignored and needs to be modeled similarly to LES. Furthermore, the filtering and consequently, the subgrid scale (SGS) model are benefited from wavelet nonlinear multiscale band-pass filter, which depends on instantaneous flow realization. As a result of using SGS models, the number of degrees-of-freedom is smaller than CVS and consequently a higher grid-compression can be achieved, Figure 1.5.

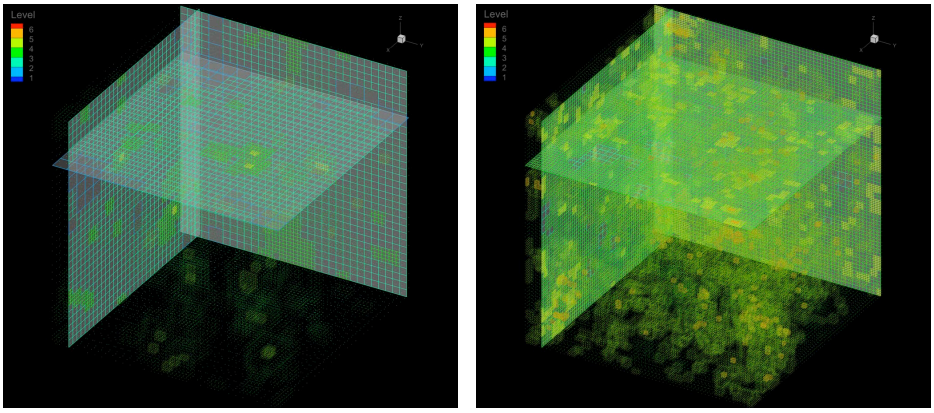

(a) SCALES (b) CVS

Figure 1.5: A visualization to show that even in CVS, which matches the DNS spectra, just at few locations, grid is adapted to the highest level of resolution while in SCALES most of the time, the highest level of resolution is one less than the maximum level of resolution.

In SCALES, the wavelet-filtered Navier-Stokes equations are solved using the adaptive wavelet collocation method (AWCM) [45], which is based on the second-generation bi-orthogonal wavelet – a compactly supported and symmetric scheme. Unlike the CVS with its original formulation, which is based on vorticity equations, SCALES similar to LES solves the velocity field and it was proved that using bi-orthogonal wavelets, the PDF of the modeled portion of the SGS (wavelet-filtered out) velocity field is of the form of Gaussian white noise PDF.

This fraction of the less energetic structures is in fact a small part of SGS field. That is to say, the velocity field is initially decomposed to more and less energetic structures by means of wavelet-threshold filter. The "deterministic most energetic coherent structures" are solved directly using AWCM. However, the unresolved field in not absolutely an incoherent stochastic field with no effect on the resolved field and as a result, it needs to be modeled. Again, using wavelet-threshold filter, the unresolved field is decomposed into two kinds of modes: the minority "deterministic coherent SGS modes"; and the "majority stochastic incoherent SGS modes". The effect of these two modes on the resolved field can be modeled by "deterministic SGS models" and "stochastic SGS models" respectively.

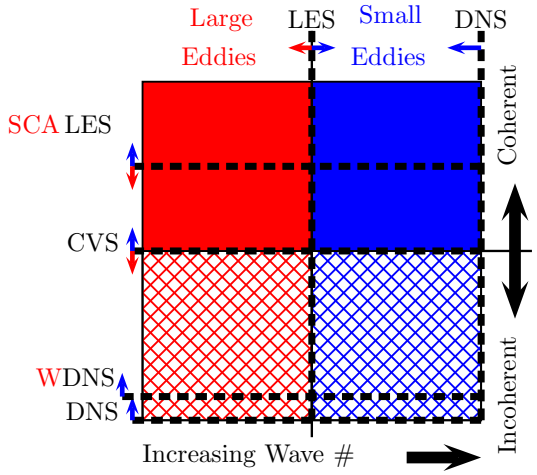

Figure 1.6: Coherency Diagram: At-a-Glance Comparison of DNS, WDNS, CVS, SCALES, LES. Courtesy of Daniel E. Goldstein [24].

The overall at-a-glance comparison of these wavelet-based turbulence modeling techniques – WDNS, CVS, SCALES – and the conventional non-wavelet-based methods – DNS, LES – can be easily illustrated in Coherency Diagram [24], Figure 1.6, on which the wavenumber increases in the horizontal direction and the wavelet-threshold-filter threshold-parameter increases in the vertical direction upward. It is clearly shown that the CVS and LES are limiting case of Coherent/Incoherent and Large/Small structures distinctions, while in SCALES in a more relaxed fashion, both resolved and unresolved structures are not limited to these separations. Therefore, while not being limited to homogenous-turbulence – as is the case in CVS – with a very high grid-compression ratio, majority of important energetic structures are resolved and both coherent-deterministic and incoherent-stochastic unresolved modes can be modeled. This distinction is not anymore limited to the size of the structures – which is rather less informative – as it is the case in classical LES. Furthermore, resolved structures and the modeled eddies overlap over a range of wavenumbers together in order to ensure more realistic energy cascade.

1.1 Motivation

Ever since the emergence of the wavelet-based multi-resolution schemes for simulations of turbulence, there has been a major limitation for all wavelet-based techniques: the use of a priori defined global (both in space and time) thresholding-parameter. In this work the robustness of the SCALES approach is further improved by exploring the spatially and temporally variable thresholding strategy, which allows more efficient representation of intermittent flow structures.

This methodology provides an automatic transition among WDNS, CVS, and SCALES, which represents a framework of continuously variable fidelity wavelet-based space/time/model-form adaptive hierarchical multiscale methodology. This work aims to develop such a uniform approach, i.e. a single computational framework, for multiscale turbulence modeling.

Even with enormous compression achieved by wavelets, i.e. 99%, still at high resolutions, the number of active degrees-of-freedom are beyond the capability of the most advanced CPU and memory configurations: for instance one cannot fit 1% of $2048^3 > 85$ millions DOF into any available CPU. All in all, highly adaptive multi-resolution techniques like SCALES are not the replacement of the need for highly scalable petascale algorithms but they are necessary to utilize the existing computational power more robustly. Therefore, completion of a long-time effort to parallelize an adaptive wavelet-based PDE solver is another essential component of the current effort.

The compression accomplished by wavelets has been proved by the existing efforts using CVS and SCALES and it is widely believed and accepted within the turbulence community; however, no work has yet proposed exactly how the number of active wavelets (DOFs) scale as Reynolds number increases. That is to say, it is unknown that how quantitatively the wavelet-based multi-resolution techniques improve the Reynolds scaling of spatial modes in DNS. Hence, the second major objective of this study is to use the aforementioned proposed wavelet-based parallel PDE solver and the spatially variable thresholding methodology in order to attain the Reynolds scaling of number of active spatial modes in 3-D linearly forced homogeneous turbulence – i.e. by taking into account

the spatial intermittency – using both CVS and SCALES. In addition to compression – which is the most prominent strength of wavelets in turbulence, due to the other wavelets properties and the dynamically adaptive mechanism, the hierarchical multiscale adaptive variable fidelity methodology developed by this work, provides a unique tool in controlling the flow-physics information, which is desired to be modeled. The current study investigates the effect of the fidelity of simulation on the Reynolds scaling of this modified SCALES in order to demonstrate how wavelet based methods can resolve more flow-physics yet using profoundly smaller number of spatial modes compared with the other techniques.

1.2 Organization

This dissertation is organized as follows. Chapter 2 addresses the background of SCALES governing equations and the AWCM for solving PDEs. In Chapter 3, the motivation, derivation and validation of the spatially variable thresholding are discussed. Chapter 4 presets the idea of "hybrid wavelet-based multiscale adaptive variable fidelity turbulence modeling" based on spatio-temporal field for the threshold-level of the WTF. Chapter 5 explains in detail the scalability studies of a parallel adaptive wavelet collocation technique. The Reynolds scaling of spatial modes of both Coherent Vortex Simulations and Stochastic Coherent Adaptive Large Eddy Simulations of linearly forced homogeneous turbulence at high Reynolds numbers Reynolds are addressed in Chapter 6. Finally, a concise overview of the most notable achievements throughout the course of this numerical effort as well as discussion of envisioned ideas for the future work are given in Chapter 7.

It is worth clarifying that each chapter ends with synopsis of in-progress efforts and perspective of future endeavors. Also, each chapter starts with a small redundant introduction as to make each chapter self consistent and comprehensive.

Chapter 2

Background

2.1 Stochastic Coherent Adaptive Large Eddy Simulation

The properties of wavelet transform, namely the ability to identify and efficiently represent temporal/spatial coherent flow structures, self-adaptiveness, and de-noising, have made them attractive candidates for constructing multi-resolution variable fidelity schemes for simulations of turbulence [40]. To address the shortcomings of LES and CVS, SCALES uses a wavelet thresholding filter to dynamically resolve and track the deterministic most energetic coherent structures while the effect of less energetic unresolved modes is modeled. The unresolved less energetic structures have been shown to be composed of a minority of deterministic coherent modes that dominate the total SGS dissipation and a majority of stochastic incoherent modes that, due to their decorrelation with the resolved modes, add little to the total SGS dissipation [8, 24]. In the current implementation, similar to the classical LES, only the effect of coherent part of the SGS modes is modeled using deterministic SGS models. The use of stochastic SGS models to capture the effect of the incoherent SGS modes will be the subject of future investigations. The most significant feature of SCALES is the coupling of modeled SGS dissipation and the computational mesh: more grid points (active wavelets) are used for SGS models with lower levels of SGS dissipation. In other words, the SCALES approach compensates for inadequate SGS dissipation by automatically increasing the local resolution and, hence, the level of resolved viscous dissipation. Another noticeable feature of the SCALES method is its ability to match the DNS energy spectra up to the dissipative wavenumber range using considerably less degrees of freedom.

2.2 Wavelet Thresholding Filter

In the wavelet-based approach to the numerical simulation of turbulence the separation between resolved energetic structures and unresolved residual flow is obtained through nonlinear multiresolution wavelet threshold filtering (WTF). The filtering procedure is accomplished by applying the wavelet-transform to the unfiltered velocity field, discarding the wavelet coefficients below a given threshold (ϵ) and transforming back to the physical space. This results in decomposition of the turbulent velocity field into two different parts: a coherent more energetic velocity field and a residual less energetic coherent/incoherent one, i.e., $u_i = \overline{u}_i^{>\epsilon} + u_i'$, where $\overline{u}_i^{>\epsilon}$ stands for the wavelet-filtered velocity at level ϵ

$$\overline{u}_i^{>\epsilon}(\mathbf{x}) = \sum_{\mathbf{l}\in\mathcal{L}^1} c_{\mathbf{l}}^1 \phi_{\mathbf{l}}^1(\mathbf{x}) + \sum_{j=1}^{+\infty} \sum_{\mu=1}^{2^n-1} \sum_{\substack{\mathbf{k}\in\mathcal{K}^{\mu,j} \\ |d_{\mathbf{k}}^{\mu,j}| > \epsilon \|u_i\|_{\mathrm{WTF}}}} d_{\mathbf{k}}^{\mu,j} \psi_{\mathbf{k}}^{\mu,j}(\mathbf{x}), \tag{2.1}$$

where $\psi_{\mathbf{k}}^{\mu,j}$ are wavelets of family μ at j level of resolution, $d_{\mathbf{k}}^{j}$ are the coefficients of the wavelet decomposition, and $\phi_{\mathbf{l}}^1$ are scaling functions at the first level of resolution.

The key-role in the wavelet-filter definition is clearly played by the non-dimensional relative thresholding level ϵ that explicitly defines the relative energy level of the eddies that are resolved and, consequently, controls the importance of the influence of the residual field on the dynamics of the resolved motions. This work explores the use of spatially and temporary varying thresholding level ϵ, which follows the evolution of the turbulent velocity field.

2.3 Adaptive Wavelet Collocation Method

Depending on whether taking full or partial advantage of wavelet analysis (e.g. multiresolution properties, wavelet compression, detection of localized structures and subsequent use for grid adaptation, fast wavelet transform/inverse-transform, wavelet-based interpolation, active error control), the wavelet-based PDE-solver algorithms can be categorized in different ways [40]. Here the focus is on "pure wavelet methods" where wavelets are used either directly for discretizing the underlying PDEs or the properties of wavelets are used for grid adaptation, preconditioning

or inversion of the operators and fast interpolation [46]. The pure wavelet methods are mainly categorized as "Adaptive Wavelet Galerkin Methods" and "Adaptive Wavelet Collocation Methods". The main difference is that former solve the problem in wavelet coefficient space but the later solve the problem in physical space on an adaptive computational grid.

In Adaptive Wavelet Galerkin Methods, the unknown variable u is decomposed into a wavelet series given by Equation (2.1). Substituting this approximation of considering only coefficients with absolute value above a given threshold into the underlying differential equation(s) and requiring that the residual vanishes with respect to test functions results in a system of equations for the unknown wavelet coefficients $d_{\mathbf{k}}^{\mu,j}$ and scaling function coefficients $c_{\mathbf{l}}^{1}$, which can be solved at each time step [40]. The test functions can be either dual wavelets and scaling functions for bi-orthogonal wavelets, wavelets and scaling function for orthogonal wavelets, or vaguelettes [40]. The grid adaption strategy is based on analyzing the wavelet coefficients $d_{\mathbf{k}}^{\mu,j}$ and the adjacent zone, which will be explained later. Using this algorithm, the approximation of 2.1 automatically tracks the solution in space and scale. Boundary conditions can be imposed using either boundary adapted basis functions or imposing them afterwards, as done for spectral methods using the tau method [40].

In Adaptive Wavelet Collocation Methods, the differential equations are solved in physical space on an adaptive computational grid. This prevents the major difficulties associated with adaptive wavelet Galerkin methods: challenging treatment of nonlinearities and general boundary conditions. The evaluation of the nonlinear terms in adaptive wavelet collocation methods is performed in the physical domain similar to pseudo-spectral methods. The grid adaptation in wavelet collocation methods is done similarly to other wavelet-based methods. The only difference is that at the end of each time step (or iteration) an additional wavelet transform is performed for the analysis of wavelet coefficients and construction of the adjacent zone. Once the approximation (2.1) is constructed, the computational grid is obtained based on one-to-one correspondence between wavelets and collocation points: a collocation point is kept if the corresponding wavelet is kept in the approximation (2.1). The implementation of wavelet collocation methods used in the current study uses a finite difference approximations of the wavelet-based interpolant: namely taking ad-

vantage of wavelet interpolation properties and evaluate spatial derivatives using finite difference approximation on either fixed stencils using a ghost point approach or variable stencils that use values at the nearest grid points. This implementation utilizes "second generation wavelets", which are constructed in the spatial domain rather than Fourier space and as a result they can be custom designed for the complex geometries and nonuniform sampling intervals. The current implementation exploits the second-generation lifted interpolating wavelets where the Lagrange polynomials are used to construct local polynomials $P_{2N-1}(x)$ of order $2N-1$, which uses $2N$ closest adaptive even points. The spatial derivatives can be taken up to $2N^{\text{th}}$ order.

In pure wavelet methods, adaptation of the wavelet expansion is based on the analysis of the wavelet coefficients of the approximation (2.1). The wavelet thresholding criterion is adequate for representing a function or a field with fewest degrees of freedom, while still retaining a good approximation. However, for solving PDEs, it is imperative to ensure that the wavelet basis or computational mesh is sufficient to approximate the solution throughout the time-integration step for the evolution problems or at the next iteration in the elliptic problems. This extended adaptation strategy for an evolution problem is illustrated in Figure 2.1, where solid circles indicate the positions of wavelets both in location (index i) and scale (index j). The locations of wavelets with significant coefficients kept in approximation (2.1) at time t are marked by the orange bell curve (significant wavelets are inside of the orange region). The second bell-shaped region on the right of the original one marks the locations of the significant wavelet coefficients at the end of the time integration, i.e., at $t + \Delta t$. In order to ensure the adequate approximation of the solution during time integration, the concept of a safety or an adjacent zone is introduced, which includes wavelets whose coefficients are or can possibly become significant during the period of time integration, when the grid remains unchanged. The safety zone is represented in Figure 2.1 by the red bell-shaped region. Most of the current wavelet adaptation techniques are based on this strategy. In the current implementation of adaptive wavelet collocation method (AWCM), a safety zones is added for each of the significant coefficients and the time-step is chosen such that the solution does not propagate outside of the safety zone. This safety zone includes neighboring wavelets at the same, one-or-more above (children),

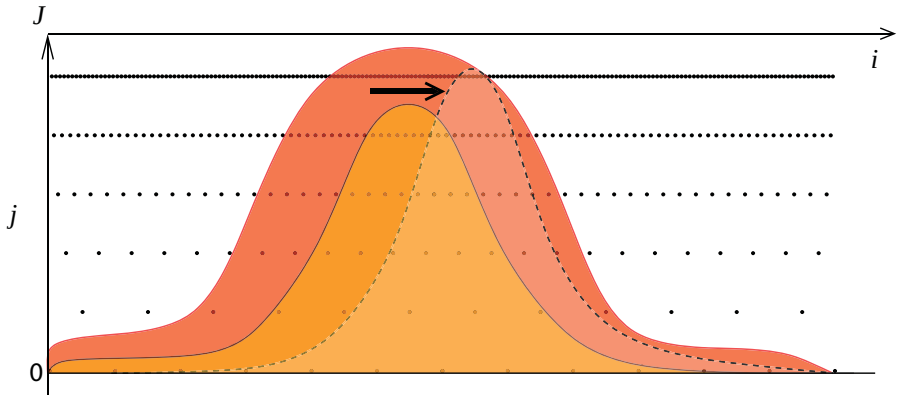

Figure 2.1: Illustration of the adjacent zone for adaptive wavelet methods in wavelet coefficient space with scale index j and position index i. Courtesy of Kai Schneider and Oleg V. Vasilyev [40]

and one-or-more below (ancestors) levels of resolution at each significant point. Therefore, it can be ensured that no energy at a given scale of resolution propagates outside the safety region. The thickness of the safety zone (number points added in each direction) determines the time interval during which the calculations can be carried out without modifying the computational grid [40]. This thickness is a user-defined control parameter. For computational efficiency, in general a safety zone, which includes only the immediate neighboring wavelets, is optimal.

2.4 Wavelet-Filtered Navier-Stokes Equations: SCALES Equations

By filtering the Navier-Stokes equations using wavelet threshold filtering, the following SCALES equations that govern the evolution of coherent energetic structures are obtained:

$$\partial_{x_i} \overline{u}_i^{>\epsilon} = 0, \tag{2.2}$$

$$\partial_t \overline{u}_i^{>\epsilon} + \overline{u}_j^{>\epsilon} \partial_{x_j} \overline{u}_i^{>\epsilon} = -\partial_{x_i} \overline{P}^{>\epsilon} + \nu \partial^2_{x_j x_j} \overline{u}_i^{>\epsilon} - \partial_{x_j} \tau^*_{ij} + Q\overline{u}_i^{>\epsilon}, \tag{2.3}$$

where $\overline{P}^{>\epsilon} = \frac{\overline{p}^{>\epsilon}}{\rho} + \frac{1}{3}\tau_{kk}$; $\tau_{ij} = \overline{u_i u_j}^{>\epsilon} - \overline{u}_i^{>\epsilon}\,\overline{u}_j^{>\epsilon}$ are the unresolved "SGS stresses" tensor that its deviatoric part $\tau^*_{ij} = \tau_{ij} - \frac{1}{3}\tau_{kk}\delta_{ij}$ needs to be modeled; $Q\overline{u}_i^{>\epsilon}$ is the linear forcing term [30], which is applied in the physical space over the whole range of wavenumbers; and the superscript $(\cdot)^{>\epsilon}$ denotes wavelet filtered quantities. The bar symbol in the notation of the pressure variable, $\overline{P}^{>\epsilon}$, does not imply the application of the WTF operator, but is used for consistency with the

other terms; the pressure term in the filtered momentum equation must be viewed as a Lagrange multiplier enforcing the incompressibility constraint since our WTF is not based on divergence-free wavelet basis. The SCALES equations are similar to the LES ones with the exception that the nonlinear multiscale band-pass wavelet filter, which depends on instantaneous flow realization, is used. The unresolved SGS stresses represent the effect of "unresolved less energetic deterministic coherent and stochastic incoherent eddies" on the "resolved more energetic coherent structures". In this study the localized kinetic-energy-based model [9] is exploited to close the filtered momentum equations. The SCALES methodology involving both the filtered momentum and the SGS energy equations is implemented by means of the adaptive wavelet collocation method [45], which is a multi-resolution adaptive scheme with $O(\mathrm{I\!D})$ computational cost, where $\mathrm{I\!D}$ is the number of active wavelets on a dyadic grid.

2.5 Localized Kinetic Energy based Model (LKM)

The localized SGS models like LKM, are based on the eddy-viscosity models assumption where turbulent viscosity depends on SGS kinetic energy contrary to the Smagorinsky model in which turbulent viscosity depends on the resolved rate of strain, $\overline{S}_{ij}^{>\epsilon}$. Hence the unknown unresolved "SGS stresses" tensor is approximated as:

$$\tau_{ij}^{*} \cong -2\nu_t \overline{S}_{ij}^{>\epsilon}. \tag{2.4}$$

In order to define the "turbulent eddy-viscosity" ν_t, one can assume the square root of SGS kinetic energy as the velocity scale and the wavelet-filter characteristic width Δ as the length scale:

$$\nu_t = C_\nu \Delta k_{\mathrm{sgs}}^{1/2}, \tag{2.5}$$

where C_ν is the turbulent eddy-viscosity model coefficient. As a result, the deviatoric part of the unresolved SGS stresses tensor which needs to be modeled is approximated as:

$$\tau_{ij}^{*} \cong -2C_\nu \Delta k_{\mathrm{sgs}}^{1/2} \overline{S}_{ij}^{>\epsilon}. \tag{2.6}$$

The SGS dissipation – rate of local-transfer of energy from energetic resolved eddies to unresolved structures – by definition obtained from τ^*_{ij} and $\overline{S}^{>\epsilon}_{ij}$:

$$\Pi = -\tau^*_{ij}\,\overline{S}^{>\epsilon}_{ij}\,. \tag{2.7}$$

Hence by replacing approximate (modeled) value for the the deviatoric part of SGS stress, SGS dissipation rate is approximated in terms of the SGS kinetic energy (SGS K.E.) as:

$$\Pi \cong C_\nu \Delta k_{\rm sgs}^{1/2} |\,\overline{S}^{>\epsilon}_{ij}\,|^2, \tag{2.8}$$

where resolved rate-of-strain tensor is defined as:

$$\overline{S}^{>\epsilon}_{ij} = \frac{1}{2}\left(\partial_{x_j}\overline{u}^{>\epsilon}_i + \partial_{x_i}\overline{u}^{>\epsilon}_j\right) \tag{2.9}$$

and the modulus of the rate-of-strain tensor is:

$$|\,\overline{S}^{>\epsilon}| = \left(2\,\overline{S}^{>\epsilon}_{ij}\,\overline{S}^{>\epsilon}_{ij}\right)^{1/2}. \tag{2.10}$$

The model transport equation for SGS K.E. is expressed as follows [23]:

$$\partial_t k_{\rm sgs} + \overline{u}^{>\epsilon}_j \partial_{x_j} k_{\rm sgs} = (\nu + \nu_t)\partial^2_{x_j x_j} k_{\rm sgs} - \tilde{\varepsilon}_{\rm sgs} + \Pi, \tag{2.11}$$

where SGS K.E. is defined as the difference between the wavelet filtered energy $\overline{k}^{>\epsilon}$ and the kinetic energy of the filtered velocity field $k_{\rm res}$:

$$k_{\rm sgs} = \overline{k}^{>\epsilon} - k_{\rm res} = \frac{1}{2}\left(\overline{u_i u_i}^{>\epsilon} - \overline{u_i}^{>\epsilon}\overline{u_i}^{>\epsilon}\right) \tag{2.12}$$

The SGS viscous dissipation by definition is:

$$\tilde{\varepsilon}_{\rm sgs} = \nu\left(\overline{\partial_{x_j} u_i \partial_{x_j} u_i}^{>\epsilon} - \partial_{x_j}\overline{u}^{>\epsilon}_i \partial_{x_j}\overline{u}^{>\epsilon}_i\right) = \overline{\tilde{\varepsilon}}^{>\epsilon} - \tilde{\varepsilon}_{\rm res}, \tag{2.13}$$

where $\tilde{\varepsilon}_{\rm res} = \nu\partial_{x_j}\overline{u}^{>\epsilon}_i \partial_{x_j}\overline{u}^{>\epsilon}_i$ is the resolved pseudo-dissipation and $\varepsilon_{\rm res} = 2\nu\,\overline{S}^{>\epsilon}_{ij}\,\overline{S}^{>\epsilon}_{ij}$ is resolved turbulent dissipation

Similar to the SGS stress model, the SGS viscous dissipation can be modeled using simple scaling arguments:

$$\tilde{\varepsilon}_{\rm sgs} = C_\varepsilon \Delta^{-1} k_{\rm sgs}^{3/2}. \tag{2.14}$$

This modeling procedure results in two dimensionless model coefficients (parameters): "Turbulent Eddy-Viscosity Model Coefficient" C_ν and "SGS Energy Dissipation Model Coefficient" C_ε. Based on previous numerical studies [9], for the sake of simplicity and saving computational resources, in the current effort, the model parameters are assumed to be priori prescribed constants as: $C_\varepsilon = 1.0$ and $C_\nu = 0.06$.

Chapter 3

Spatially Variable Thresholding: Framework for Adaptive Variable Fidelity Wavelet-based Models

Until now, not only SCALES but also all other wavelet-based turbulence modeling approaches and in general all wavelet-based methods for numerical solution of PDEs had a major limitation: the use of a priori defined global (both in space and time) thresholding-parameter for the wavelet-thresholding-filter. One of the main objectives of this work is to enhance the robustness of the SCALES approach even more by exploring the physics-based spatially and temporally variable thresholding strategy. The proposed spatially variable thresholding methodology is the key element of a more general wavelet-based hybrid adaptive variable fidelity turbulence modeling framework in order to fully utilize spatial/temporal intermittency of flow structures.

Previous studies, e.g. [25], demonstrated that in SCALES, the SGS dissipation is proportional to ϵ^2; therefore, one can enhance SCALES by exploiting spatially-varying ϵ based on local SGS dissipation $\Pi = -\tau_{ij}^* \overline{S}_{ij}^{>\epsilon}$. This implies that rate of local-transfer of energy from energetic-resolved-eddies to unresolved-less-energetic structures can be controlled by varying the thresholding-factor. Therefore, the idea is to locally vary ϵ wherever Π deviates from a priori defined goal-value. A decrease of the thresholding level results in the local grid refinement with subsequent rise of the resolved viscous dissipation, while an increase of ϵ coarsens the mesh resulting in the growth of the local SGS dissipation. However, in order to vary ϵ in a physically consistent fashion, it should follow the local flow structures as they evolve in space and time. This necessitates the Lagrangian representation of ϵ. Therefore, the continuously varying threshold level ϵ should be forced properly

in order to track the time-rate-of-change of ϵ within a material framework subjected to a spatial and temporal dependency of the velocity field. Differentiation with respect to time of the "statistical average of ϵ along the trajectory of a fluid particles" results in the evolution equation for ϵ based on the material derivative. Since the chaotic convective mixing can create high frequency modes in the threshold field and consequently lead to undesired small-scale fluctuations in the velocity field, an additional artificial diffusion term is added to the evolution equation. Therefore, the Lagrangian representation of ϵ is achieved using the Lagrangian path-line diffusive averaging approach [47]:

$$\partial_t \epsilon + \overline{u}_j^{>\epsilon} \partial_{x_j} \epsilon = -\text{forcing}_{\text{term}}(\mathbf{x}, t) + \nu_\epsilon \partial^2_{x_j x_j} \epsilon. \tag{3.1}$$

For the sake of efficiency, instead of solving Eq. (3.1) for the evolution of ϵ, the linear-interpolation along characteristics, similar to the idea of Meneveau et al. [32], can be used

$$\frac{1}{\Delta t}\left[\epsilon^{\text{new}}\left(\mathbf{x}, t+\Delta t\right) - \epsilon^{\text{old}}\left(\mathbf{x} - \overline{\mathbf{u}}^{>\epsilon}\Delta t, t\right)\right] = -\text{forcing}_{\text{term}}\left(\mathbf{x} - \overline{\mathbf{u}}^{>\epsilon}\Delta t, t\right). \tag{3.2}$$

The use of linear interpolation results in sufficient numerical diffusion, thus, eliminating the need for explicit diffusion. That is to say, the required physical diffusion is controlled either explicitly by the evolution equation approach directly or implicitly through the interpolation on the local resolution.

The proposed spatially variable thresholding strategy ensures that the wavelet threshold is not **a priori** prescribed but determined on the fly by desired "turbulence resolution" described in the following. The mechanism for the forcing term is as follows: The local fraction SGSD (FSGSD, $\mathcal{F}$) is defined as $\frac{\Pi}{\varepsilon_{\text{res}}+\Pi}$, where $\varepsilon_{\text{res}} = 2\nu\,\overline{S}_{ij}^{>\epsilon}\,\overline{S}_{ij}^{>\epsilon}$ is the resolved viscous dissipation. A prescribed level for the quantity of $\mathcal{F}$ is referred as desired "turbulence resolution", since it indicates the level to which one would like to resolve the most energetic structures and model the effect of unresolved structures on the resolved ones. It should be noted that the SGS kinetic energy is also proportional to the threshold-level, i.e. scales as ϵ^2, consequently, the ratio of $\frac{k_{\text{sgs}}}{k_{\text{res}}+k_{\text{sgs}}}$ could be also used to characterize how much the flow is resolved/modeled. However, since the energy spectrum decays with the increase of wave numbers, the SGS kinetic energy characterization of turbulence is not well suited for high Reynolds number flows, simply because it mostly based on large-scale contribution

and is not sensitive to the Reynolds number changes. The SGS dissipation characterization, on the other hand, is more objective measure, since dissipation spectrum increases with wavenumber and the changes in molecular viscosity and correspondingly Reynolds number would result in shifting the peak of the resolved dissipation. For that reason in this work, ϵ is adapted based on the ratio of dissipations rather than the ratio of kinetic energies of modeled and resolved structures. In addition, the SGS kinetic energy is not always available, while SGS and resolved dissipations are.

Based on this concept of the turbulence resolution, the idea of the forcing scheme is basically to maintain $\mathcal{F}$ at a priori-define desired "Goal", $\mathcal{G}$, value. In this work, two different simple linear feedback forcing methods are studied:

FT1 Controlling $\mathcal{F}$ at the goal-value $\mathcal{G}$ simply implies retaining Π at $\varepsilon_{\text{res}}\frac{\mathcal{G}}{1-\mathcal{G}}$. The first forcing type (FT1) is an attempt to implement this while normalizing the forcing term based on its time average:

$$\text{forcing}_{\text{term}}\left(\mathbf{x},t\right) = C_{\text{f}_\epsilon}\,\frac{\Pi - \varepsilon_{\text{res}}\frac{\mathcal{G}}{1-\mathcal{G}}}{\text{TAF}}\,\epsilon\left(\mathbf{x},t\right), \tag{3.3}$$

where TAF stands for the time average of the forcing, is the time average of $|\Pi - \varepsilon_{\text{res}}\frac{\mathcal{G}}{1-\mathcal{G}}|$. The forcing constant coefficient, C_{f_ϵ}, is intentionally set to 400 in order to make the time response of FT1 about three to four times faster than large eddy turnover time, which is discussed in the next section.

FT2 In this approach, the variations of $\mathcal{F}$ is controlled directly based on the goal-value in conjunction with a relaxation time parameter (time-scale), τ_ϵ,

$$\text{forcing}_{\text{term}}\left(\mathbf{x},t\right) = \frac{1}{\tau_\epsilon}\left(\frac{\Pi}{\varepsilon_{\text{res}}+\Pi} - \mathcal{G}\right)\epsilon\left(\mathbf{x},t\right). \tag{3.4}$$

Following the time-varying threshold studies [7], a time-scale associated to the characteristic rate-of-strain is chosen: $\tau_\epsilon^{-1} = \langle|\,\overline{S}_{ij}^{>\epsilon}\,|\rangle$.

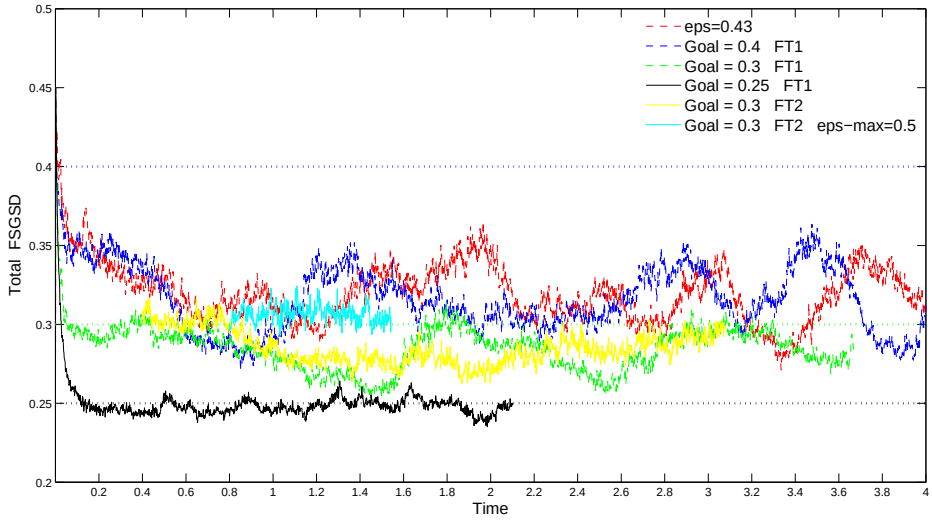

Figure 3.1: Time-history of total fraction SGSD, $\frac{\langle \Pi \rangle}{\langle \varepsilon_{\text{res}} \rangle + \langle \Pi \rangle}$.

3.1 Results

The proposed methodology has been tested [35] for linearly forced homogeneous turbulence [6] with linear forcing constant coefficient $Q = 6$ at $Re_\lambda \cong 72$ (Taylor micro-scale Reynolds number) using localized dynamic kinetic-energy-based SGS models [9, 6] on an adaptive grid with effective resolution of 256^3. Figure 3.1 demonstrates the results of this implementation for three different goal-values $(0.4, 0.3, 0.25)$ for the local FSGSD with the upper and lower bound for epsilon set as 0.2 and 0.43 ($\epsilon \in [0.2, 0.43]$) as well as a constant-thresholding case of $\epsilon = 0.43$. The local and total FSGSD are defined respectively as $\frac{\Pi}{\varepsilon_{\text{res}} + \Pi}$ and $\frac{\langle \Pi \rangle}{\langle \varepsilon_{\text{res}} \rangle + \langle \Pi \rangle}$, where $\langle \Pi \rangle = \langle -\tau^*_{ij} \overline{S}^{>\epsilon}_{ij} \rangle$ and $\langle \varepsilon_{\text{res}} \rangle = 2\nu \langle \overline{S}^{>\epsilon}_{ij} \overline{S}^{>\epsilon}_{ij} \rangle$ are respectively the volume-averaged SGS dissipation and the volume-averaged resolved viscous dissipation .

For the case of $\mathcal{G} = 0.4$, total-FSGSD never reaches the prescribed goal-value (0.4). The reason is that the total-FSGSD for the case of constant-thresholding with $\epsilon = 0.43$ is smaller than 0.4 for most of the time. As a result, varying thresholding-factor with a "local-FSGSD goal-value" larger than the average FSGSD of constant-thresholding using the same ϵ and ϵ_{max} resulted in total-FSGSD, which was bellow the goal-value. Similarly to the previous case, the test case of the goal-value of 0.3 inherits a large-period oscillations due to capping ϵ at 0.43 level regardless of the

forcing method. These oscillations are removed by increasing $\epsilon_{\max}$ to 0.5. The success of this test with larger $\epsilon_{\max}$ compared with the above mentioned two tests, where $\epsilon_{\max}$ was 0.43, revealed that the upper bound of the interval for allowable threshold variations was not large enough to increase the SGS dissipation accordingly, which implies that with $\epsilon \in [0.2, 0.43]$ flow was over resolved. Therefore, to achieve a FSGSD greater than the average of FSGSD corresponding to constant-thresholding at a certain $\epsilon_{\text{constant-thresholding}}$, it is required to set the $\epsilon_{\max} > \epsilon_{\text{constant-thresholding}}$. This is further confirmed by considering the case with the goal set to 0.25, which illustrates how precisely the spatially variable thresholding methodology can maintain Π at a priori defined level. In addition, when $\epsilon_{\max}$ is set up high enough, the SGS dissipation approaches the desired level within few eddy turnover times.

The time history of TAF and τ_ϵ^{-1} are shown in Figure 3.2. The relaxation time parameter for FT2, τ_ϵ, is approximately one-tenth of the large eddy turnover time, $\tau_{\text{eddy}} = \frac{u'^2}{\langle\varepsilon\rangle} = \frac{\frac{2}{3}K}{2KQ} = \frac{1}{3Q} = \frac{1}{18}$. While the relaxation time parameter for FT1, $C_{f_\epsilon}\text{TAF}^{-1}$, is between one-third and one-fourth of τ_{eddy}. That is, FT2 has as much as 2 to 3 times faster response compared with FT1. This faster time response was able to partially recover the FSGSD. This improvement reveals the importance of very localized and fast mechanisms for the forcing term. The time-averaged term in FT1 destroys the localized Lagrangian nature of the algorithm; however, to smear out the effect of possible very localized FSGSD values, it is recommended to have some averaging mechanism. Hence, another approach, which is currently under investigation, is to track the forcing term itself within a Lagrangian frame so that the forcing term inherits the history of the flow evolution.

Analysis of spatially variable thresholding SCALES by means of the localized dynamic kinetic-energy model (LDKM) – in which either Bardina-like or Germano-like approach is exploited for the dynamical evaluation of both turbulent eddy-viscosity and SGS energy dissipation model coefficients – to close the filtered momentum equations is the subject of further investigations.

Compared with the constant-thresholding case of $\epsilon = 0.43$, number of active wavelets, $\mathfrak{D}$, for small goal value of 0.25 by average is higher, while all the other variable thresholding cases inherit approximately the same average of number of active wavelets (grid points), Figure 3.3.

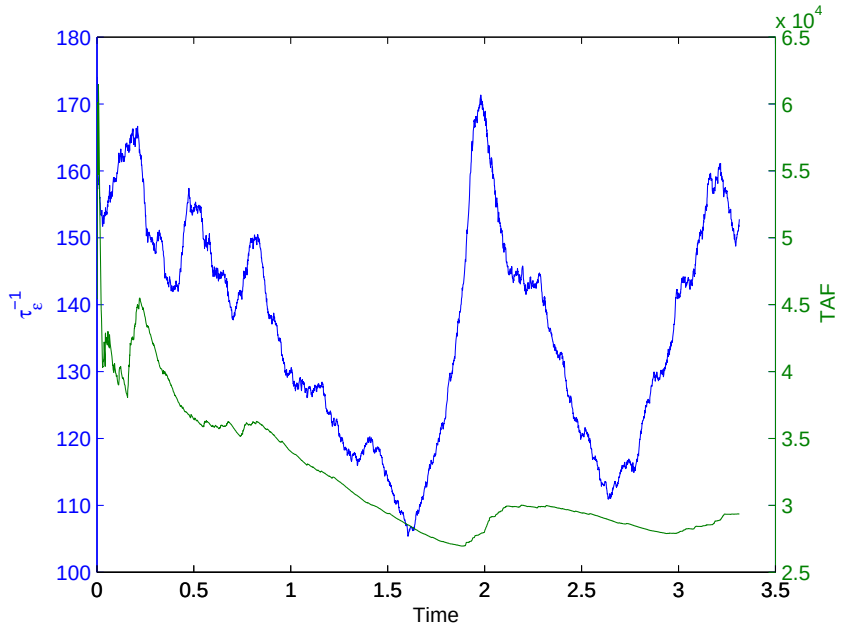

Figure 3.2: Time-history of TAF and τ_ϵ^{-1}.

Relaxation Time Parameter for FT1 : $C_{f_\epsilon}\,\mathrm{TAF}^{-1} \approx \frac{1}{3\,\mathrm{or}\,4}\,\tau_{\mathrm{eddy}}\ (\frac{1}{75})$

Relaxation Time Parameter for FT2 : $\tau_\epsilon \approx \frac{1}{10}\,\tau_{\mathrm{eddy}}\ (\frac{1}{170})$

Compression Ratio, $1 - \frac{\mathfrak{D}}{\mathfrak{D}_{\max}}$ – where $\mathfrak{D}/\mathfrak{D}_{\max}$ is the ratio of the active wavelets on the adaptive grid to the total available wavelets on the non-adaptive effective grid at the highest level of resolution or DNS resolution of 256^3 – illustrated a compression of more than 99% at most of the time for all cases except $\mathcal{G} = 0.25$, Figure 3.4. Even for $\mathcal{G} = 0.25$, the compression is retained at more than 98%. Considering that the sixth order AWCM code is about 3 to 5 times slower per grid point than pseudo-spectral DNS code [6], even the worst case scenario of compression factor of 98%, represents an acceleration of approximately 16 to 10 times with respect to pseudo-spectral DNS. This clarifies the enormous compression, i.e. number one strength of wavelets in turbulence.

Total Resolved Dissipation, $\langle \varepsilon_{\mathrm{res}} \rangle$, Figure 3.5, indicates that not necessarily the smaller goal value for FSGSD results in higher resolved dissipation at all time. This is because of the fact that the continuous coupling between the dissipation and grid-adaptation results in continuous adjustment of resolved dissipation as discussed before by refining or coarsening the grid and as a result at some time/locations it may affect the amplitude of the resolved dissipation differently.

Therefore, one can not make such a judgement whether the lower FSGSD goal value means the the higher resolved dissipation throughout the spatial/time space. This argument is also valid for the Total SGS Dissipation, $\langle \Pi \rangle$, and Total Resolved+SGS Dissipation, $\langle \varepsilon_{\text{res}} \rangle + \langle \Pi \rangle$, as illustrated in Figures 3.6 and 3.7 respectively.

Taylor Microscale Reynolds Number, $Re_\lambda = \frac{u'\lambda}{\nu}$, where the Taylor length-scale can be evaluated for isotropic turbulence as $\lambda = (\frac{15\nu u'^2}{\langle \varepsilon \rangle})^{1/2}$, is demonstrated in Figure 3.8 where the time averaged of each case is also shown.

To summarize, variable thresholding is a methodology, which provides two-way feedback between the modeled SGS dissipation and the computational mesh in order to maintain a priori defined level of SGS dissipation, namely a prescribed level of turbulence resolution. The feedback is achieved through spatio-temporal variation of the wavelet threshold that follows the evolution of the resolved/unresolved flow structures. The proposed methodology represents a **fully adaptive wavelet thresholding filter** for turbulent flow simulation, where the thresholding level is determined on the fly by tracking the areas of locally significant SGS dissipation (or any other physical quantity).

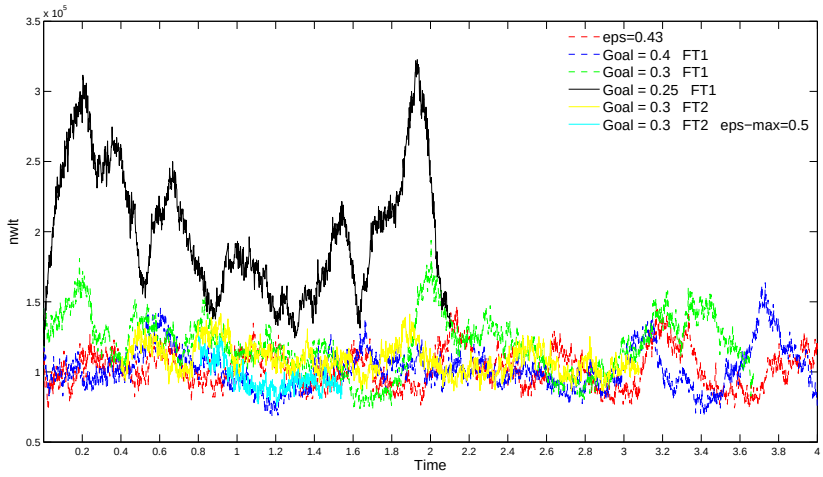

Figure 3.3: Number of active wavelets.

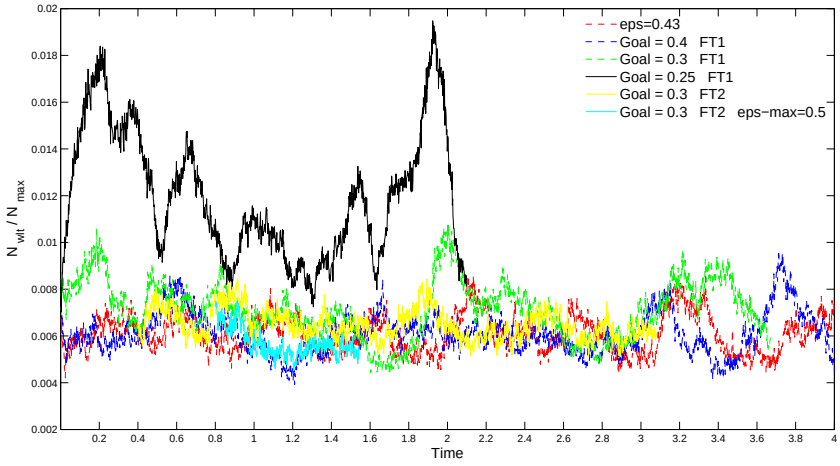

Figure 3.4: Percentage of active wavelets, $\mathfrak{N}/\mathfrak{N}_{\max}$.

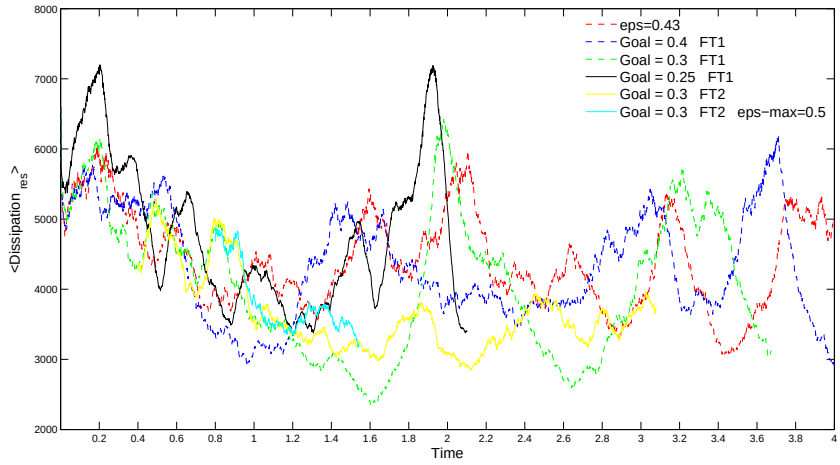

Figure 3.5: Total resolved dissipation, $\langle \varepsilon_{\text{res}} \rangle$.

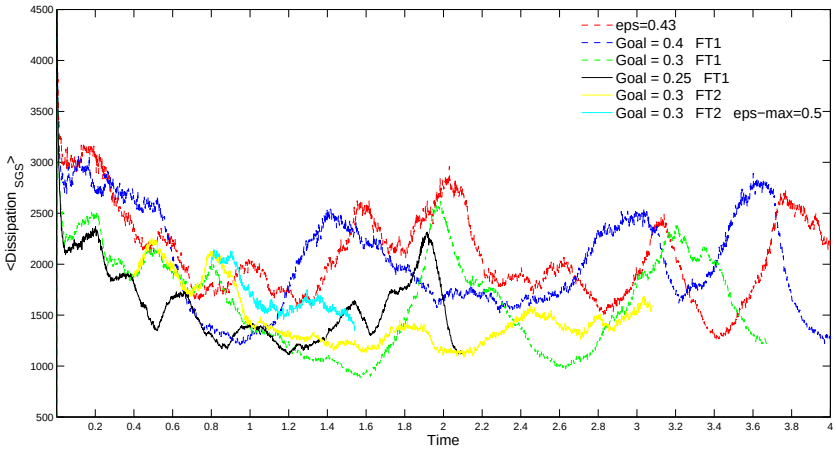

Figure 3.6: Total SGS dissipation, $\langle \Pi \rangle$.

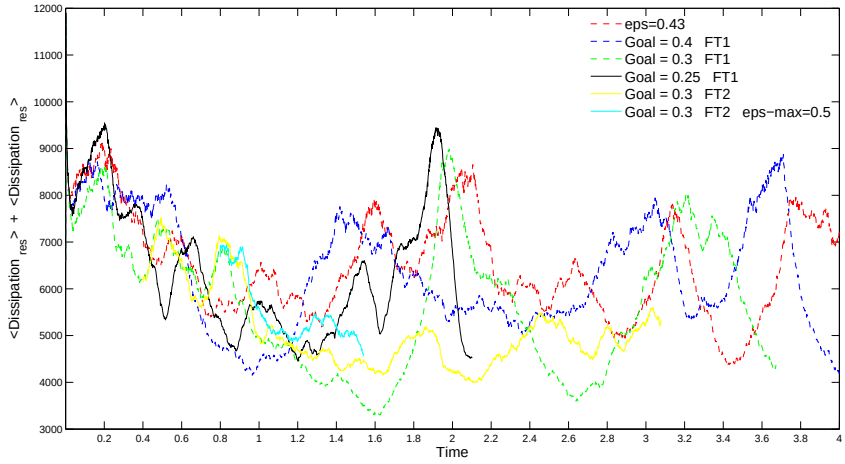

Figure 3.7: Total Resolved+SGS dissipation, $\langle \varepsilon_{\text{res}} \rangle + \langle \Pi \rangle$.

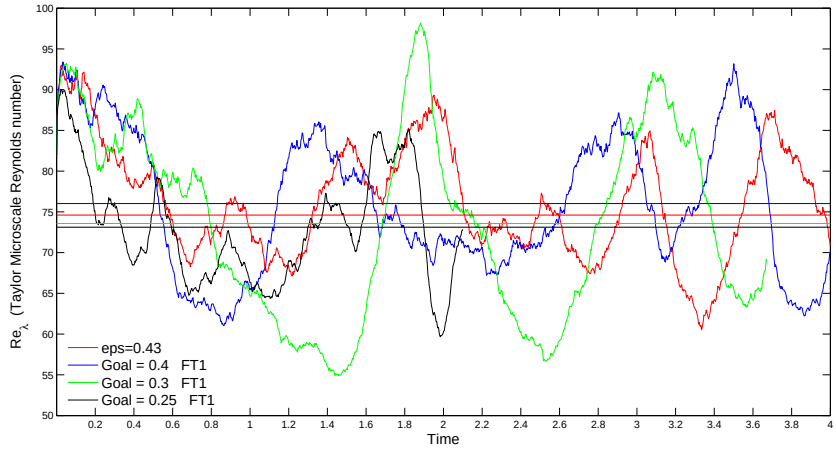

Figure 3.8: Taylor Microscale Reynolds number, Re_λ.

For the sake of completeness it should be mentioned that the spatially varying thresholding methodology is not limited to homogeneous flows or SCALES. It has been also tested for WDNS of inhomogeneous external flows, where forcing term of "characteristic based tracking of epsilon" is constructed based on the magnitude of vorticity or strain rate rather than SGS dissipation since there is no SGS model in WDNS. The results for incompressible flow around NACA 0015 airfoil show a very robust and fast methodology for adjusting the thresholding-factor based on dynamically important flow characteristics, for instance, the magnitude of vorticity or strain rate (Figure 3.9). The main objective of this test case is indeed to prove spatially variable thresholding technique is limited neither to the homogeneous flows nor to SCALES: within the range of WDNS and CVS that SGS dissipation is not defined, other important flow characteristics can be utilized to define the threshold-level as a field. The extension of this feasibility study to CVS and WDNS of external flows at high Reynolds numbers is envisioned for future endeavors.

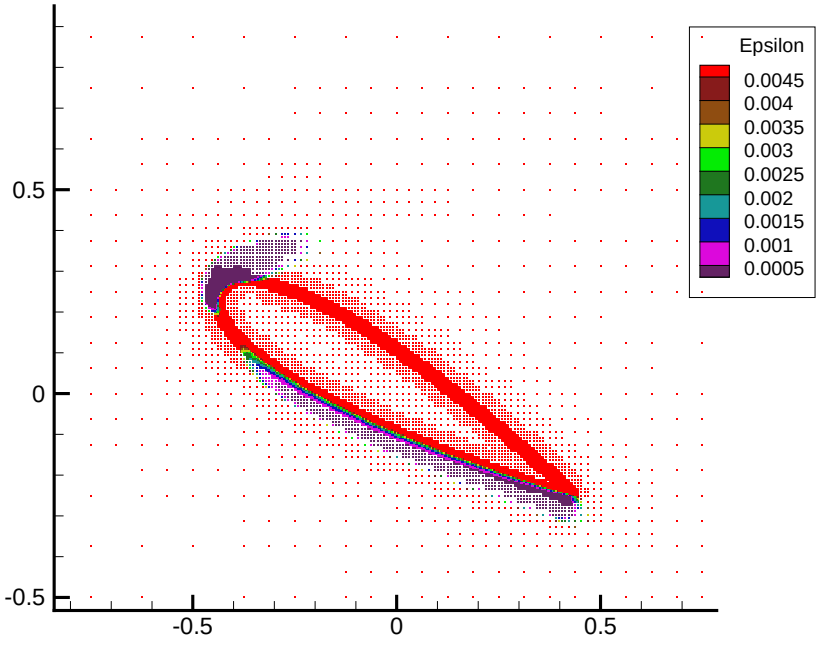

Figure 3.9: Incompressible flow around NACA 0015 at 30° angle-of-attack.

Another ongoing investigation as discussed in the previous section is to track the forcing term itself within a Lagrangian frame so that the forcing term inherits the history of the flow evolution, i.e., analogous to the FT2, the forcing is defined based on Lagrangian Averaged of Forcing, $\mathcal{I}_F$,

$$\text{forcing}_{\text{term}}\left(\mathbf{x},t\right)=\frac{1}{\tau_\epsilon}\frac{1}{\mathcal{I}_F}\left(\Pi-\varepsilon_{\text{res}}\frac{\mathcal{G}}{1-\mathcal{G}}\right)\epsilon\left(\mathbf{x},t\right), \tag{3.5}$$

where the Lagrangian Averaged of Forcing defined as the statistical average of the forcing, $F\left(\boldsymbol{x}\left(\tau\right),\tau\right)$,

$$\mathcal{I}_F\left(\boldsymbol{x},t\right)=\frac{1}{\tau_\epsilon}\int_{-\infty}^{t}e^{\frac{\tau-t}{\tau_\epsilon}}F\left(\boldsymbol{x}\left(\tau\right),\tau\right)d\tau. \tag{3.6}$$

Similar to the threshold-factor, the Lagrangian representation of $F\left(\boldsymbol{x}\left(\tau\right),\tau\right)$, is tracked using the Lagrangian Path-Line Diffusive Averaging approach,

$$\partial_t\mathcal{I}_F+\overline{u}_j^{>\epsilon}\partial_{x_j}\mathcal{I}_F=-\frac{1}{\tau_\epsilon}\left(F_{\text{local}}-\mathcal{I}_F\right)+\nu_{\mathcal{I}_F}\partial^2_{x_jx_j}\mathcal{I}_F, \tag{3.7}$$

where the local forcing is defined as follows:

$$F_{\text{local}}=\Pi-\varepsilon_{\text{res}}\frac{\mathcal{G}}{1-\mathcal{G}}. \tag{3.8}$$

Therefore, the forcing, $F\left(\boldsymbol{x}\left(\tau\right),\tau\right)$, also follows the local flow structures as they evolve in space and time.

Chapter 4

Hierarchical Variable Fidelity Multiscale Turbulence Modeling

The idea of LES and filtering the velocity-field has been a breakthrough in numerical simulation of turbulence, yet still has some limitations including large computational cost for high-Reynolds number wall-bounded flows. To overcome the LES shortcomings, there has been a considerable interest in development of hybrid turbulence models. Since they aim at providing better results than RANS without the cost of a complete LES in the entire domain. This is essential for many industrial applications, in particular for high-Reynolds number flows in the presence of walls.

Growing number of complicated fluid devices and rising challenges of complex fluid flows across numerous disciplines necessitate the development of robust multiscale variable fidelity methodologies. A wide range of hybrid LES/RANS and DNS/LES/RANS approaches to smooth the sharp interface between these different models has been attempted. Despite a relatively longtime endeavors to match these techniques and construct a coherent transition, still much remain for future research, mostly because these methodologies are fundamentally different. Furthermore, ever since the inception of Computational Fluid Dynamics, turbulence modeling and numerical methods evolved as two separate fields of research with the perception that once a turbulence model is developed, any suitable computational approach can be used for the numerical simulations of the model.

The high compression property of the wavelet-based decomposition is a promising feature, which can make very large scale hybrid adaptive wavelet-based DNS/LES/URANS of turbulent flows a reality. This work develops a framework for very large-scale parallel hybrid adaptive wavelet-based simulation of turbulence. Two major building blocks, required for such a framework, are

1) hybrid models within the context of adaptive wavelet-based methods by means of the notion of defining the thresholding-factor of the wavelet threshold filter as a field variable (spatial/temporal variable thresholding); and 2) highly-scalable parallel adaptive wavelet-based PDE solver. While the later has been completed by this work, the former is the first major subject of this research.

As mentioned in Chapter 1, CVS in its original formulation [15] solves the wavelet-filtered vorticity equations with the use of orthogonal Daubechies wavelets, while SCALES analogous to LES is solves wavelet-filtered Navier-Stokes equations along with SGS models using bi-orthogonal second-generation interpolated wavelets. However, Goldstein and Vasilyev [24] showed that the velocity-field can be decomposed to deterministic coherent and stochastic incoherent (with Gaussian PDF) modes using wavelet threshold filtering in velocity space, thus, CVS can also be based on primitive variables (velocity-pressure). Therefore, hereafter this work refers to CVS in velocity-pressure formulation. This implies that this CVS and SCALES both solve the wavelet-threshold filtered Navier-Stokes equations without and with SGS models respectively though at different threshold levels. On the other hand, WDNS can be also viewed as solution of wavelet-filtered Navier-Stokes equations at very small value of threshold parameter and without an SGS model. All in all, the three methodologies all solve the same governing equations.

In wavelet based methods in general and particularly in SCALES, implementation of Hybrid DNS/LES/RANS mainly requires change of wavelet thresholding-factor with no or minimal additional efforts for merging two different solvers. Because, within the context of wavelet-based methods, variable fidelity is achieved predominantly by changing the thresholding-factor: very small thresholding-factor corresponds to WDNS, moderately small thresholding-factor corresponds to CVS, larger value of thresholding-factor along with solving the SGS models result in SCALES, and much larger value of thresholding-factor for solving Unsteady Reynolds Averaged Navier-Stokes equations lead to WURANS [29] (wavelet-based URANS). Hence, a careful combination of WDNS, CVS, SCALES, and WURANS in a systematic manner can lead to fully adaptive wavelet-based hybrid method.

Transition from WDNS to CVS is very straightforward since it can be controlled only by change of thresholding factor. Transition from SCALES to CVS can be performed differently. Three main possibilities are: 1) Utilizing SGS model to control SGS dissipation (which has already been discussed) at all time throughout the entire spatial space; 2) instead of solving SGS model, at the CVS level, local kinetic energy of the last band can be monitored; and 3) instead of solving SGS model, at the CVS level, the numerical dissipation due to WTF truncation – defined analogous to the SGS dissipation based on the resolved kinetic energy – can be monitored. Following the discussion in Chapter 3, the ratio of SGS and resolved dissipations is a more general measure of turbulence resolution, consequently the first and the third approaches seem to be more robust. However, the first approach is the most practical for implementation and is more general. As a result, transition from SCALES to CVS can also be defined based on change of thresholding-factor.

The transition from SCALES to WURANS is considerably more challenging since each is solving different governing equations and this violates the synergistic transition, which is explained for hybrid WDNS/CVS/SCALES. In addition, the large values of threshold parameter necessitate modeling the effect not only small, but large scales, thus require the use of models similar to RANS, but different in nature, since the models should not be based on ensemble or time averages. Hence, in order to properly transition from SCALES to WURANS, one requires new SGS models, capable to model the effect of energy containing range. This new class of models will be also free from the challenges corresponding to classical RANS - e.g. model coefficients, which must be correlated based on experimental data. Self-adaptive models of Perot and Gadebusch [37] are good candidates for such models, but require further studies. In addition, model switching, model-refinement, can be based on other physically meaningful flow properties (like $\mathcal{F}$) resulting in a continuous dynamic model change from regular SGS ones (like dynamic SGS model) to the new types (which are modeling the effect of unresolved large structures). This implies an automated model selection based on the required local level of fidelity, the appropriate level of resolution of the dynamically important flow structures, and user's input. Once developed, the new models can be incorporated within the context of the variable thresholding methodology proposed in this dissertation. Thus this work

should be viewed as a proof of concept that cover WDNS/CVS/SCALES regimes, the transition to WURNS regime and the development of appropriate SGS models is the subject of future research and is not further elaborated in this research.

To summarize, ever since the first use of wavelets in turbulence [13], a number of wavelet-based multi-resolution approaches have pursued different philosophy of physics-based turbulence modeling, namely direct coupling of numerical methods and physical models within the multi-resolution wavelet analysis framework. For instance, WDNS employs mainly the compression achieved by wavelets; CVS in addition to compression decomposes the turbulent field into deterministic (coherent) and stochastic (incoherent) modes; and SCALES resolves the most energetic deterministic (coherent) structures while modeling the effect of less energetic coherent/incoherent structures. This work proposes a unique systematic approach to merge these techniques within one single computational framework where only one type of governing equations is solved all the time. This methodology exploits the use of spatially variable thresholding technique that exhibits synergistic transition among various required levels of user-defined "accuracy/resolution/fidelity". This approach automatically provides the required numerical resolution and the model-fidelity in and space/time adaptive fashion based on a two-way coupling of numerical method and physical models.

The proposed approach dynamically tracks the regions of interest in spatial and time space and not only adapts the grid but also adjusts the model as well: the former alone is analogous to **hp**-refinement, though the latter is a new concept of model-refinement, which is defined as **m**-refinement. Within wavelet-based methods, the **p**-refinement implies changing locally the order of wavelet transform [26]. Therefore, the methodology established in this dissertation constitutes an **hm**-refinement technique. Although understanding how to adjust and correlate the models to the physical phenomena is a fundamentally challenging problem, the proposed methodology explicitly controls the coupling between models and numerical methods so that the interaction can be fine tuned to tailor the models based on the theoretical/numerical/experimental observations.

The dependency diagram for both original SCALES [24] and the variable-fidelity SCALES – proposed by this work – as well the classical explicitly filtered LES illustrates the general connections

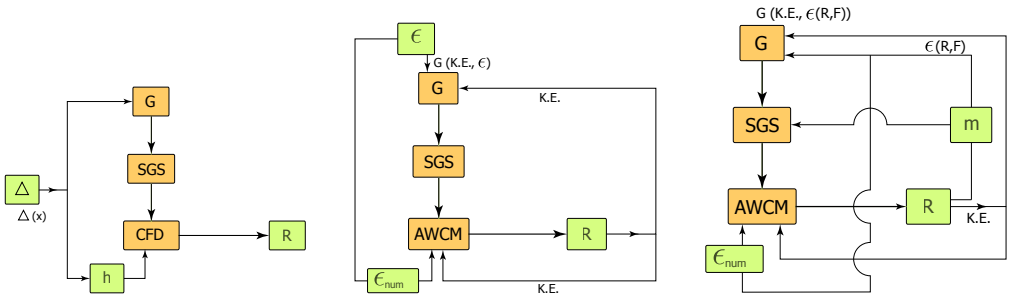

(a) Explicitly Filtered LES (b) Original SCALES (c) **m**-SCALES

Figure 4.1: Dependency diagram for original SCALES, variable-fidelity SCALES proposed by this work, and classical explicitly filtered LES. Terminology: G: Filter, R: results, m: model refinement, nun: numerical, F: is an arbitrary dynamically important physical quantity such as $\mathcal{F}$

of the components of solver in each case and clearly identifies how the proposed variable-fidelity SCALES connects all components including numerics/models/physics altogether to construct a fully dynamically adaptive computational framework, Figure 4.1. In classical explicitly filtered LES, the filter-width is priori user-defined based on which the resolution is determined; therefore, both the CFD engine (through the resolution) and the filtering mechanism (via the filter-width) depend on priori defined filter-width, which is not fine-tuned based on the results. The original SCALES improved this by its wavelet-filtered based dynamically adaptive mechanisms via constantly adapting both the numerical grid and the filter-width based on the results. The threshold-level of WTF can be different for the resolved-scales-numerical-engine (AWCM) and the filtering procedure. However, the wavelet thresholding filter uses a priori user-defined threshold-level and as a result of filtering the velocity-filed with this constant threshold, the WTF is indeed imposing a feedback based on a constant level of resolved kinetic energy. This limitation then has been removed by the current work through constructing a fully adaptive wavelet thresholding filter as explained in detail before. The new SCALES, which is denoted as **m**-SCALES, requires a priori user-defined level of resolution/fidelity based on which the threshold is adapted to maintain the fidelity constant as user has requested. In original SCALES, the filtering mechanism is a function of results (kinetic energy) and a constant threshold, while in the newly developed SCALES, threshold itself is a function of results (any physical quantity and not limited to kinetic energy) and the user-defined fidelity.

4.1 Results

To examine the functionality of the developed hybrid variable-fidelity methodology, two important measures must be well scrutinized: accuracy of preserving the $\mathcal{F}$ at the specified goal value $\mathcal{G}$ and time-response of the model to adjust to the $\mathcal{G}$. In other words, it is essential for the model to not only well-maintain the fidelity of the desired physical quantity at the goal value but also adjust the resolution rapidly to a new goal value when/where it changes. Hence, the proposed methodology is thoroughly tested for the cases where the desired physical quantity to-be-controlled (here the $\mathcal{F}$) is changing constantly in space/time and is very localized in order to ensure that under such circumstances still the developed framework is capable to control the $\mathcal{F}$ accurately and rapidly. The homogenous turbulence is the extreme of such situation where the resolved dissipation is highly intermittent in both space and time, thus, requiring rapid adjustment of wavelet threshold to maintain required local and volume-averaged turbulence resolutions. If the methodology can maintain its volume-average at a specified goal value over many eddy turnover time scales, τ_{eddy}, or adjust to a new goal within/less-than one τ_{eddy}, the method can be claimed as a robust hybrid computational framework. The inhomogeneous turbulence in general is more complicated to model numerically; however, it should be noted that this approach is local and should be applicable to inhomogeneous turbulent flows. In addition, it also can be applied to the situations with spatially varied goal value, typical to inhomogeneous flows.

This section examines the extreme case, namely the instantaneous change of the goal value $\mathcal{G}$, resulting in rapid switching among WDNS, CVS, and SCALES regimes. If the methodology can deal with such abrupt changes, it surely can deal with spatial changes as well. In addition to the interpolation approach introduced in Chapter 3, the Lagrangian path-line diffusive averaging equation (3.1) is solved directly along with the SCALES governing equations, hereafter is referred to as "Evolution Equation (EE)" approach. The variable thresholding mechanism is based on the second forcing, FT2, which is introduced in Chapter 3. However, to fully utilize the local intermittency of the structures, instead of a global relaxation time-scale, $\tau_\epsilon^{-1} = \langle |\overline{S}_{ij}^{>\epsilon}| \rangle$, the corresponding local

time-scale associated to the local rate-of-strain, $\tau_\epsilon^{-1} = |\overline{S}_{ij}^{>\epsilon}|$, is used. As discussed above, the main factors that examine the accuracy of the approach are the accuracy of preserving the $\mathcal{F}$ (local fraction of SGS dissipation: $\mathcal{F} = \frac{\Pi}{\varepsilon_{\text{res}}+\Pi}$) at the specified $\mathcal{G}$ (goal value) as well as time-response of the model to adjust to the $\mathcal{G}$. The former indicates how accurate the model can really maintain the goal value and the later shows how fast the overall turbulence resolution can be adjusted to the desired value while changing the goal.

It is evident that the two key controlling parameters here are the time-scale and the level of diffusivity. The first order interpolation itself introduces a larger diffusion while one should expect less numerical diffusion associated with the 3$^{\text{rd}}$ order interpolation. In the EE approach, the diffusion coefficient is a parameter, which can be controlled. A relatively complicated test case, which can be considered as a simplified model of the physical situations where the level of the resolution required to be changed in time constantly, is constructed where the $\mathcal{F}$ is continuously changed after few τ_{eddy}. Therefore, value of $\mathcal{G}$ for every $5\tau_{\text{eddy}}$ belongs to $\{0.2, 0.25, 0.3, 0.2, 0.3, 0.25\}$. The simulation of homogeneous turbulence at $Re_\lambda \cong 120$ on a non-adaptive effective resolution of 256^3 with viscosity of $\nu = 0.09$ was performed, where the the turbulence field was initialized with a well developed CVS field using the same resolution, viscosity, and Reynolds number. The goal value of the turbulence resolution, i.e. $\mathcal{G}$, was changed as mentioned above. The simulation was repeated for both 1$^{\text{st}}$ order and 3$^{\text{rd}}$ order interpolation as well as EE with four different viscosity coefficients of $\nu_\epsilon \in \{0.05, 0.1, 4, 5\}$. These series of test address the effect of diffusion on both time-response and accuracy of the achieved turbulence resolution compared with the goal value.

The interpolation approach shows a time-response delay, which is by and large greater than one eddy turnover time, resulting in slow adjustment to the goal value, Figure 4.2(a). This undesired and unrealistic response lag is similar regardless of the interpolation order; however, it is observed that the small diffusion coefficient in case of EE can prevent this and as a result it is concluded that the diffusion of the scheme is the cause of the time-response delay, Figure 4.2(b). In terms of the amplitude of the $\mathcal{F}$, i.e. the accuracy of retaining the $\mathcal{G}$, also it is observed that the lower diffusion achieved a closer global volume-averaged $\mathcal{F}$ ($\langle\mathcal{F}\rangle$) to the $\mathcal{G}$ at each time.

As it is observed, large diffusion can significantly delay the time-response and affect the level of accuracy of turbulence resolution; however, threshold field must be a smooth field and any very localized structures with sharp interfaces must be prevented since velocity is filtered using threshold and any noise in threshold field can lead to significant noise and undesired small-scale fluctuations in the velocity field, i.e. the entire solution. Although with $\nu_\epsilon = 0.1$, no evidence of such instabilities was observed, a qualitative investigation of smoothness of threshold is highly recommended. Therefore, the contour plots of threshold throughout the domain for all studied values of ν_ϵ as well as for both first and third order interpolation approaches are examined. Figures 4.3 and 4.4 provide snapshots of such contour plot at two different time for EE with $\nu_\epsilon \in \{0.05, 0.1, 4, 5\}$ and both 1^{st} order and 3^{rd} order interpolation methods.

Another factor to look into is the range of change of τ_ϵ. In all aforementioned cases, there were no limits on the τ_ϵ and since this is the local time-scale, which depends on the local strain-rate, it could be either very small or very large values. Figure 4.5 illustrates the minimum, maximum, average, and volumed-averaged of τ_ϵ for three different cases using both interpolation and EE with $\nu_\epsilon = 5$ approaches. Relatively small minimum values is observed in the time-history of τ_ϵ for all three cases. Large values of τ_ϵ, which correspond to small local strain-rate, are theoretically acceptable since they can be interpreted as rapid response. Since threshold is always capped to physically meaningful minimum and maximum allowable bounds, there is no danger in even very large τ_ϵ. However, small values of τ_ϵ, which correspond to large local strain-rate, can be problematic as they can lead to very slow response and consequently result in lag in adjusting to physically meaningful value of threshold. Hence, three different sets of test, where either the minimum value of τ_ϵ, maximum value of τ_ϵ, or the interval (both min and max) within which τ_ϵ can be changed are specified and investigated. This allows to cap τ_ϵ to a limited range rather than allowing very slow or extremely rapid local change of threshold. For the interpolation approach, the results for limiting only the minimum value of τ_ϵ to small factor of τ_{eddy}, e.g. $\tau_{\epsilon_{\text{min}}} = 2\tau_{\text{eddy}}$, shows a slight improvement in the accuracy of the level of $\mathcal{F}$ at some time; however, for large lower bound of τ_ϵ, e.g. $\tau_{\epsilon_{\text{min}}} = 6\tau_{\text{eddy}}$ even a less accurate $\mathcal{F}$ is attained, Figure 4.6(a). The results for limiting

only the minimum value of τ_ϵ in case of EE approach indicates that a less accurate $\mathcal{F}$ is achieved, Figure 4.6(b). For the test cases where either the maximum or both minimum and maximum bounds of τ_ϵ are set, also either no or very-low improvement in the the accuracy of the level of $\mathcal{F}$ is observed, Figure 4.6(a). To conclude, it appears that it is not necessary to bound the τ_ϵ.

The time-averaged energy spectra for each interval of $\mathcal{G}$ for the EE case with $\nu_\epsilon = 0.1$ are illustrated in Figure 4.7(a). The value of $\mathcal{G}$ indeed consist of three different values, which each is repeated twice. So, it is expected that the time-averaged energy spectra for each of these pairs of interval to be identical; however, this is not observed for all three values of $\mathcal{G}$. For small $\mathcal{G}$ of 0.2, time-averaged energy spectra of the first and fourth intervals are close even at the dissipation range since at small $\mathcal{G}$ the threshold will be smaller and consequently flow will be much more resolved at all ranges including dissipation range. But at larger value of $\mathcal{G}$, where threshold by average is larger, the flow is less resolved. This implies that at larger $\mathcal{G}$, a greater percentage of flow structures especially at the higher wavenumbers, i.e. dissipation range, are modeled and due to uncertainties associated with the SGS models, a less pronounced consistency between time-averaged energy spectra of two different fields with the same $\mathcal{G}$ is achieved. By increasing the length of interval, a better agreement would be accomplished.

The time-averaged dissipation spectra of the six cases presented in Figure 4.7(a), are illustrated in Figure 4.7(b). An important point to clarify is the jump in both energy and dissipation spectra at about $\kappa = 64$ corresponding to the effective resolution of 128^3. This jump is due to the fact that the effective resolution is not always 256^3, which is the strength of the wavelet-based methods as discussed in Figure 1.5. This effective resolution lower than the maximum resolution is even more probable in SCALES. Namely, in SCALES, most of the time, the highest level of resolution is one less than the maximum level of resolution. This implies that by not only an adaptive resolution but even smaller maximum resolved wavenumber, SCALES can resolve the most energetic structures, which are responsible for a correct energy cascade. In this particular case, at various time frames, the maximum resolution is 128^3; as a result of averaging instantaneous spectrum with different maximum wavenumbers of 64 and 128, a kink is appeared in the time-averaged

spectra. Figures 4.8 and 4.9 present the time-averaged energy and dissipation spectra by averaging the time-frames only with either $\kappa_{\max} = 64$ or $\kappa_{\max} = 128$. Figures 4.10(a) to 4.12(b) are analogous to Figures 4.7(a) to 4.9(b) but for $\nu_\epsilon = 0.05$.

This examined intricate test case proved that with the use of the Lagrangian spatially variable thresholding, a "Hierarchical Multiscale Adaptive Variable Fidelity Wavelet-based Turbulence Modeling" methodology can be utilized. This hybrid turbulence modeling technique has shown a very robust uniform-solver/single-framework for performing fully adaptive hybrid turbulence simulations akin to hybrid LES/DNS. Within this adaptive wavelet-based computational framework, only one solver is utilized and as a result challenges corresponding to overlapping multiple solvers and difficulties associated with Adaptive Mesh Refinement (AMR) are unrelated. The current framework makes it possible to perform hybrid wavelet-based DNS, coherent vortex simulations, as well as wavelet-based fully adaptive LES. Namely, the developed framework is for hybrid WDNS/CVS/SCALES, while the extension to WDNS/CVS/SCALES/WURANS is analogous though as discussed earlier, it requires developing new self-adaptive RANS-type models.

While the developed hybrid framework makes it possible to perform fully adaptive hybrid WDNS/CVS/SCALES, the extension of the investigated benchmark to real flow applications where spatially varying $\mathcal{G}$ is desired remains for the future investigations. The computational tool required for such complex real flow simulations has already been implemented; it is only required to define the realistic spatio-temporal mask for $\mathcal{G}$. For instance, for wall bounded flows, it is advised to set small value of $\mathcal{G}$ in the vicinity of the wall. Another interesting example of the inevitability of spatially varying $\mathcal{G}$ hybrid turbulence simulations, is airplane propulsion systems modeling, where generally very accurate resolution is desired in combustion chamber, while less accurate simulations are adequate in bypass-duct/compressor/turbine to capture the physically important flow structures.

Once again, it worth stressing the fact that the volume-average of a very localized quantity, which is very rapidly and randomly varying in space/time, could be maintained approximately constant and altered quickly, is proving how efficient is this scheme and how powerful it will be for the inhomogeneous applications, where the spatial and/or temporal variations of $\mathcal{F}$ are smooth.

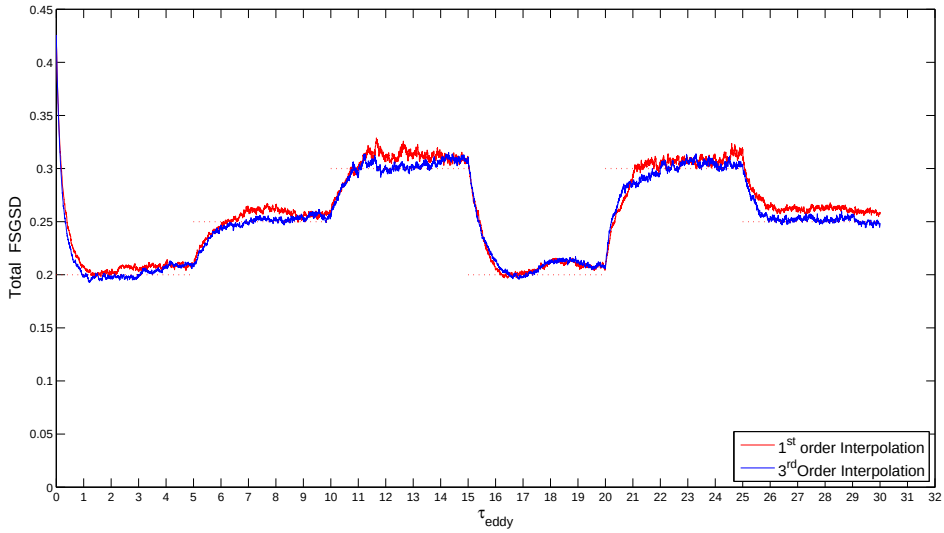

(a) Interpolation method

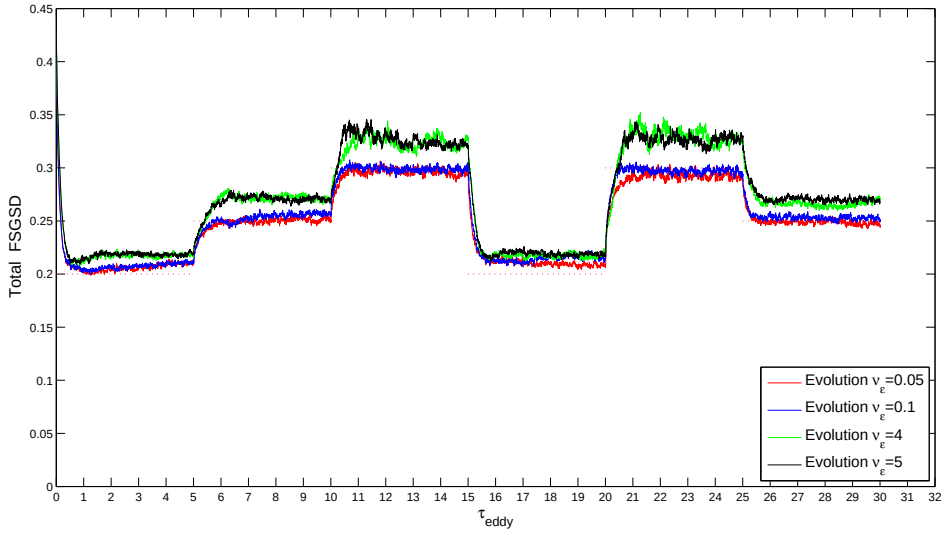

(b) EE method

Figure 4.2: Variable $\mathcal{G}$ SCALES, $\epsilon \in [0.2, 0.5]$, ν= 0.09, C_f= $6.\bar{6}$, Re_λ= 70, 256^3. Total FSGSD is defined as $\langle \mathcal{F} \rangle = \frac{\langle \Pi \rangle}{\langle \varepsilon_{\text{res}} \rangle + \langle \Pi \rangle}$, where $\langle \Pi \rangle = \langle -\tau^*_{ij} \overline{S}^{>\epsilon}_{ij} \rangle$ and $\langle \varepsilon_{\text{res}} \rangle = 2\nu \langle \overline{S}^{>\epsilon}_{ij} \overline{S}^{>\epsilon}_{ij} \rangle$ are respectively the volume-averaged SGS dissipation and the volume-averaged resolved viscous dissipation .

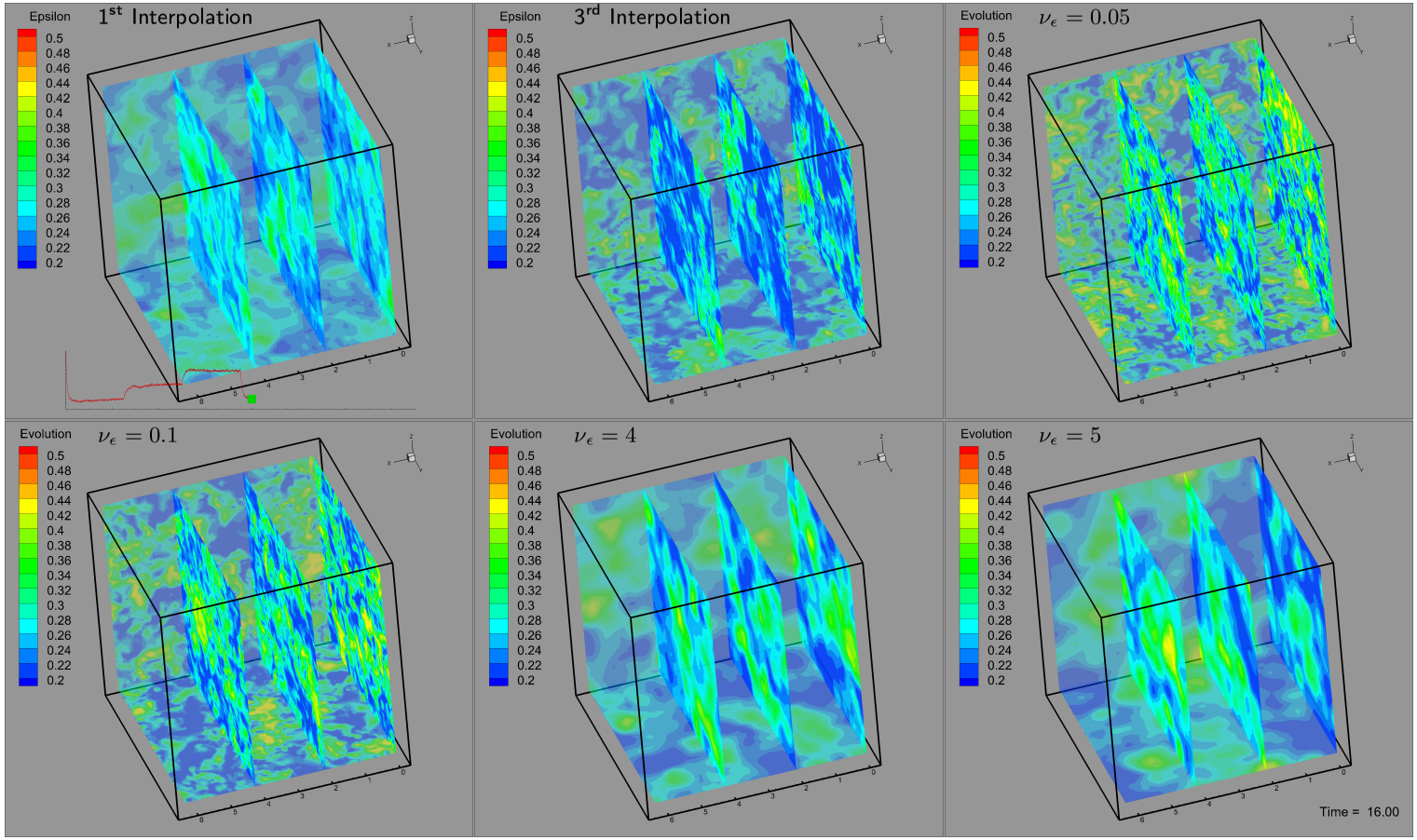

Figure 4.3: Contour of threshold for variable $\mathcal{G}$ SCALES, Interpolation and EE approaches, $\epsilon \in [0.2, 0.5]$, ν= 0.09, C_f= $6.\bar{6}$, Re_λ= 70, 256^3. At the beginning of the fourth interval, $t = 16\,\tau_{\text{eddy}}$.

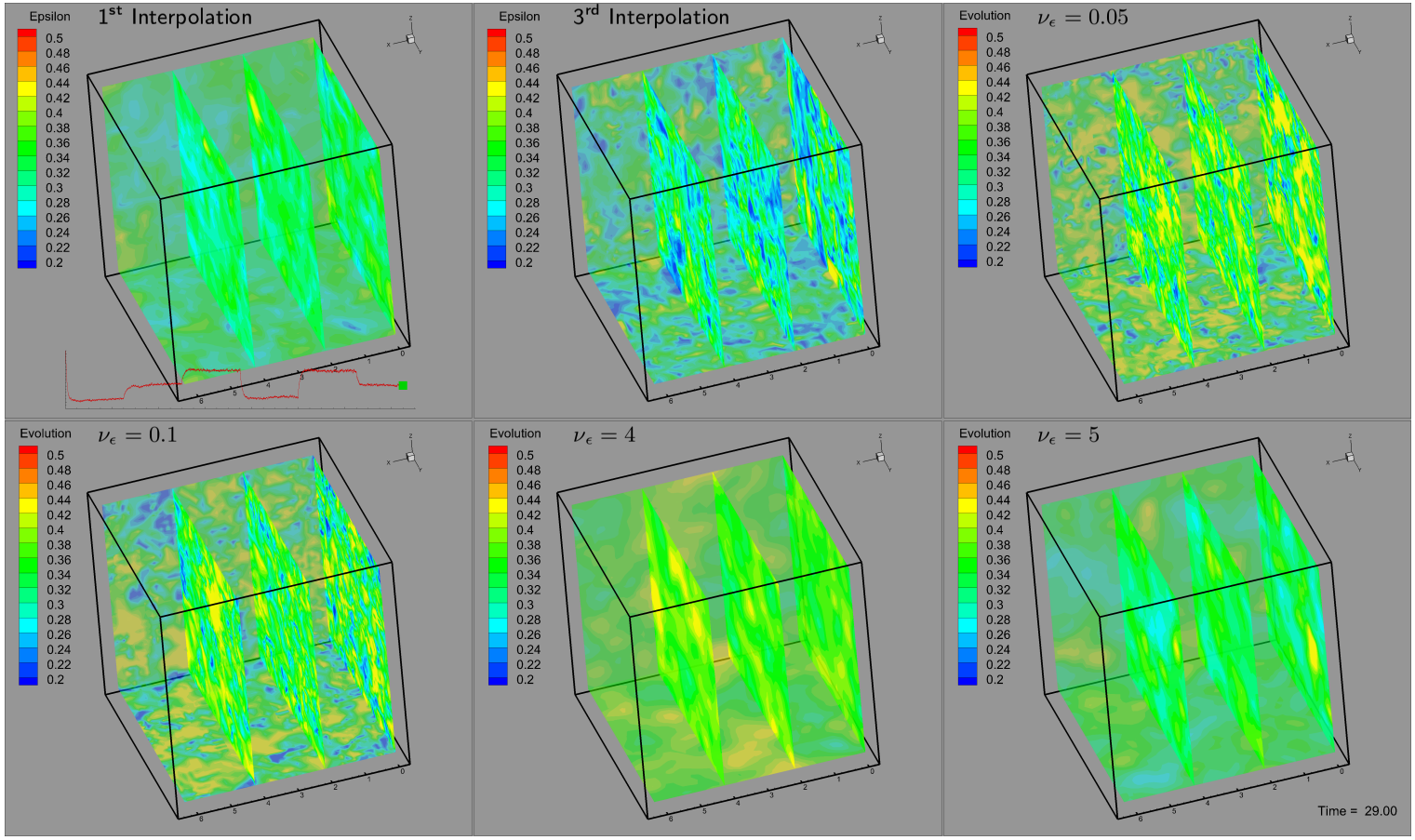

Figure 4.4: Contour of threshold for variable $\mathcal{G}$ SCALES, Interpolation and EE approaches, $\epsilon \in [0.2, 0.5]$, ν= 0.09, C_f= $6.\bar{6}$, Re_λ= 70, 256^3. At the end of the sixth interval, $t = 29\,\tau_{\text{eddy}}$.

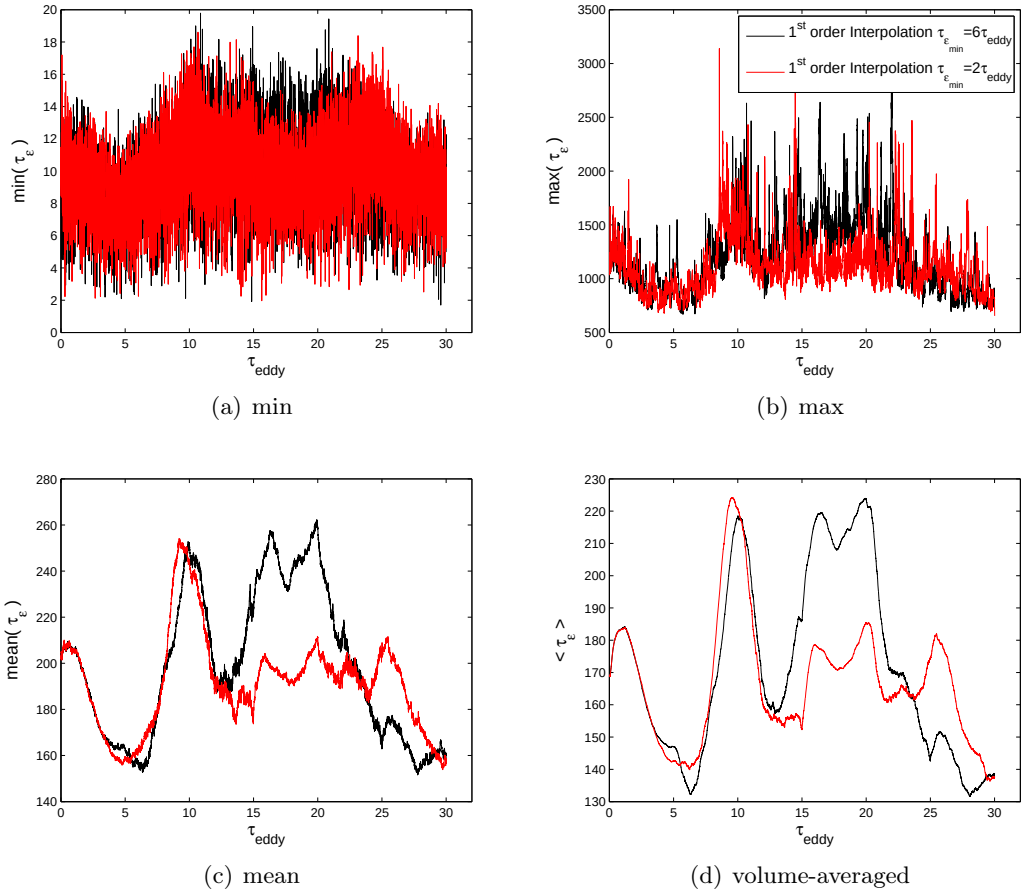

(a) min (b) max

(c) mean (d) volume-averaged

Figure 4.5: Statistics (Minimum,Maximum,Average,Volume-Average) of local time-scale τ_ϵ for variable $\mathcal{G}$ SCALES, $\epsilon \in [0.2, 0.5]$, ν= 0.09, C_f= $6.\bar{6}$, Re_λ= 70, 256^3.

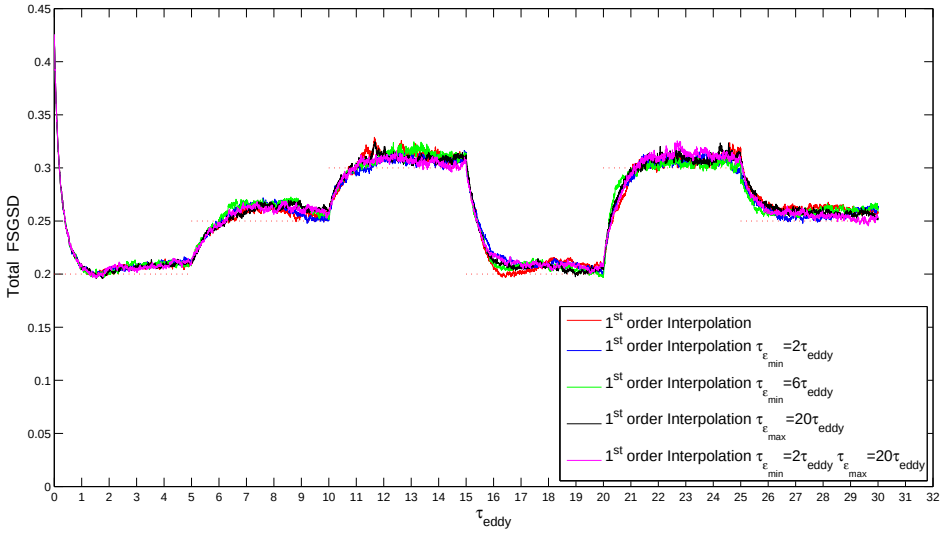

(a) Interpolation method

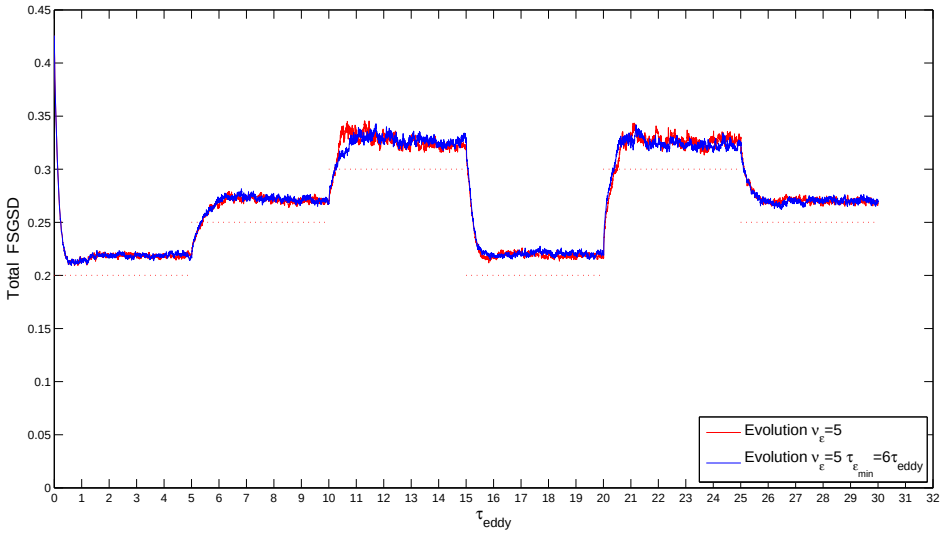

(b) EE method

Figure 4.6: Variable $\mathcal{G}$ SCALES with capping τ_ϵ, $\epsilon \in [0.2, 0.5]$, ν= 0.09, C_f= $6.\bar{6}$, Re_λ= 70, 256^3.

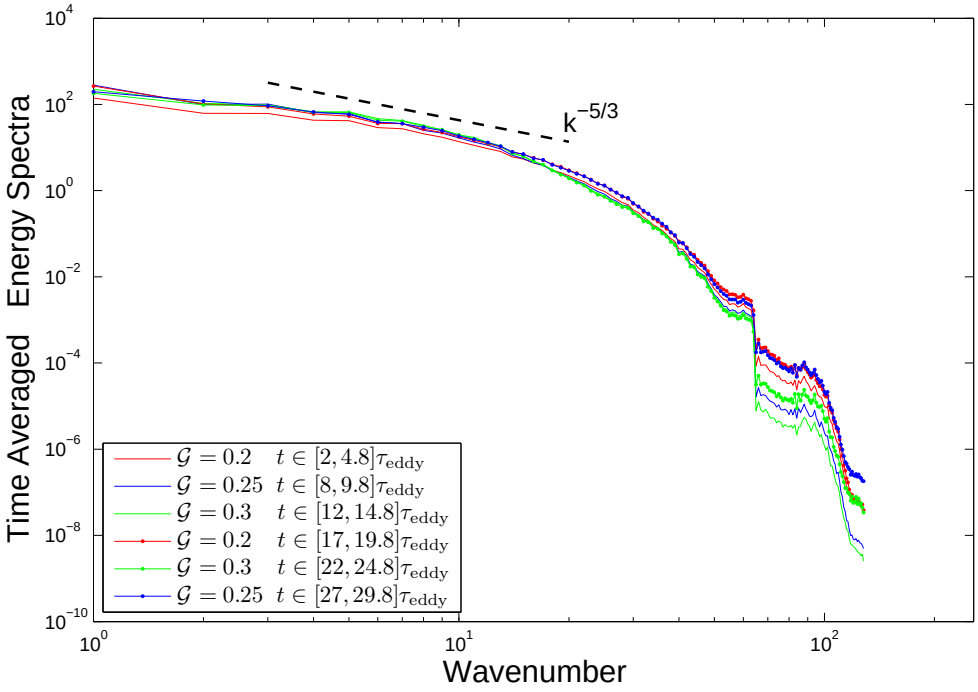

(a) Energy spectra

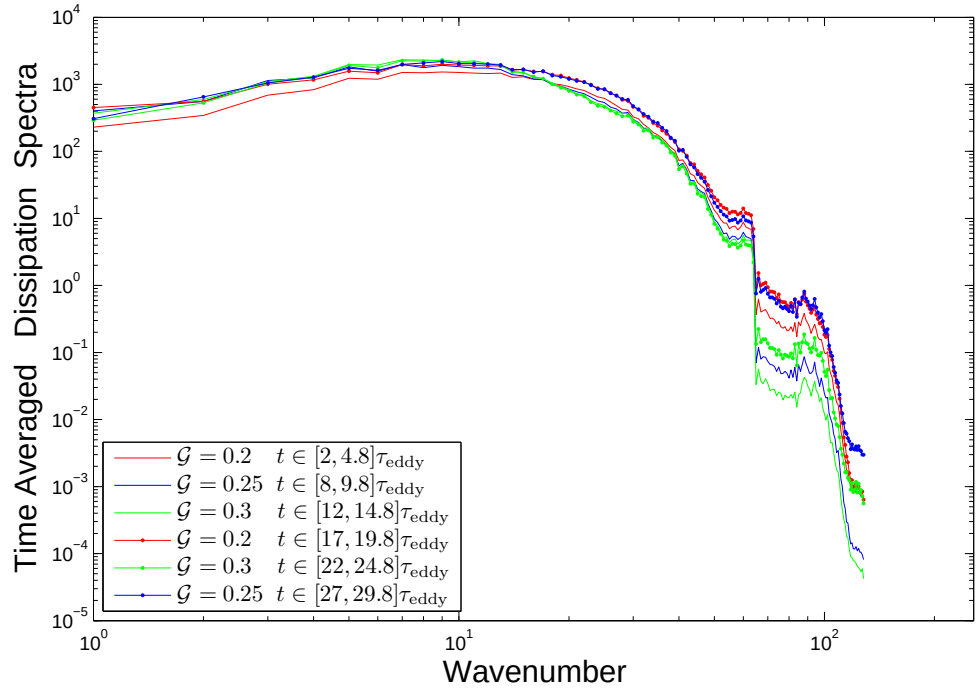

(b) Dissipation spectra

Figure 4.7: Time-averaged energy and dissipation spectra for variable $\mathcal{G}$ SCALES, EE method with $\nu_\epsilon = 0.1$, $\epsilon \in [0.2, 0.5]$, ν= 0.09, C_f= $6.\bar{6}$, Re_λ= 70, 256^3.

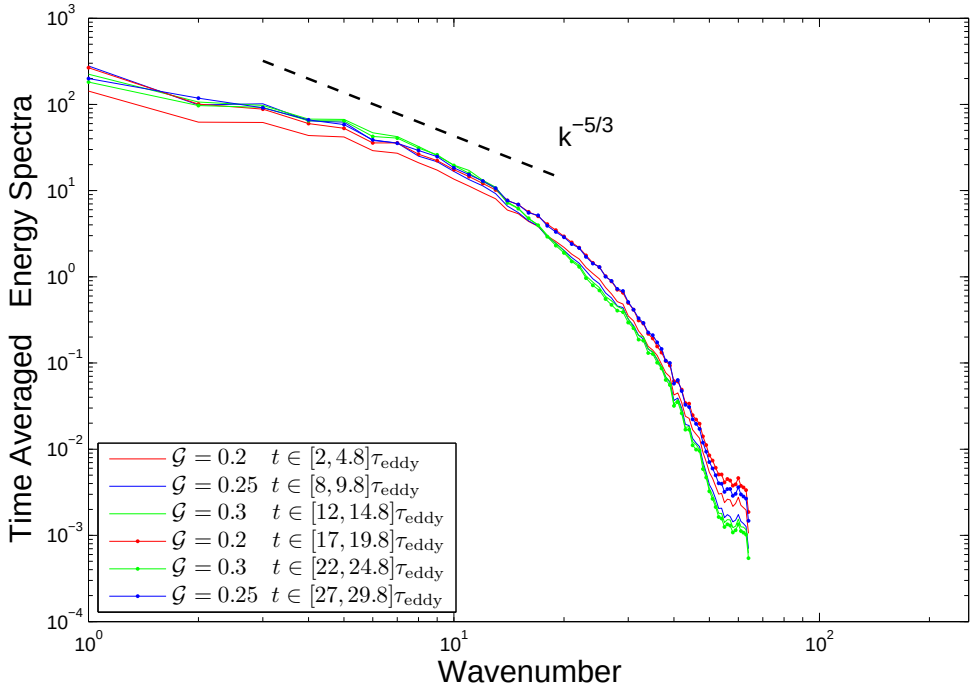

(a) $\kappa_{\max} = 64$

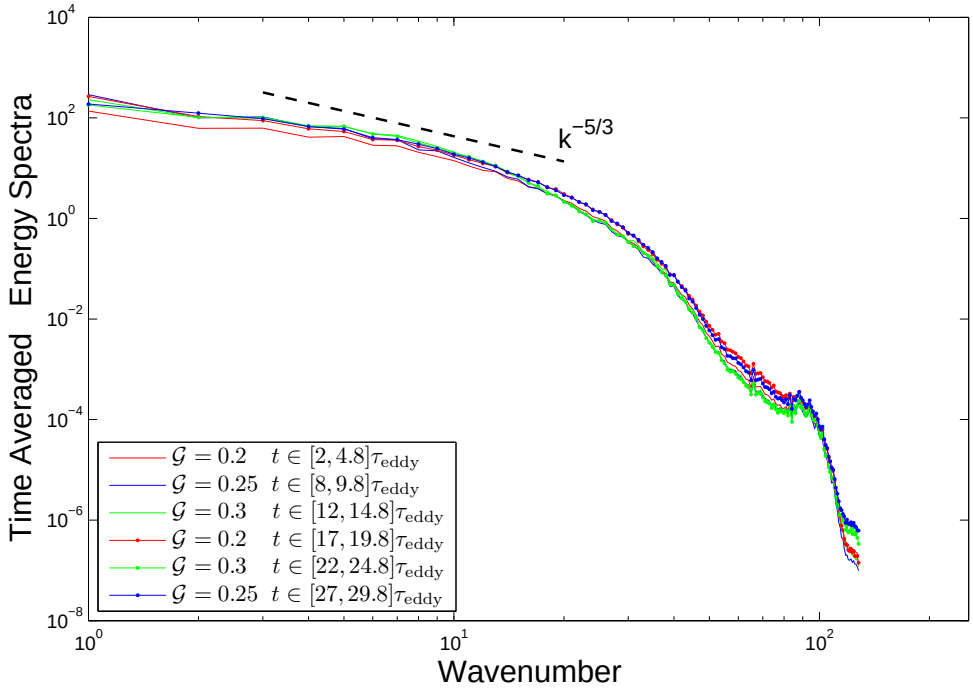

(b) $\kappa_{\max} = 128$

Figure 4.8: Time-averaged energy spectra of time-frames with $\kappa_{\max} = 64, 128$ for variable $\mathcal{G}$ SCALES, EE method with $\nu_\epsilon = 0.1$, $\epsilon \in [0.2, 0.5]$, ν= 0.09, C_f= 6.$\bar{6}$, Re_λ= 70, 256^3.

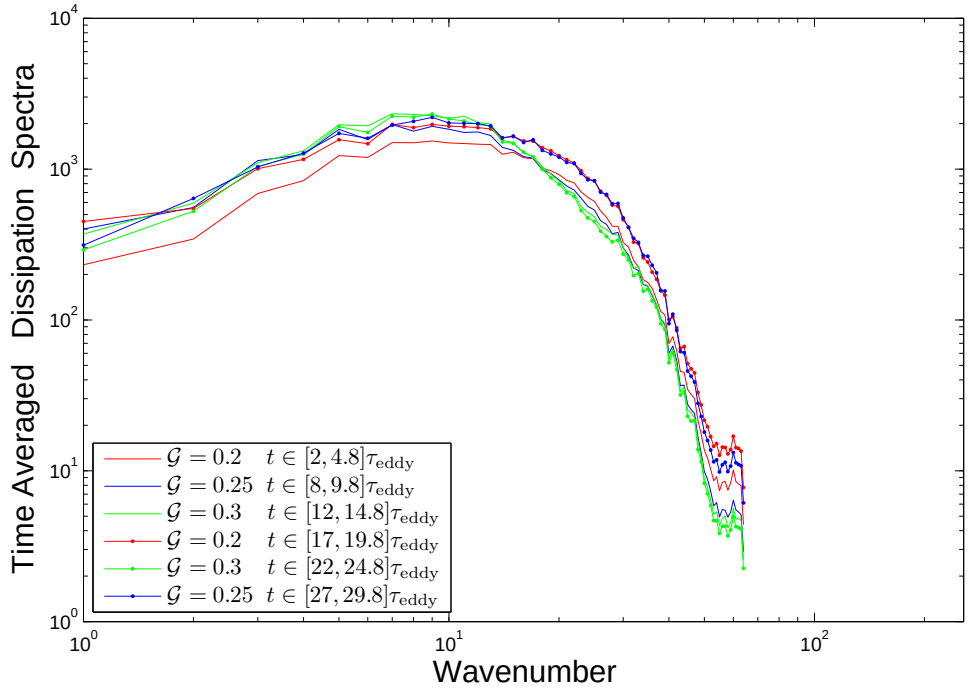

(a) $\kappa_{\max} = 64$

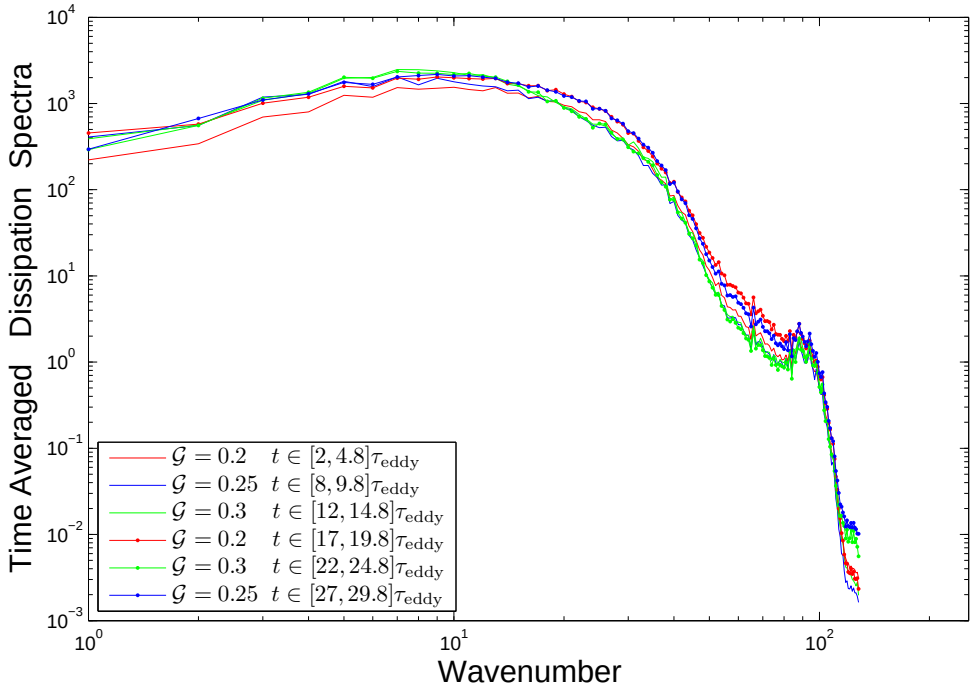

(b) $\kappa_{\max} = 128$

Figure 4.9: Time-averaged dissipation spectra of time-frames with $\kappa_{\max} = 64, 128$ for variable $\mathcal{G}$ SCALES, EE method with $\nu_\epsilon = 0.1$, $\epsilon \in [0.2, 0.5]$, ν= 0.09, C_f= 6.$\bar{6}$, Re_λ= 70, 256^3.

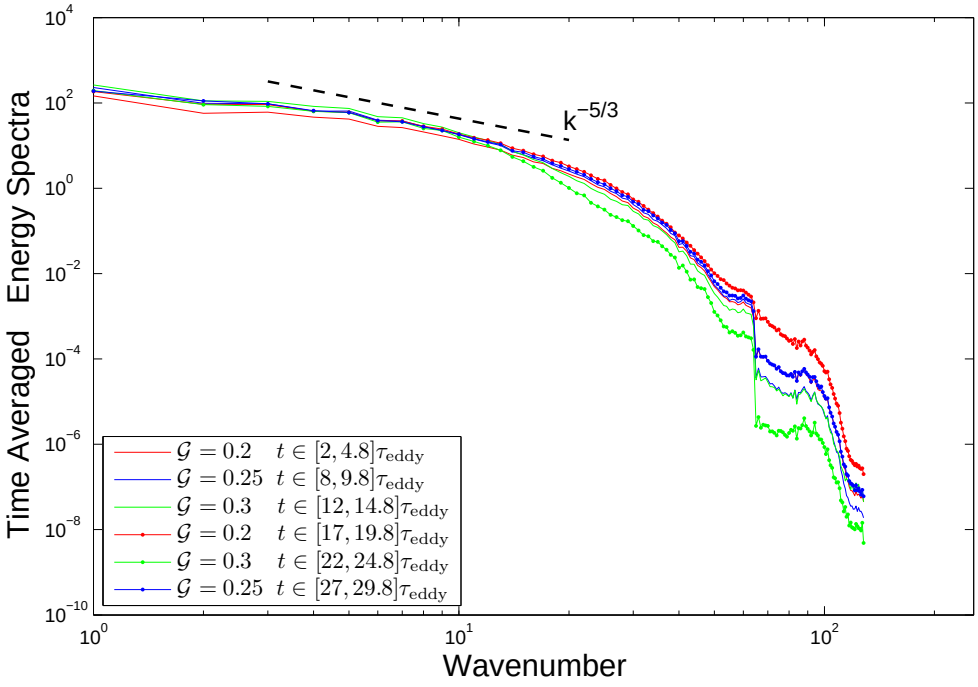

(a) Energy spectra

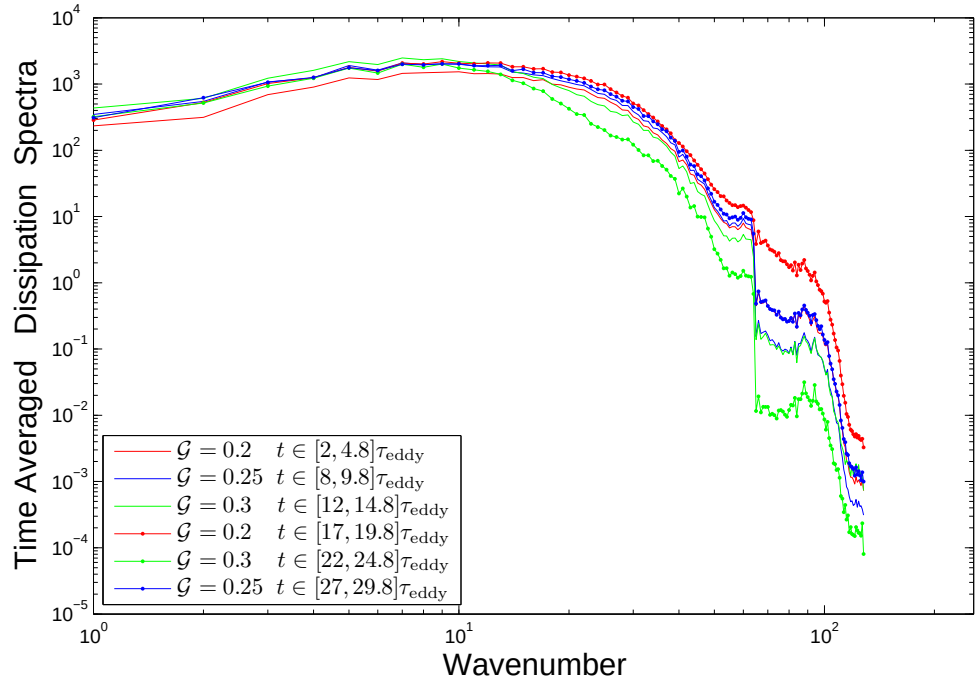

(b) Dissipation spectra

Figure 4.10: Time-averaged energy and dissipation spectra for variable $\mathcal{G}$ SCALES, EE method with $\nu_\epsilon = 0.05$, $\epsilon \in [0.2, 0.5]$, ν= 0.09, C_f= $6.\overline{6}$, Re_λ= 70, 256^3.

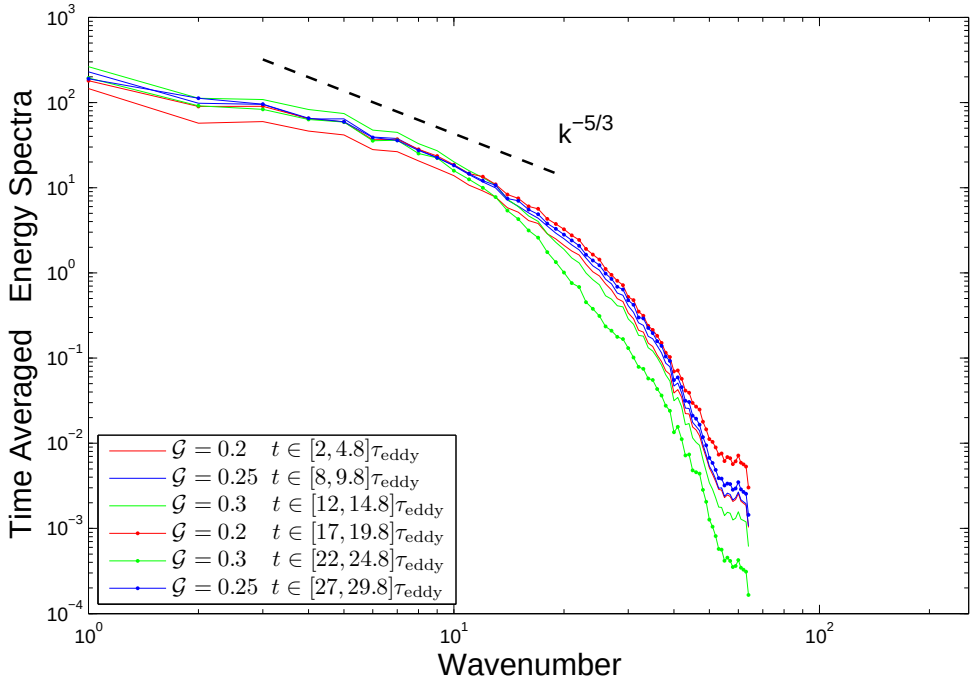

(a) $\kappa_{\max} = 64$

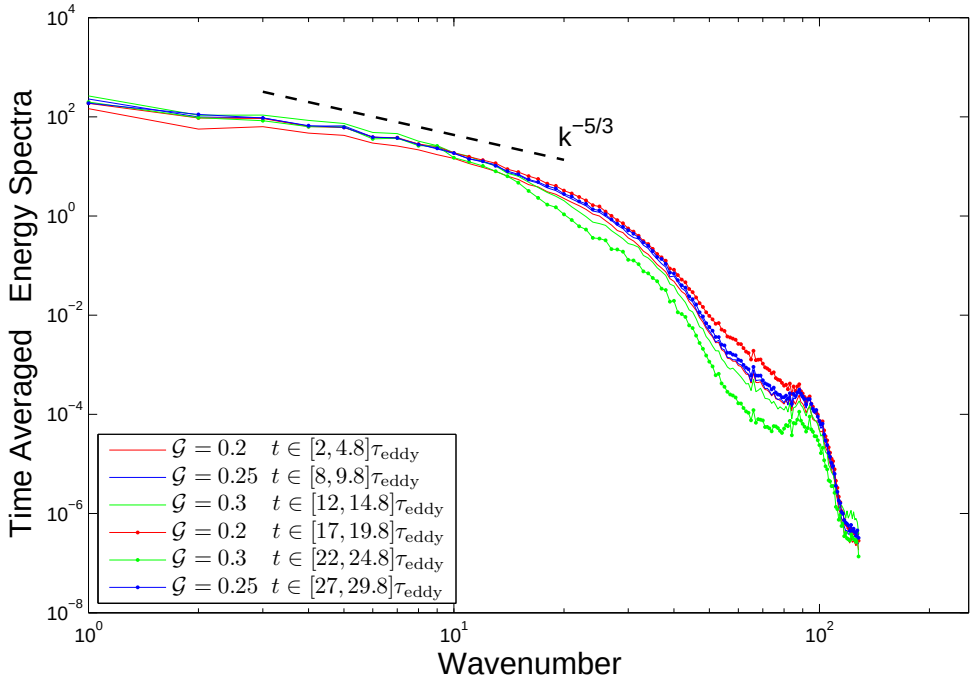

(b) $\kappa_{\max} = 128$

Figure 4.11: Time-averaged energy spectra of time-frames with $\kappa_{\max} = 64, 128$ for variable $\mathcal{G}$ SCALES, EE method with $\nu_\epsilon = 0.05$, $\epsilon \in [0.2, 0.5]$, ν= 0.09, C_f= $6.\bar{6}$, Re_λ= 70, 256^3.

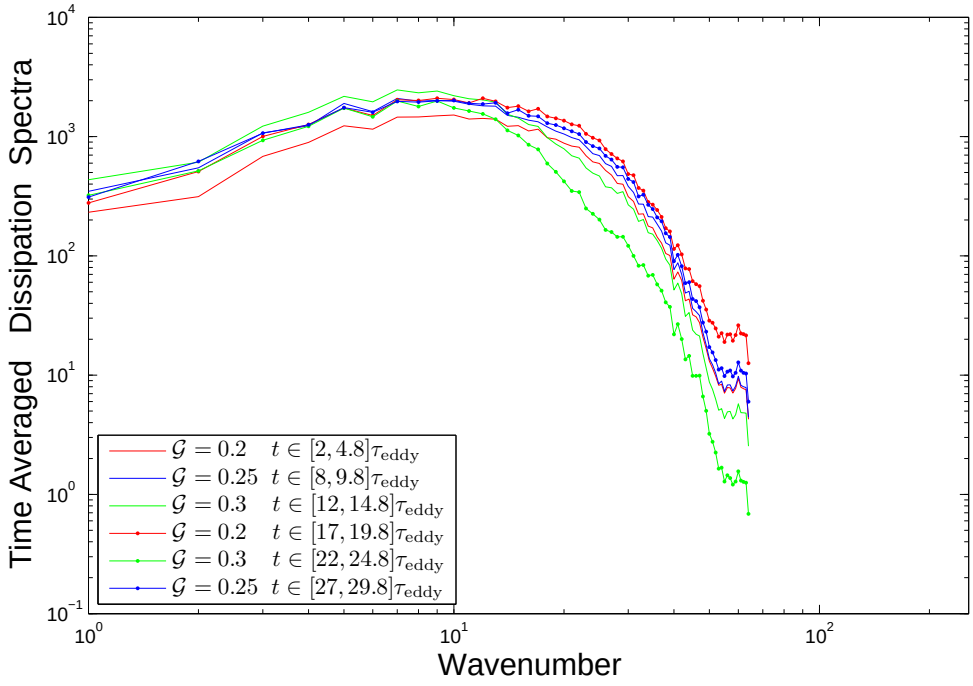

(a) $\kappa_{\max} = 64$

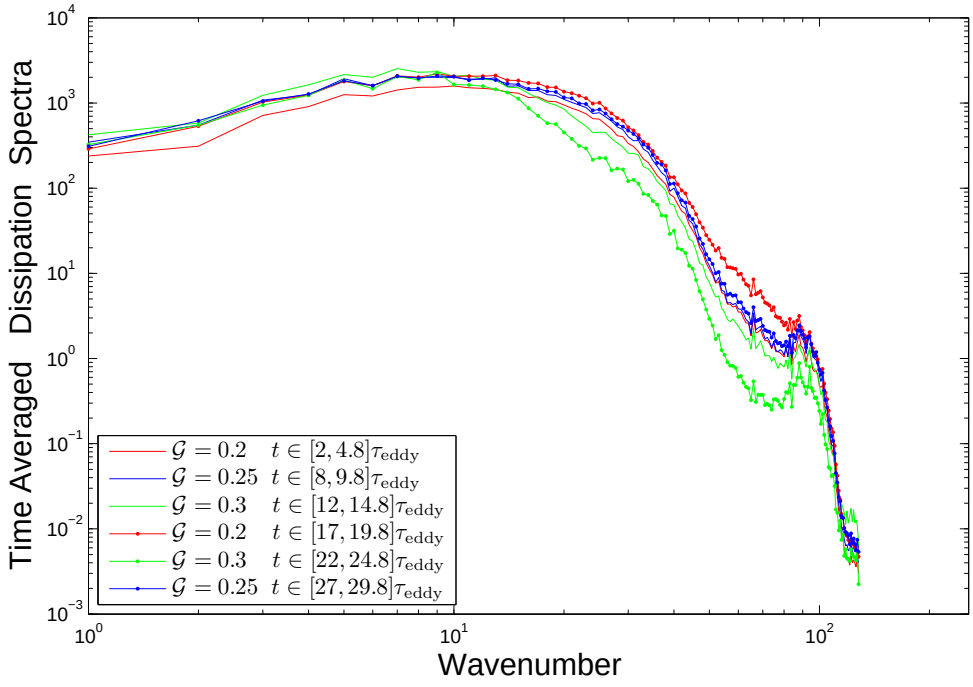

(b) $\kappa_{\max} = 128$

Figure 4.12: Time-averaged dissipation spectra of time-frames with $\kappa_{\max} = 64, 128$ for variable $\mathcal{G}$ SCALES, EE method with $\nu_\epsilon = 0.05$, $\epsilon \in [0.2, 0.5]$, ν= 0.09, C_f= $6.\bar{6}$, Re_λ= 70, 256^3.

Chapter 5

Parallel Adaptive Wavelet Collocation Method for PDEs

In spite of the fact that the parallel AWCM has been completed and become fully functional during the course of this study and has been a major part of the novel numerical efforts covered in this dissertation, this parallelization of AWCM was initiated prior to the current work and was not fully covered during the term of the current effort. However, the scalability and speedup studies of the parallel AWCM are performed for the first time within the the scope of this dissertation.

The first aforementioned objective of large-scale wavelet-based hybrid turbulence simulation has been developed and is addressed in Chapters 3 and 4. However, both large-scale simulations and large Reynolds numbers studies require scalable parallel code. Therefore, another main objective of this dissertation is to develop a parallel multi-functional adaptive wavelet-based solver that can be used for variable fidelity hierarchical wavelet-based turbulence simulations.

In order to make a substantial progress in the development of computational capabilities for massively parallel distributed systems, the development efforts have been focused on two main fronts: namely improving data structure for faster access and developing scalable parallel computational capabilities. The original serial algorithm of the AWCM [44, 45, 46] is first enhanced by means of a robust tree structure database, which is well suited for parallel computation, and then the algorithm has been parallelized.

5.1 Wavelet Transform and AWCM

The second-generation wavelets are constructed on an interval Ω with arbitrary distribution of grid (collocation) points. The construction is performed on an arbitrary set of interpolating points, $\{x_k^j \in \Omega\}$, which are used to form a set of nested grids

$$\mathcal{G}^j = \left\{ x_k^j \in \Omega : \; x_k^j = x_{2k}^{j+1}, \; k \in \mathcal{K}^j \right\}, \quad j \in \mathcal{J}, \tag{5.1}$$

where x_k^j are the grid points of the j level of resolution. The restriction $x_k^j = x_{2k}^{j+1}$ guarantees the nestedness of the grids, i.e. $\mathcal{G}^j \subset \mathcal{G}^{j+1}$.

The full 1-D forward second-generation wavelet transform includes an update stage following the predict stage as follows:

$$\text{Predict Stage: } d_k^j = \frac{1}{2}\left(c_{2k+1}^{j+1} - \sum_l w_{k,l}^j c_{2k+2l}^{j+1} \right), \tag{5.2}$$

$$\text{Update Stage: } c_k^j = c_{2k}^{j+1} + \sum_l \widetilde{w}_{k,l}^j d_{k+l}^j. \tag{5.3}$$

The corresponding 1-D inverse second-generation wavelet transform is

$$\text{Inverse Update Stage: } c_{2k}^{j+1} = c_k^j - \sum_l \widetilde{w}_{k,l}^j d_{k+l}^j, \tag{5.4}$$

$$\text{Inverse Predict Stage: } c_{2k+1}^{j+1} = 2d_k^j + \sum_l w_{k,l}^j c_{2k+2l}^{j+1}, \tag{5.5}$$

where $w_{k,l}^j$ and $\widetilde{w}_{k,l}^j$ are coefficients associated with two stages of wavelet transform; c_k^j and d_k^j are the function values and wavelet coefficient at location k on level j on the defined dyadic nested grid. For the details, the readers are referred to [42, 43, 45].

The first stage of forward transform is called a predict stage, since the wavelet coefficients are calculated by predicting the function value using the interpolated points on the next coarser level. The predict stage of the 1-D second-generation wavelet forward transform is illustrated in Figure 5.2(a). The c_k^j-values that get carried down to the next lower level of resolution are then updated using the wavelet coefficients that were calculated during the predict stage. The update

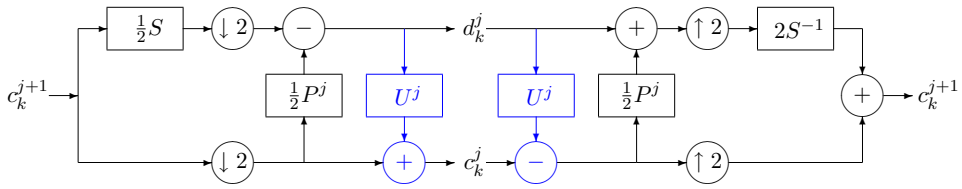

Figure 5.1: Block diagram of lifted interpolating wavelet transform.

stage, Figure 5.2(b), guarantees that the wavelet interpolating functions have zero mean, which ensures an accurate transform. In fact, the interpolating wavelets of order N when using the update stage have N vanishing moments. For the inverse wavelet transform, the order of operations is reversed and the inverse wavelet transform is performed from low to high levels of resolution as opposed to high to low for the forward wavelet transform.

The block diagram for one step wavelet transform is shown in Figure 5.1, where S and S^{-1} denote respectively the delay and advance operators, i.e. $Sf_k = f_{k-1}$ and $S^{-1}f_k = f_{k+1}$, $(\downarrow 2)$ denotes the downsampling (decimation) operator which removes odd-numbered components from the signal, while U^j and P^j denote respectively lifting and dual lifting operators (P stands for predict and U stands for update).

The second-generation scaling function ϕ_m^j can be formally defined by setting $c_k^j = \delta_{k,m}$ $\forall k \in \mathcal{K}^j$ and $d_l^{j'} = 0$ $\forall l \in \mathcal{L}^{j'}$, $\forall j' \geq j$, and then recursively performing the inverse wavelet transform up to an arbitrary high level of resolution J. This procedure will result in a scaling function ϕ_k^j sampled at the locations x_k^J. Analogously, second-generation wavelet ψ_l^j can be formally defined by assuming $d_m^{j'} = \delta_{j',j}\delta_{l,m}$ $\forall l \in \mathcal{L}^j$, $\forall j' \geq j$ and $c_k^j = 0$ $\forall k \in \mathcal{K}^j$, and then recursively performing the inverse wavelet transform up to an arbitrary high level of resolution J. Now using the linear superposition it is easy to show that on each level of resolution J a function $f(x)$ can be approximated as

$$f^J(x) = \sum_{k \in \mathcal{K}^1} c_k^1 \phi_k^1(x) + \sum_{j=1}^{J-1} \sum_{l \in \mathcal{L}^j} d_l^j \psi_l^j(x). \tag{5.6}$$

The described wavelet construction can be easily extended to multiple dimensions using tensor product, e.g. the three-dimensional tensor product wavelets are given by

$$\psi^{\mu,j}_{i,k,l}(\mathbf{x}) = \begin{cases} \psi^j_i(x_1)\,\phi^j_k(x_2)\,\phi^j_l(x_3) & \mu = 1 \\ \psi^j_i(x_1)\,\phi^j_k(x_2)\,\psi^j_l(x_3) & \mu = 2 \\ \psi^j_i(x_1)\,\psi^j_k(x_2)\,\phi^j_l(x_3) & \mu = 3 \\ \phi^j_i(x_1)\,\phi^j_k(x_2)\,\psi^j_l(x_3) & \mu = 5 \\ \phi^j_i(x_1)\,\psi^j_k(x_2)\,\phi^j_l(x_3) & \mu = 6 \\ \phi^j_i(x_1)\,\psi^j_k(x_2)\,\psi^j_l(x_3) & \mu = 4 \\ \psi^j_i(x_1)\,\psi^j_k(x_2)\,\psi^j_l(x_3) & \mu = 7 \end{cases} \tag{5.7}$$

with three-dimensional scaling function $\phi^j_{i,k,l}(\mathbf{x}) = \phi^j_i(x_1)\,\phi^j_k(x_2)\,\phi^j_l(x_3)$, where $\psi^j_i(x_1)$, $\psi^j_k(x_2)$, $\psi^j_l(x_3)$, $\phi^j_i(x_1)$, $\phi^j_k(x_2)$, $\phi^j_l(x_3)$ correspond to arbitrary one-dimensional wavelets and scaling functions and $\mathbf{x} = (x_1, x_2, x_3)$. The d-dimensional tensor product wavelets are constructed analogously, with exception that there are $2^d - 1$ distinctive d-dimensional wavelets. Note that in the case of d-dimensional tensor product wavelets, the one step of forward wavelet transform consists of the sequential application of one-dimensional wavelet transform starting from x_1 direction, while the one step of inverse wavelet transform consists of the sequential application of one-dimensional inverse wavelet transform in reverse order starting from x_d direction.

5.2 Asynchronous Parallel Second-Generation Wavelet Transform

As explained in the previous section and illustrated in Figure 5.2(b), the update stage at each level of resolution for both forward and inverse wavelet-transform necessitates inclusion of grid points at the higher level of resolution. While to predict these added points at the higher level of resolution, again more points on the lower level of resolution will be included.

Figures 5.2(c-d) show a series of predict, update, and corresponding required extra stages on an adaptive grid for one complete forward wavelet transform. Figure 5.2(c) is the schematics of predict stages at levels $j+1$ and j separately, while the update stages at levels j and $j-1$ are

shown by Figure 5.2(d). The sequence illustrated by these four diagrams starts with predicting a point on level $j+1$ belonging to a target processor (processor red), Figure 5.2(c). This predict stage requires four points at level j, which one of them belongs to the immediate neighboring processor on the right (processor blue). Besides, one of the three required points from processor red itself belongs to the lower level $j-1$.[1] Since $j-1$ is the lowest level of resolution in this illustration, this point (marked green) needs to updated as shown in the right diagram of Figure 5.2(c). As a result, in order to predict one point on level $j+1$ from processor red, four points from processor blue are required.

This procedure becomes extremely complicated for the update stage as demonstrated in Figure 5.2(d), which shows that "two extra predict stages at level $j+1$ on the processor blue" are required for "updating four points at level j on processor red". By descending the level of resolution, the number of extra stages required for update grows fast: for updating three points at level $j-1$ on processor red, two extra predicts as well as four extra updates are necessary at level j. This recursive nature rapidly thickens the set of points required to perform one sequence of predict-update.

For problems of arbitrary dimension (greater than one), the wavelet transform is performed by transforming each dimension independently. As the levels of resolution are descended (or ascended in the inverse wavelet transform) in one dimension, the transform is completed over the entire domain at that level of resolution. In order to completely and accurately perform the update stage of the wavelet transform (obtaining the correct c_k^j-values at each level of resolution), the points must be synchronized across subdomain boundaries. The points lying outside of the boundaries of each processor are buffer zones added for proper interpolation. These points, which are required to be synchronized, are shown in Figures 5.2(c-d) by the blue and green markers. That is to say, in this illustration, the entire set of blue and green points must be communicated to the processor red in order to perform one complete forward wavelet transform (including both predict and update stages) on an adaptive grid with only one point at the highest level of resolution.

[1] On these diagrams, at each level of resolution, points belonging to the level itself and all levels below are shown.

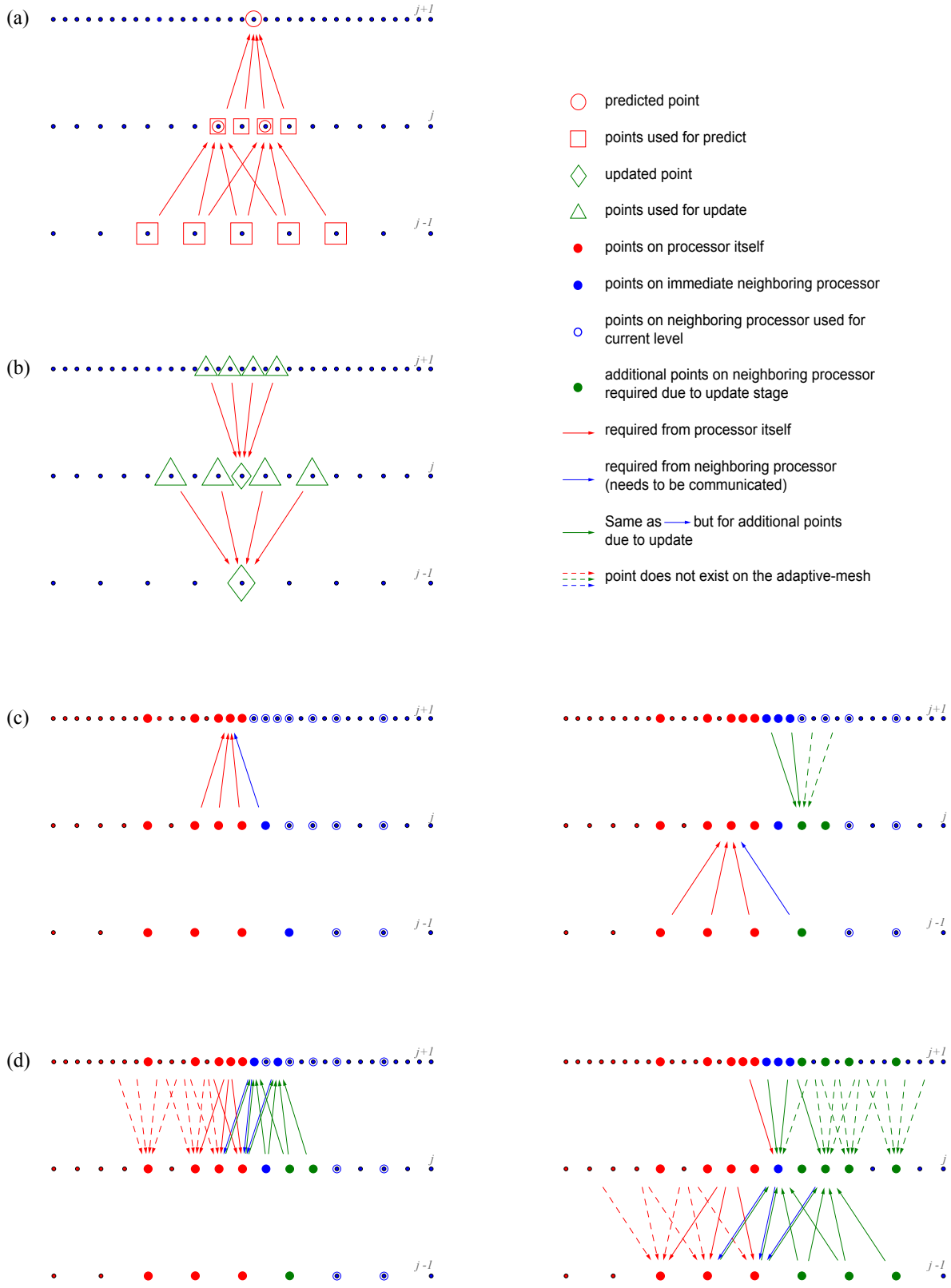

Figure 5.2: Illustration of predict and update stages of the forward wavelet transform. (a) Predict stage dependency; (b) Update stage dependency; (c) Predict stages at levels $j+1$ and j; (d) Update stage at levels j and $j-1$.

Therefore, for asynchronous wavelet transform, i.e. with only one synchronization of the buffer-zone, the wavelet coefficients at the lower level of resolution in the buffer-zone need to be calculated, necessitating the inclusion of grid points at higher level of resolution required for the update stage, which results in synchronization of the entire domain on all processors to complete the update stage. This is impractical because neighboring points on different levels of resolution could end up being on different processors, which drastically complicate the logic of the parallel algorithm plus loses the efficiency.

Thus, asynchronous wavelet transform with update stage is impractical for parallel implementation, alternatively, one can perform synchronization at every level of resolution after each update stage and/or predict stage depending on the algorithm as well as for every dimension. Note that the more synchronization stages are implemented, the smaller the size of the buffer zone, where wavelet coefficients need to be synchronized. Therefore, for a d-dimensional problem with J levels of resolution, $(2)dj$ communication stages are required to simply perform one forward wavelet transform, where 2 is put in parenthesis depending if synchronization is done for both predict and update stages or just once after update. The inverse wavelet transform requires the same amount of stages resulting in doubling synchronization stages for one time-step while using the AWCM. It is expected that the cost of so much communication could be a bottleneck, not mentioning the difficulties of load balancing at each level of resolution.

Five different parallel extensions have been investigated with the idea that the performance of these different methods would shed light on how to modify the wavelet transform so that its parallel implementation is fully optimized. These extensions include synchronization at each update and predict stages, only at predict stages, as well as modifying wavelet transform so that the wavelets close to the inter-processor boundaries do not need to be updated, and finally, skipping the update stage in the entire domain.

It was found that the most efficient solution is to skip the update stage over the entire computational domain. This allows to develop asynchronous wavelet-transform, i.e. synchronizing the data in the buffer-zone only at the beginning of the transform and performing wavelet transform

inside and in the buffer-zone. The ability of performing wavelet transform in the buffer-zone is guaranteed by the reconstruction check procedure discussed in Section 5.4. In addition, due to the lack of the update stage, the computational time is also cut down since the algorithm takes half as many steps. The main drawback for this method is a loss of zero-mean properties of the interpolating wavelet.

To easily/visually address the difference between the serial and the no-update algorithm, the parts that are **not** carried out in the **parallel** algorithm are colored **blue** in the Equations (5.2 – 5.5). In the block diagram of the 1-D one-step second-generation wavelet transform (Figure 5.1) also, the the part that is **not** carried out in the **parallel** algorithm is colored **blue**.

5.3 Data Structure

A dynamic arbitrary dimension tree structure database has been constructed: binary in 1D, quad-tree in 2D, and octree in 3D, Figure 5.3. This tree like data structure has been implemented for wavelet coefficient storage and retrieval. Trees are organized as forward link-list with a deterministic path determined by the global non-adaptive coordinates starting from the root of the tree. Roots of the tree are specified on a given resolution and trees could be empty. For parallel implementation, the trees are the smallest quantum for the data migration.

In order to decrease number of cache-misses during tree traverse, nodes of each two levels are stored together starting from the finest level of resolution.To summarize:

(1) Nodes are arranged by levels (to simplify access during wavelet transforms) and in a cache friendly manner (to speed up the access),

(2) In a tree of dimension d, a node of level j has $2^d - 1$ links to the nodes of higher level $j+1$,

(3) Each node of level j is also considered as a node of level $j+1, j+2, \cdots, J_{\max}$.

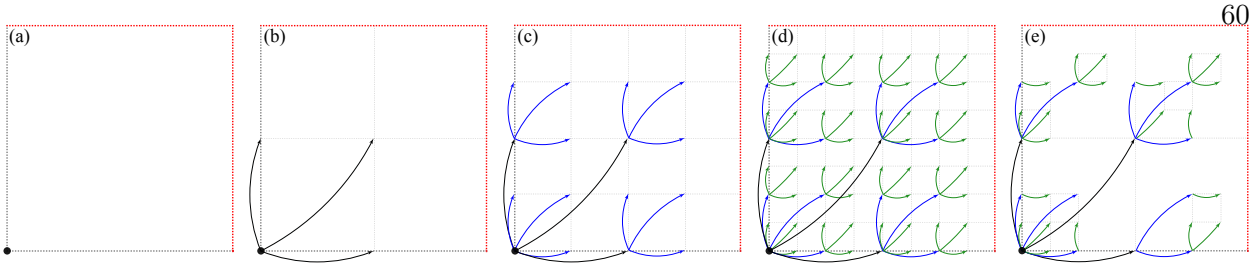

Figure 5.3: Possible links from a tree root node. Each level goes to $2^d - 1$ nodes of the next level + itself: totaly 2^d. Tree-root is marked by filled black circle. Black links show the first hierarchy ($j = J_{\text{root}} + 1$). Blue ($j = J_{\text{root}} + 2$) and Green (j=$J_{\text{root}} + 3$) links show the second and third hierarchial links respectively. The right and top edges belong to the neighboring trees. (a) Empty tree, $j = J_{\text{root}}$; (b) All possible links to completely fill level $j = J_{\text{root}} + 1$; (c) All possible links to completely fill level $j = J_{\text{root}} + 2$; (d) All possible links to completely fill a tree with $J_{\text{root}} = J_{\max} - 3$: a full non-adaptive grid; (e) Only links required for the illustrated adaptive grid of a tree with $J_{\text{root}} = J_{\max} - 3$.

For data access based on coordinates, the length of the path to a data point at a level $J_{\text{root}} + j$ is j. The cost of data access to all points at a level $J_{\text{root}} + j$ is $(2^d - 1)2^{(j-1)d}\mathfrak{N}_{\text{root}}(j + 1)$, where $\mathfrak{N}_{\text{root}}$ is the number of points on the tree root level, J_{root}, i.e. $\mathfrak{N}_{\text{root}} = \mathbf{M}2^{J_{\text{root}}-1}$. The base grid size of $\mathbf{M} = [m_x, m_y, m_z]$ and tree root level of J_{root} are user defined input parameters. At the limit when j is large, it can be seen that $\mathfrak{N} \cong \mathfrak{N}_{\text{root}}2^{jd}$, which implies that $j \cong \frac{1}{d}\log_2 \frac{\mathfrak{N}}{\mathfrak{N}_{\text{root}}}$. Therefore, the overall cost of data access to the tree is $O(\mathfrak{N} \log \mathfrak{N})$.

In addition, for faster access, the pointers to the data are stored in orthogonal list based on wavelet family, location in relation to the rectangular computational domain (internal, face, edge, corner), level of resolution, level of derivative calculation. This makes the cost of direct access to the data $O(\mathfrak{N})$.

Trees and the corresponding data are orthogonally distributed among processors; however, in order to facilitate the wavelet-transform and the derivative calculations, each processor has identical matrix of tree-roots that are marked by the processor-rank where the actual data are stored on.

All the trees that belong to processor itself hereafter are called internal-zone trees and their corresponding points are called internal-zone points. All the trees that do not belong to the processors itself hereafter are called buffer-zone trees and the points belonging to these buffer-trees are

called buffer-zone points. It should be noted that the buffer-zone trees are always a subset of the trees on the corresponding processor and consist of the points that are necessary for asynchronous wavelet-transform that is discussed in Section 5.2. Each processor should have at least one tree with the possibility of some of them being empty. Each tree-root also has descriptor indicating to which process it belongs.

5.4 Grid Adaptation

Significant, adjacent, ghost points/zone as well as the grid adaptation methodology based on the wavelet threshold filtering (WTF) and the corresponding reconstruction check procedure are explained in the following. In 1-D wavelet threshold filtering, in order to predict the wavelet coefficient d_k^j, only the values of c_{2k+2l}^{j+1} and c_{2k+1}^{j+1} are required. The the wavelet coefficient above the threshold value ϵ are kept and wavelet coefficients below threshold value are set to zero.

Analogously, in the higher dimensional case, the only difference is that the d-dimensional wavelet transform consists of the sequential application of d one-dimensional wavelet transforms in x_i, $i = 1, \ldots, d$, directions. Hence, to find the grid points that are necessary for the calculation of the wavelet coefficient $d_{\mathbf{l}}^{\mu,j}$, we start with the collocation point associated with $d_{\mathbf{l}}^{\mu,j}$ and recursively, $i = d, \ldots, 1$, add points that are needed to perform one step of the one-dimensional wavelet transform in the x_i direction at the locations that are added to perform the one-dimensional wavelet transforms in x_l, $l = i+1, \ldots, d$, directions. At the end of this recursive procedure, we will have a minimal set of grid points that are necessary for calculation of wavelet coefficient $d_{\mathbf{l}}^{\mu,j}$ provided that wavelet coefficients at other locations are either zero or negligible (below an a priori prescribed threshold). Figure 5.4 illustrates the minimal set of grid points that are necessary for calculation of wavelet coefficient $d_{\mathbf{l}}^{\mu,j}$ belonging to three different families of wavelets, i.e. $\mu = 1, 3$. Thus, if we a priori know what wavelet coefficients are zero or negligible, we can disregard the values of the function at these points.

Algorithm 1 Reconstruction Check Procedure (RCP) for the wavelet transform: $\mathcal{M}_{p,p}^{S+A} \xrightarrow{\text{RCP}} \mathcal{M}_{p,r}^{S+A}$

for $\forall p = 0 : 1 : \mathsf{n_p} - 1$
  set $\mathcal{M}_{p,r\neq p}^{S+A} = \varnothing$ at $j = J$
  for all levels $j = J - 1 : -1 : 1$
    extend mask $\mathcal{M}_{p,r}^{S+A}$ to include the ancestry points at level j
  end
end

The pseudocode for the perfect reconstruction check procedure is shown in Algorithm 1. At the end of this procedure, we have the complete mask $\mathcal{M}_{p,r}^{S+A}$ from which we can easily construct a set of nested adaptive computational grids $\mathcal{G}_{\geq}^{j}$. The perfect reconstruction check procedure guarantees that all wavelet coefficients obtained by performing the wavelet transform on the adapted grid are the same as those found by performing the wavelet transform of $u_{\geq}(\mathbf{x})$ on the complete grid.

In order to be able to perform asynchronous wavelet-transform, all the data at the ancestry points necessary to perform the wavelet-transform at the points on a given processor marked by $\mathcal{M}_{p,p}^{S+A}$ are required including points that are stored on different processors. In order to construct the necessary points marked by $\mathcal{M}_{p,r\neq p}^{S+A}$, the reconstruction check procedure on $\mathcal{M}_{p,p}^{S+A}$ is performed on each processors as it is serial algorithm. The data at the points on the resulting masks $\mathcal{M}_{p,r\neq p}^{S+A}$ need to be synchronized among processors. Once synchronized, the wavelet-transform on each processor can be proceeded as in the case of the regular serial algorithm.

Note that for some processor r, $\mathcal{M}_{p,r\neq p}^{S+A}$ could be an empty set; however, the identity $\mathcal{M}_{p,r\neq p}^{S} = \varnothing$ always holds. Also, $\mathbf{u}_{\mathbf{k}}^{m}$ and $\mathcal{G}_{\geq}^{m}$ are local on each processor.

Both internal and buffer-zone masks for significant, adjacent and ghost points can be visualized by Figure 5.5: for instance, red-point is $\mathcal{M}_{0,0}^{S+A}$; all the orange-points on the green-background are reconstruction on $\mathcal{M}_{0,0}^{S+A}$ while all the orange-points on the blue-background are reconstruction on $\mathcal{M}_{0,1}^{S+A}$; all the violet-points on the green-background are $\mathcal{M}_{0,0}^{G}$ while all the violet-points on the blue-background represent $\mathcal{M}_{0,1}^{G}$. Figure 5.6 presents an illustration of the nodes that need to be synchronized, $\mathcal{M}_{p,r\neq p}^{S+A}$.

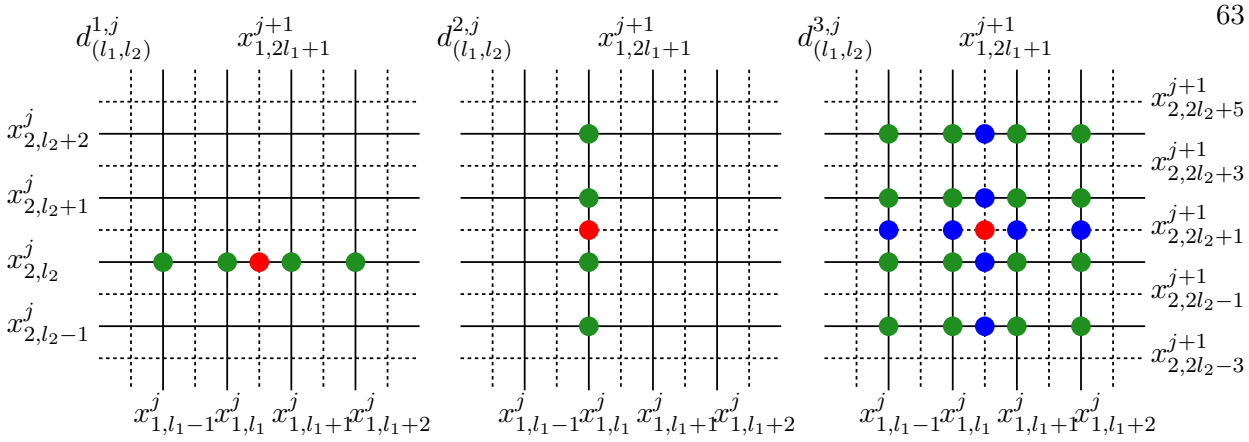

Figure 5.4: Points at the coarser level j (marked •) and finer level $j+1$ (marked •) where $c^{j+1}_{\mathbf{k}}$ are needed for calculation of the wavelet coefficient $d^{\mu,j}_{\mathbf{l}}$, $\mu = 1, 3$ (marked •) for two-dimensional wavelet transform with $N = 4$.

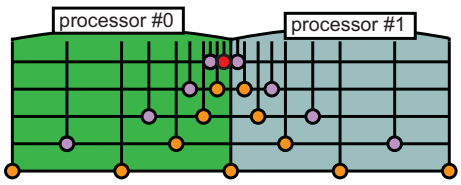

Figure 5.5: Illustration of Zones and Masks (includes nodes required for wavelet transform and derivatives) in parallel. Red-wavelet above the threshold ($\mathcal{M}^{S+A}_{0,0}$), Orange-nearest neighbors to capture evolving solution (reconstruction masks $\mathcal{M}^{S+A}_{0,0}$ and $\mathcal{M}^{S+A}_{0,1}$), Violet-nodes required for derivatives (Ghost masks $\mathcal{M}^{G}_{0,0}$ and $\mathcal{M}^{G}_{0,1}$). Courtesy of Alexei Vezolainen.

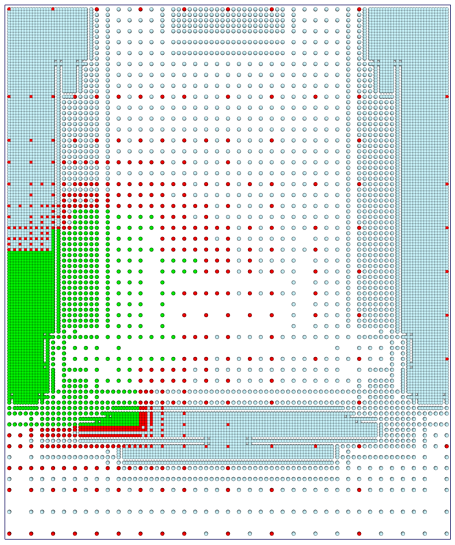

Figure 5.6: Parallel Wavelet Transform: Green-one processor ($\mathcal{M}^{S+A}_{p,p}$), Red-nodes used in communication (to be synchronized, $\mathcal{M}^{S+A}_{p,r\neq p}$), Blue-rest of processors. Courtesy of Alexei Vezolainen.

5.5 Calculation of Derivatives on the Adapted Grid

The differentiation procedure for obtaining derivatives of a function from its values at collocation points is based on the interpolating properties of second generation wavelets. It is recalled that wavelet coefficients $d_{\mathbf{l}}^{\mu,j}$ measure the difference between the approximation of the function at the $j+1$ level of resolution and its representation at the j level of resolution. Thus, if there are no points in the immediate vicinity of a grid point $\mathbf{x}_{\mathbf{k}}^{j}$, i.e. $|d_{\mathbf{m}}^{\mu,j}| < \epsilon$ for all the neighboring points, and points $\mathbf{x}_{(2k_1\pm1,2k_2\pm1)}^{j+1}$ are not present in $\mathcal{G}_{\geq}^{j+1}$, then there exists some neighborhood of $\mathbf{x}_{\mathbf{k}}^{j}$, $\Omega_{\mathbf{k}}^{j}$, where the actual function is well approximated by a wavelet interpolant based on $c_{\mathbf{m}}^{j}$ ($\mathbf{m} \in \mathcal{K}^{j}$), i.e.

$$\left| u(\mathbf{x}) - \sum_{\mathbf{m}\in\mathcal{K}^{j}} c_{\mathbf{m}}^{j}\phi_{\mathbf{m}}^{j}(\mathbf{x}) \right| \leq C_4\epsilon, \quad \mathbf{x} \in \Omega_{\mathbf{k}}^{j}. \tag{5.8}$$

Thus, differentiating this interpolant will give us the value of the derivative of the function at that particular location. Rewriting this interpolant as local Lagrange polynomial of order N, i.e. the same order as the wavelet, differentiating the polynomial, and evaluating it at $\mathbf{x}_{\mathbf{k}}^{j}$ location would result in local finite difference operator that uses the neighboring points of the interpolant on level j. Let us denote by $\mathcal{D}_{p}^{j}$ a collection of such points at each level of resolution for each processor $p \in \{0, \cdots, \mathsf{n_p} - 1\}$. $\mathcal{D}_{p}^{j}$ is the set of the points that not only they belong to significant+adjacent mask of each processor but also the differentiation is taken on them at level j, i.e.

$$\mathcal{D}_{p}^{j} = \left\{ x_k^j \in \Omega : \; x_k^j \in \mathcal{M}_{p,p}^{S+A}, \text{differentiation taken at level } j \right\}. \tag{5.9}$$

Note that $\mathcal{D}_{p}^{j}$ is an orthogonal set, $\bigoplus_{j=1}^{J} \mathcal{D}_{p}^{j} = \mathcal{M}_{p,p}^{S+A}$.

The pseudocode for the procedure for finding derivatives at all grid points is given in Algorithm 2. At the end of this procedure, we will have derivatives of the function at all grid points. The computational cost of calculating spatial derivatives will be roughly the same as the cost of forward and inverse wavelet transforms. For the details of the accuracy of this differentiation procedure, the readers are referred to [44, 45].

Algorithm 2 Calculation of derivatives on the adapted grid.

for $\forall p = 0 : 1 : \mathsf{n_p} - 1$
  perform forward wavelet transform for each component of $\mathbf{u}_{\mathbf{k}}^m$ on $\mathcal{M}_{p,r}^{S+A}$
  for all levels $j = 1 : 1 : J - 1$
    perform one step of inverse wavelet transform for level j on $\mathcal{M}_{p,r}^{S+A+G}$
    find derivatives at grid points that belong to $\mathcal{D}_p^j$
  end
end

5.6 Data migration

The mask of points $\mathcal{M}_{p,r\neq p}^{S+A}$ for either transform or derivative-calculation are constructed separately and then communicated by means of either all-to-all or one-to-one communication techniques.

5.7 Domain Partitioning and Dynamic Load Balancing

Several partitioning approaches with different user controls are implemented, Figure 5.7. More advanced Zoltan [2, 3, 4, 5, 11, 12] library based partitions provide nearly optimal load balancing. In short, for the geometric simultaneous partitioning all spatial directions of the domain are divided simultaneously. The major deficiency of that approach is poor load balancing for a non-uniform wavelet distribution. For the geometric sequential partitioning, the domain is subdivided by planes normal to the first axis on rounded to the nearest integer $\sqrt[d]{P}$ sub-domains, where d is the problem dimension and P is the total number of processors. The available P processors are distributed among these sub-domain according to the number of active wavelets inside each of the sub-domains. This recursion step is repeated d times to get the final partitioning. It may deliver not quite an optimal load balancing, though it may be more usable for non-uniform wavelet distributions across the domain. For significantly non-uniform wavelet distribution, the domain is partitioned using Zoltan partitioning library by Sandia National Laboratories, Figure 5.7.

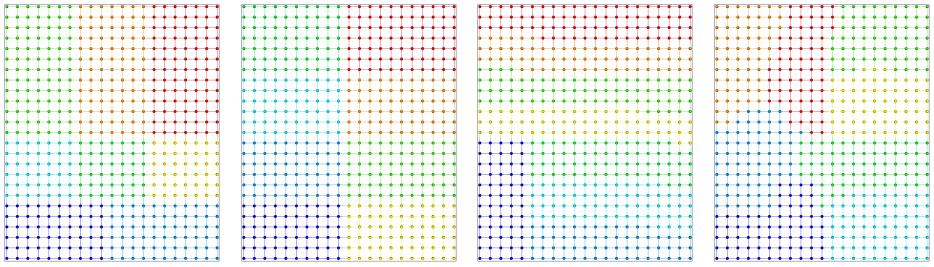

(a) (b) (c) (d)

Figure 5.7: Domain partitioning: (a) geometric simultaneous, (b) geometric sequential, (c) Zoltan geometric, (d) Zoltan hypergraph. Courtesy of Alexei Vezolainen.

Dynamic load balancing (DLB) is implemented via domain repartitioning during grid adaptation step and reassigning tree data structure nodes to the appropriate processors. User provides an imbalance tolerance vector to trigger the repartitioning if necessary. Depending on the imbalance of wavelet distribution a different kind of repartitioning is performed. Highly imbalanced data are partitioned without considering initial decomposition, moderately imbalanced repartitioned while trying to stay close to the current decomposition, and nearly balanced will be refined by small changes only. Three dimensional examples of dynamic load balancing for the 3D simulations of the Convection-Diffusion of rotating ellipsoids as well as SCALES of linearly forced homogeneous turbulence on 2048^3 are presented in Figures 5.8 and 5.9.

5.8 Parallel AWCM

Algorithm 3 illustrates a summary of major components of both serial and parallel AWCM. In Algorithm 3, the operations that are **only** carried out in the **parallel** algorithm are colored **blue**. The operator $\xrightarrow{\text{A}}$ is the adjacent (safety) zone inclusion that extends the significant mask on each rank $\mathcal{M}_{p,p}^{S}$ to its corresponding significant+adjacent mask $\mathcal{M}_{p,r}^{S+A}$, which may belong to any rank $r = 0, \cdots, \mathsf{n_p} - 1$. Similarly, the operator $\xrightarrow{\text{RCP}}$ is the reconstruction check procedure on $\mathcal{M}_{p,p}^{S+A}$ to extend it to $\mathcal{M}_{p,r}^{S+A}$.

Algorithm 3 Adaptive Wavelet Collocation Method (AWCM).

for $\forall \mathsf{p} = 0:1:\mathsf{n_p}-1$
  initial guess $(m=0)$**:** $\mathbf{u}_{\mathbf{k}}^{m}$ and $\mathcal{G}_{\geq}^{m}$
end

while $m=0$ **or** $\left\{ m \geqslant 1 \text{ and } \left\{ \underbrace{\left[\mathcal{G}_{\geq}^{m} \neq \mathcal{G}_{\geq}^{m-1} \text{ or } \|\mathbf{u}_{\mathbf{k}}^{m} - \mathbf{u}_{\mathbf{k}}^{m-1}\|_{\infty} > \delta_{\epsilon}\right]}_{\text{only for Elliptic problem}} \text{ or } \underbrace{[t_m < t_{\text{end}}]}_{\substack{\text{only for} \\ \text{time evolution} \\ \text{problem}}} \right\} \right\}$

  request $\mathcal{M}_{p,r\neq p}^{S+A}$ for migration
  perform forward wavelet transform for each component of $\mathbf{u}_{\mathbf{k}}^{m}$
  for $\forall \mathsf{p} = 0:1:\mathsf{n_p}-1$
    for all levels $j = J:-1:1$
      create a mask $\mathcal{M}_{p,p}^{S}$ for $|d_{\mathbf{l}}^{\mu,j}| \geq \epsilon$
    end
    $\mathcal{M}_{p,p}^{S} \xrightarrow{\text{A}} \mathcal{M}_{p,r}^{S+A}$, $r = 0, \cdots, \mathsf{n_p}-1$
    synchronize mask: $\mathcal{M}_{p,r\neq p}^{S+A}$ send to r processor: $\mathcal{M}_{r,r}^{S+A} = \bigcup_{p=0}^{\mathsf{n_p}-1} \mathcal{M}_{p,r}^{S+A}$
    perform the reconstruction check procedure: $\mathcal{M}_{p,p}^{S+A} \xrightarrow{\text{RCP}} \mathcal{M}_{p,r}^{S+A}$
    add ghost mask: $\mathcal{M}_{p,p}^{S+A} \xrightarrow{\bigoplus_{j=1}^{J} \mathcal{D}_{p}^{j}} \mathcal{M}_{p,r}^{S+A+G}$. $\mathcal{M}_{p,r}^{S} \subset \mathcal{M}_{p,r}^{S+A} \subset \mathcal{M}_{p,r}^{S+A+G}$
  end
  if miss-balanced
    domain-**repartitioning** and **migration** of trees
    clean $\mathcal{M}_{p,r\neq p}^{S+A} = \varnothing$ and $\mathcal{M}_{p,r\neq p}^{S} = \varnothing$
    perform the reconstruction check procedure: $\mathcal{M}_{p,p}^{S+A} \xrightarrow{\text{RCP}} \mathcal{M}_{p,r}^{S+A}$
  end if
  for $\forall \mathsf{p} = 0:1:\mathsf{n_p}-1$
    construct $\mathcal{G}_{\geq}^{m+1}$
    if $\mathcal{G}_{\geq}^{m+1} \neq \mathcal{G}_{\geq}^{m}$
      interpolate $\mathbf{u}_{\mathbf{k}}^{m}$ to $\mathcal{G}_{\geq}^{m+1}$
    end if
  end
  Either **Solve** the Elliptic problem (using Local Multilevel Elliptic Solver)
  or **Advance** in Time (using Krylov/RK Time-Integration)
  $m = m+1$
end

5.9 Scalability Studies

The studies of the code scalability have been performed for the CVS (thresholding-factor ϵ= 0.2) of linearly forced (C_f= 6.$\bar{6}$) homogeneous turbulence at $Re_\lambda = 70, 120, 190, 320$ on an adaptive grid corresponding to 256^3, 512^3, 1024^3, and 2048^3 (at the highest level of resolution) using geometric sequential partitioning (fixed partitioning) as well as Zoltan hypergraph partitioning, Figures 5.10 – 5.13. These figures represents the speedup based on the CPU-time for the main time-integration loop of the code. The scalability studies confirm that parallel code even without dynamic load balancing is scalable with the speedup monotonically increasing with approximately the same slope (nearly linearly scalable up to a certain number of processors depending on the resolution), but then saturates.

For geometric partitioning, the saturation occurs mainly because of spatial intermittency of turbulent flows resulting in highly non-uniform and imbalanced distribution of grid-points among processors.

The standard deviation (stdv), the bound of (mean+stdv) and (mean-stdv), as well as bound of min and max of the the number of active wavelets ($\mathfrak{D} = \mathfrak{D}_{\mathrm{SA}}$: number of significant+adjacent points) on each rank present the miss-balance of the data-partitioning. It is evident, Figures 5.14 and 5.15, that all of these three measures are decreasing by increase of number of ranks at regardless of the resolution. This decrease is also even more clear by the time-average of the min, max, and mean of the number of active wavelets, Figures 5.16 and 5.17. This implies that the miss-balance has been improved by increasing number of processors. While number of active wavelets represents the cost of the wavelet-transform, the number of SAG (significant+adjacent+ghost) points, which are used for derivatives calculations, is a better measure of the overall computational time since as mentioned in Algorithm 3, the number of SAG points is in general greater than the number of active wavelets: $\mathcal{M}_{p,r}^{S} \subset \mathcal{M}_{p,r}^{S+A} \subset \mathcal{M}_{p,r}^{S+A+G}$. That is to say, the overall cost is proportional to $\mathfrak{D}_{\mathrm{SAG}} \log \mathfrak{D}_{\mathrm{SAG}}$ instead of $\mathfrak{D} \log \mathfrak{D}$. Thus, it is required to ensure that the number of SAG points are also well-balanced across all processors; the time-average of the min, max, and mean of $\mathfrak{D}_{\mathrm{SAG}}$

(number of SAG points) also show an improvement of the miss-balance by increasing number of processors, Figures 5.18 and 5.19. All in all, scrutinizing the miss-balance of both significant and SAG points clarify that miss-balance has been improved by increasing number of processors and it reveals that the source of the saturation is not due to the miss-balance.

The remaining possible factors are communication, data-base search algorithms, and the wavelet transform algorithm. The default implemented communication mechanism for all presented results is an all-to-all communication method in which the send-receive buffers are communicated via MPI All-to-All commands. It is well known that the all-to-all communications cost increase significantly by increase of the buffer size and total number of ranks. In our application, by increasing the Re_λ, i.e. increasing the resolution, indeed the buffer zone of each rank enlarges and results in very big send-receive buffers. That is why the first guess for the second cause of the saturation after miss-balance is the all-to-all communications. The speedup based on parallel communication, Figure 5.20, on 2048^3 indicates that for large resolution and large number-of-processors, i.e. very large communication buffer size, the saturation due to all-to-all communication is evident and daunting. It should be noted that even for this parallel algorithm, one cannot expect speedup based on communication-cost since the buffer-size and consequently the communication cost is increasing by increase of number of ranks; so, as long as, the "speedup based on parallel communication" is even constant or is slightly decreasing, it can be claimed that there is no significant problem with the communication procedure. However, on 2048^3, Figure 5.20 has shown a slowdown of approximately $\frac{89}{0.198} \cong 450$ times while increasing number of processors by a factor of 2. Therefore, a one-to-one communication mechanism has been implemented and tested: results indicate approximately the same speedup slope as the all-to-all approach and saturation was observed at about the same number of processors as all-to-all case; however, there is a very significant improvement in the slowdown, Figure 5.21. This indicates the inevitable need of one-to-one communications on large number-of-processors, where all-to-all buffer will for sure saturates.

The untouched slope and saturation at about the same number of ranks proves that the real cause of the saturation regardless of the resolution is the not just the communication technique

itself. As mentioned above, in the AWCM algorithm, by increasing the resolution, the buffer zone of each rank enlarges in other words, the ratio of number of points in the boundary zone to the internal points is increasing as number-of-processors increases. Figures 5.22 and 5.23 denote that size of boundary zone is increasing as number of rank increases and as a result, communication buffer size will be larger. Therefore, there is not much that can be done to reduce the buffer zone and the communication cost.

In the current asynchronous wavelet-transform algorithm, all ranks have to wait until the communication is complete among all processors. This is true regardless of all-to-all or one-to-one communication, i.e. even in one-to-one case, there is barrier at the end of communication. Perhaps, the size of the buffer-zone and resulting very large send-receive buffers cannot be reduced; therefore, even more smart one-to-one communication techniques will not be able to reduce the communication wall-time significantly though by removing the barrier other operations can be performed at the same time. A number of alternative algorithms to speedup the wavelet transform are proposed, which are under investigation for future development. For instance, one small change in the wavelet-transform can postpone the saturation to many times more number-of-processors: as mentioned before, in the current asynchronous algorithm, all ranks should wait for the communication until each rank can start the wavelet transform on its corresponding mask $\mathcal{M}_{p,r}^{S+A}$; however, each rank indeed can perform the wavelet transform on a subset of $\mathcal{M}_{p,p}^{S+A}$ – which does not require any point form $\mathcal{M}_{p,r\neq p}^{S+A}$ – at the same time the communication is executing. As soon as the migration of $\mathcal{M}_{p,r\neq p}^{S+A}$ to each rank is completed then the rank can continue transforming on the rest of $\mathcal{M}_{p,r}^{S+A}$. This removes the barrier on the wavelet transform while migration is occurring and it ensures that the wavelet transform engine is not idle during the migration. This technique while postponing the saturation to a very large number-of-processors, will perhaps result in no or small improvement in the speedup slope.

It is also imperative to note that all addressed speedup investigations here are indeed results of strong-scalability, where the resolution is kept constant while number of processors is increasing. Once again, the buffer zone enlarges as the number of ranks increases, i.e. the ratio of number

of SAG (significant+adjacent+ghost) points in the boundary zone $\mathfrak{D}_{\mathrm{SAG_B}}$ to the internal SAG points $\mathfrak{D}_{\mathrm{SAG_I}}$ is increasing as number-of-processors increases. Consequently, for each resolution there will be a theoretical limit for the maximum optimal number-of-processors after which the ratio of $\frac{\mathfrak{D}_{\mathrm{SAG_B}}}{\mathfrak{D}_{\mathrm{SAG_I}}}$ is very large and no speedup can be gained any more. This implies that within the context of the strong scalability, one can not except speedup for any number-of-processor regardless of the communication algorithm, wavelet-transform algorithm, and the data-structure efficiency. It must be also noted that the weak scalability is not straightforward to perform for AWCM due to the dynamically adaptive evolution of the grid, which makes it very challenging to maintain constant number-of-active-wavelets per rank for the same number-of-processors, while the resolution is changing.

Figure 5.24 that combines all strong-scalability plots presented before into one, indicates an approximately the same formal speedup slope for all resolutions up to a moderate number of processors where the effect of communication is insignificant and the InfiniBand network can be assumed to be smart enough to handle the communication load efficiently. That is to say, the observed formal slope, which is somehow resolution independent, should be close to the theoretical efficiency based on zero communication cost. Therefore, it is of great importance to find an estimate for this asymptotic slope. As explain earlier, the most expensive part of the current algorithm is the derivatives and as a result the overall computational cost is proportional to the number SAG points. In the serial case, there is no boundary zone; so, the overall computational cost scales as the number of SAG points inside the domain, $\mathfrak{D}_{\mathrm{SAG_{I_{serial}}}}$. In parallel, the the overall computational cost scales as the total number of SAG points (both internal and boundary zone SAG points), $\langle \mathfrak{D}_{\mathrm{SAG_I}} \rangle + \langle \mathfrak{D}_{\mathrm{SAG_B}} \rangle$, where $\langle \mathfrak{D}_{\mathrm{SAG_I}} \rangle$ is assumed to be the volume average of number of internal SAG points across all processors and the $\langle \mathfrak{D}_{\mathrm{SAG_B}} \rangle$ is the volume average of number of boundary-zone SAG points across all processors. It is evident that for a well-balanced partitioning, $\mathfrak{D}_{\mathrm{SAG_{I_{serial}}}} \cong \mathsf{n_p} \langle \mathfrak{D}_{\mathrm{SAG_I}} \rangle$. The parallel efficiency is basically defined as the ratio of the computational cost in serial to the parallel:

$$\text{Parallel}_{\text{Efficiency}} = \eta_{\mathsf{p}} \cong \frac{\mathsf{n}_{\mathsf{p}} \langle \Omega_{\text{SAG}_\text{I}} \rangle}{\langle \Omega_{\text{SAG}_\text{I}} \rangle + \langle \Omega_{\text{SAG}_\text{B}} \rangle} = \frac{\mathsf{n}_{\mathsf{p}}}{1 + \frac{\langle \Omega_{\text{SAG}_\text{B}} \rangle}{\langle \Omega_{\text{SAG}_\text{I}} \rangle}}. \tag{5.10}$$

Therefore, once an asymptotic approximation for $\frac{\langle \Omega_{\text{SAG}_\text{B}} \rangle}{\langle \Omega_{\text{SAG}_\text{I}} \rangle}$ is obtained then the theoretical parallel efficiency can be estimated. However, evaluating this asymptotic ratio is not straightforward for the real nonadaptive simulations. Hence, the actual value of $\overline{\left(\frac{\langle \Omega_{\text{SAG}_\text{B}} \rangle}{\langle \Omega_{\text{SAG}_\text{I}} \rangle} \right)}$, e.g. the time-average of the statistics demonstrated in Figure 5.23, is used to estimate the theoretical parallel efficiency as illustrated in Figure 5.25 for 2048^3 CVS. A very good agreement between η_{p} and the actual speedup is observed for the moderate number of processors up to 512 CPU cores. At 1024 CPU cores, the improvement by one-to-one communication is close to the theoretical efficiency and hence any more improvement in parallel communication should not increase the speedup significantly. Although, at 2048 CPU cores, a factor of two increase in the speedup can be expected by means of further enhancement of the parallel communication, which remains for the future investigations. It worth stressing again that in the theoretical efficiency, the cost associated parallel communication is not taken into account, i.e. η_{p} assumes zero wall-time for parallel communication.

Another factor affecting the overall efficiency of the algorithm in both serial and parallel is the search algorithm of the tree-structure database, which currently initiates the search from the very beginning of each tree-root for each call. A smart search algorithm, which will inherit the access point and search path of the previous call, has been proposed. This idea is under investigation to construct an algorithm to achieve the smallest possible number of calls to and the lowest possible time-spent within the database search/access functions. It is believed that a factor of at least two times speedup can be achieved, which is the subject of future effort.

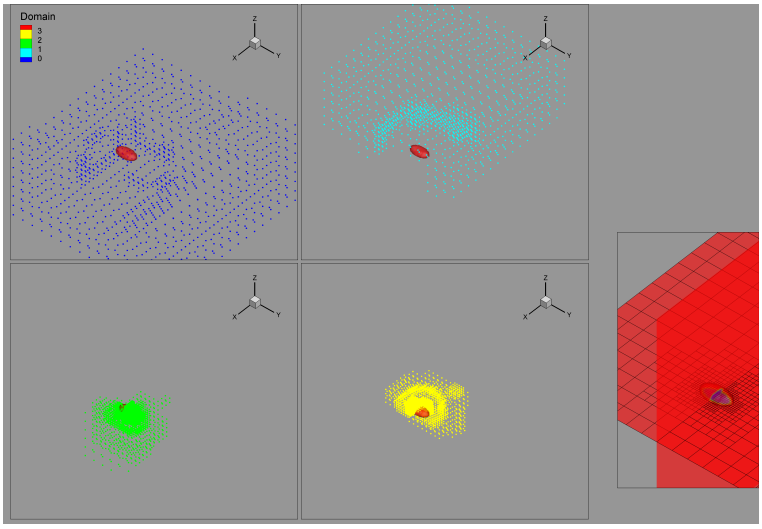

Figure 5.8: Dynamic load balancing using Zoltan hypergraph domain partitioning for Convection-Diffusion of rotating ellipsoids.

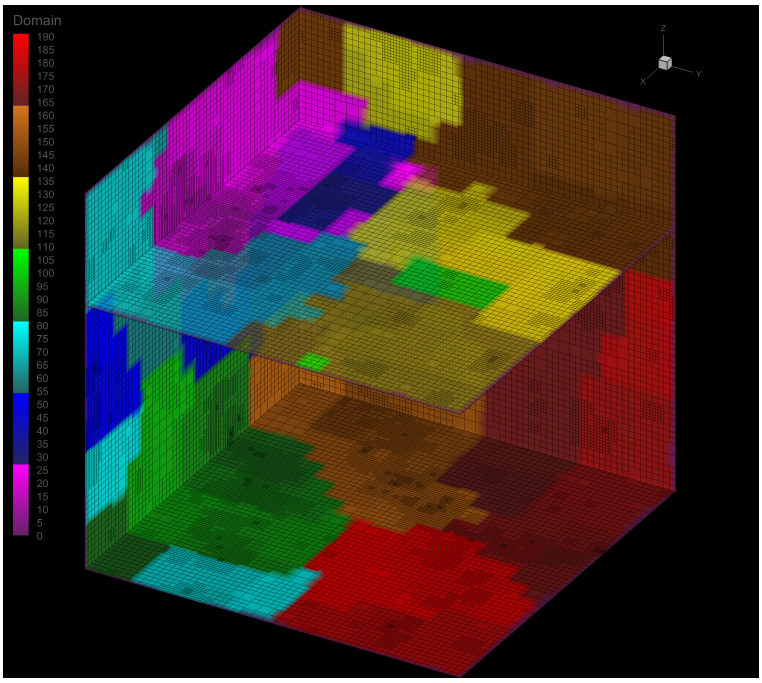

Figure 5.9: Dynamic load balancing using Zoltan hypergraph domain partitioning for SCALES on 2048^3 at $Re_\lambda = 320$.

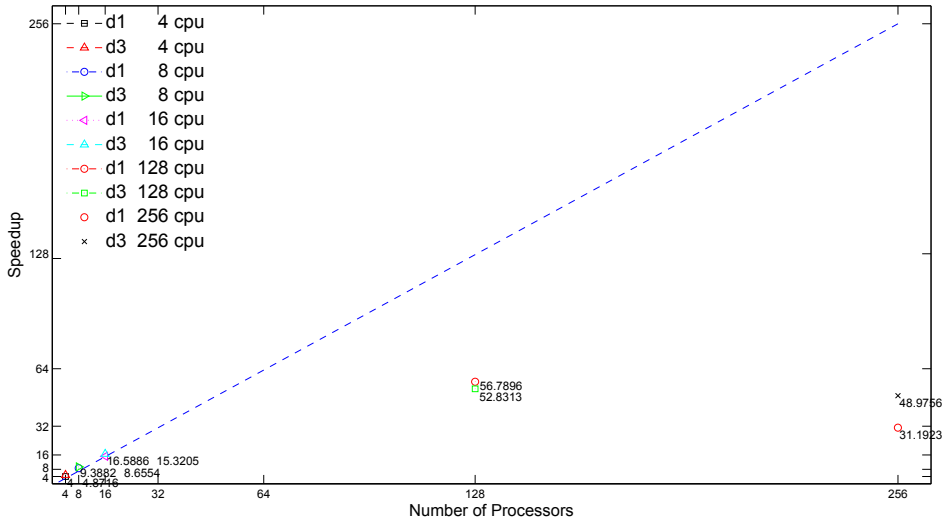

Figure 5.10: Parallel speedup for CVS $\epsilon = 0.2$ $\nu = 0.09$ $C_f = 6.\bar{6}$ $Re_\lambda = 70$ 256^3 using geometric sequential (d1) and Zoltan hypergraph partitioning (d3).

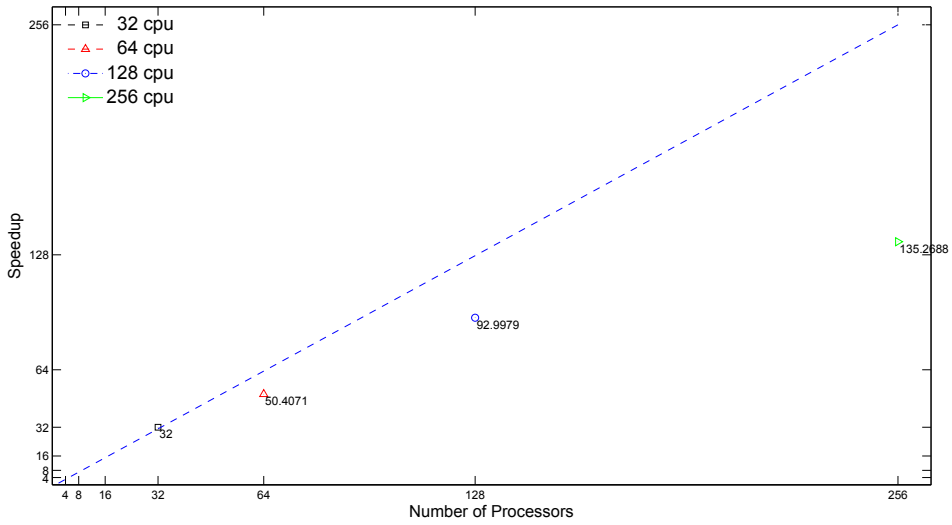

Figure 5.11: Parallel speedup for CVS $\epsilon = 0.2$ $\nu = 0.035$ $C_f = 6.\bar{6}$ $Re_\lambda = 120$ 512^3 using Zoltan hypergraph partitioning.

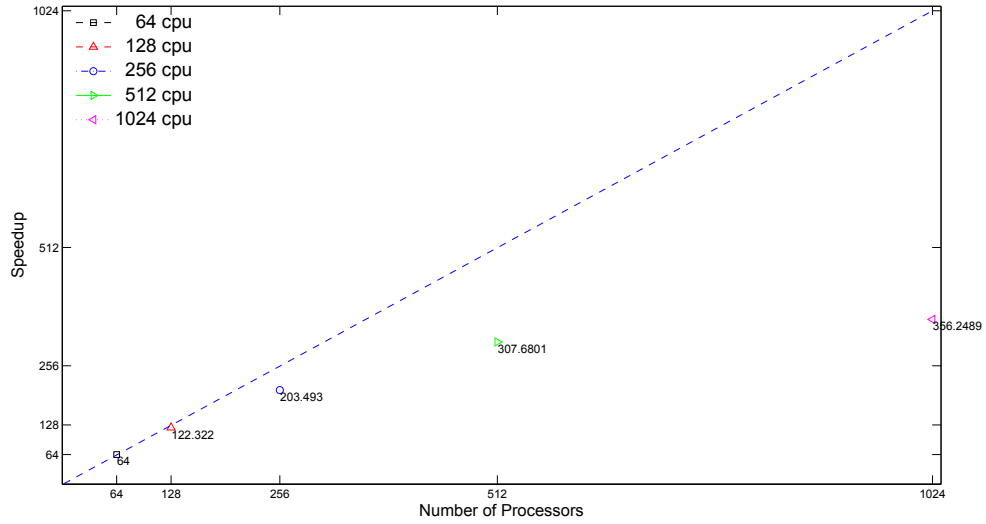

Figure 5.12: Parallel speedup for CVS $\epsilon = 0.2$ $\nu = 0.015$ $C_f = 6.\bar{6}$ $Re_\lambda = 190$ 1024^3 using Zoltan hypergraph partitioning.

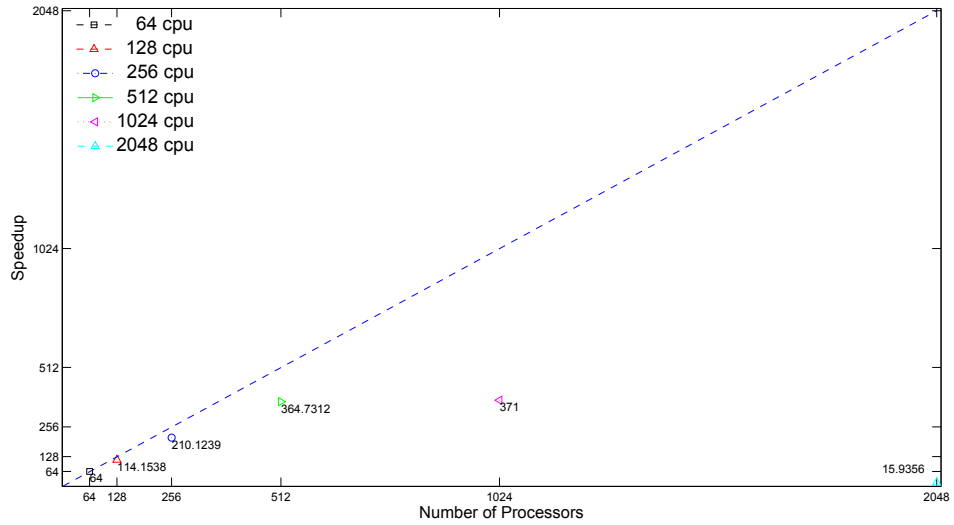

Figure 5.13: Parallel speedup for CVS $\epsilon = 0.2$ $\nu = 0.006$ $C_f = 6.\bar{6}$ $Re_\lambda = 320$ 2048^3 using Zoltan hypergraph partitioning.

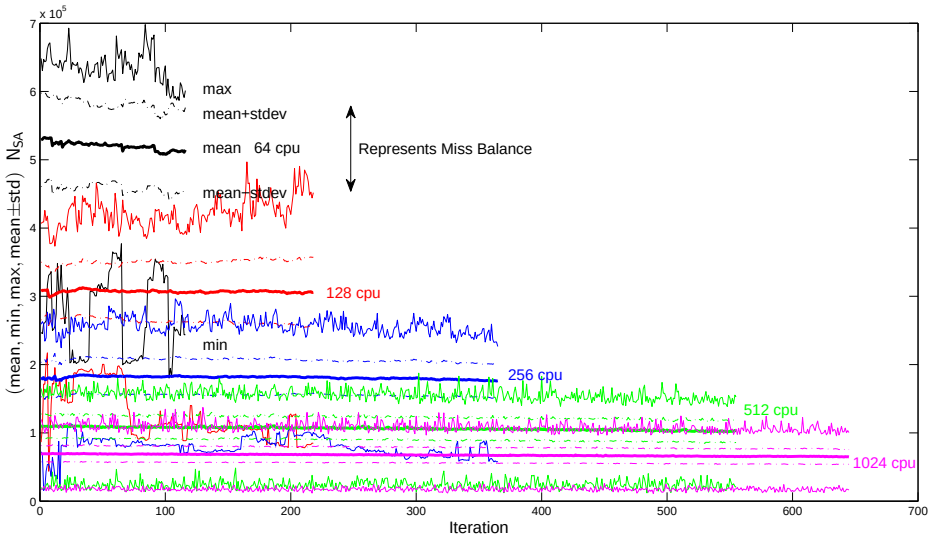

Figure 5.14: Statistics (Minimum,Mean,Maximum,Mean±stdv) of $\mathfrak{N}_{SA}$ (active wavelets) for CVS $\epsilon = 0.2$ $\nu = 0.015$ $C_f = 6.\bar{6}$ $Re_\lambda = 190$ 1024^3 using Zoltan hypergraph partitioning.

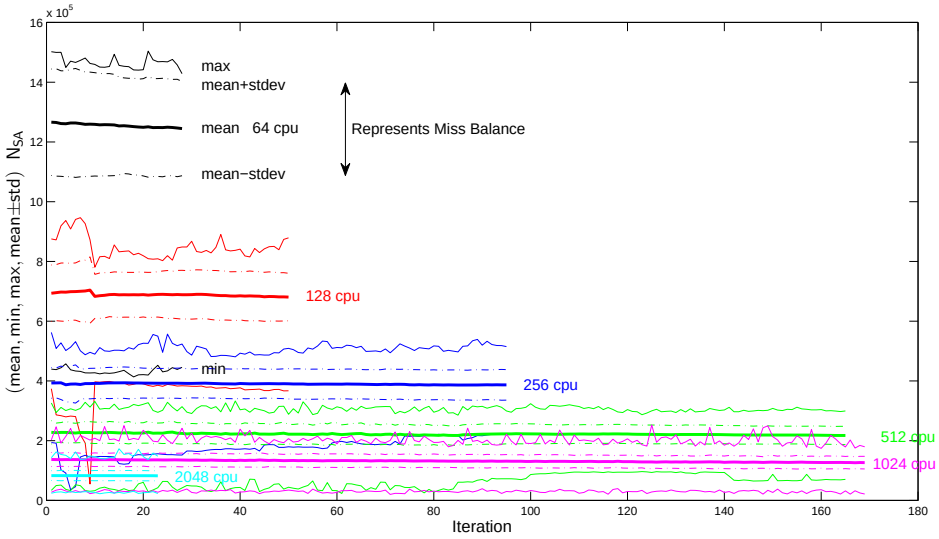

Figure 5.15: Statistics (Minimum,Mean,Maximum,Mean±stdv) of $\mathfrak{N}_{SA}$ (active wavelets) for CVS $\epsilon = 0.2$ $\nu = 0.006$ $C_f = 6.\bar{6}$ $Re_\lambda = 320$ 2048^3 using Zoltan hypergraph partitioning.

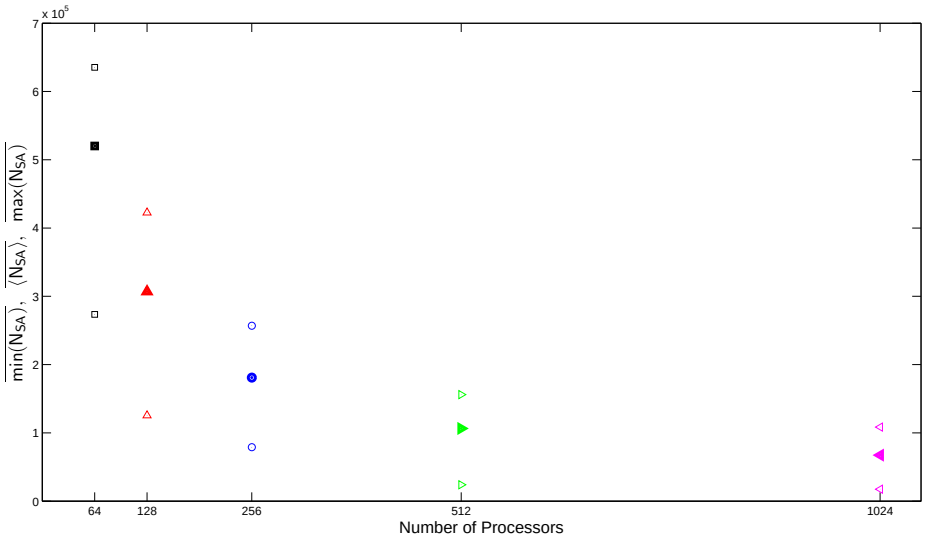

Figure 5.16: Statistics of $\overline{\min(\mathfrak{I}_{\mathrm{SA}})}$, $\overline{\max(\mathfrak{I}_{\mathrm{SA}})}$, and $\overline{\langle \mathfrak{I}_{\mathrm{SA}} \rangle}$ for CVS $\epsilon = 0.2$ $\nu = 0.015$ $\mathrm{C_f} = 6.\bar{6}$ $\mathrm{Re}_\lambda = 190$ 1024^3 using Zoltan hypergraph partitioning.

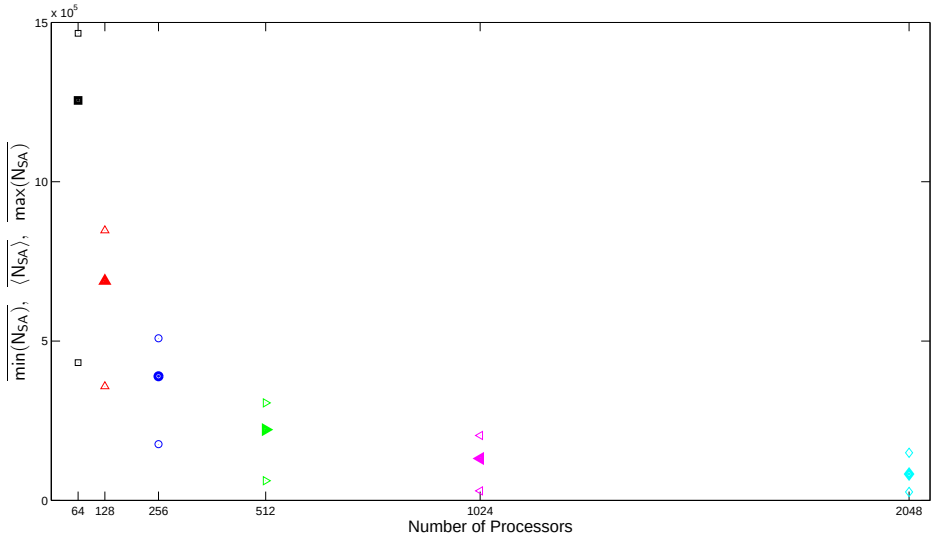

Figure 5.17: Statistics of $\overline{\min(\mathfrak{I}_{\mathrm{SA}})}$, $\overline{\max(\mathfrak{I}_{\mathrm{SA}})}$, and $\overline{\langle \mathfrak{I}_{\mathrm{SA}} \rangle}$ for CVS $\epsilon = 0.2$ $\nu = 0.006$ $\mathrm{C_f} = 6.\bar{6}$ $\mathrm{Re}_\lambda = 320$ 2048^3 using Zoltan hypergraph partitioning.

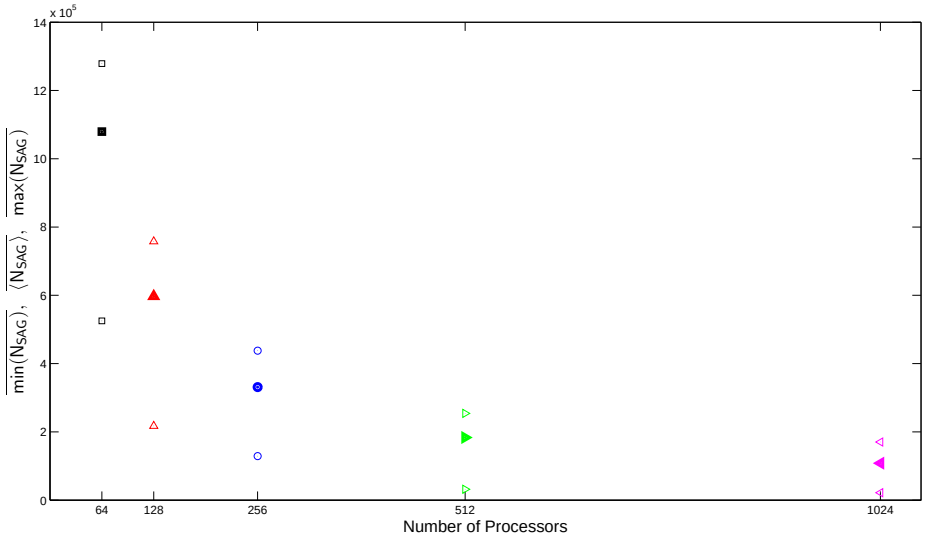

Figure 5.18: Statistics of $\overline{\min(\mathfrak{I}_{\mathrm{SAG}})}$, $\overline{\max(\mathfrak{I}_{\mathrm{SAG}})}$, and $\overline{\langle \mathfrak{I}_{\mathrm{SAG}} \rangle}$ for CVS $\epsilon = 0.2$ $\nu = 0.015$ $\mathrm{C_f} = 6.\bar{6}$ $\mathrm{Re}_\lambda = 190$ 1024^3 using Zoltan hypergraph partitioning.

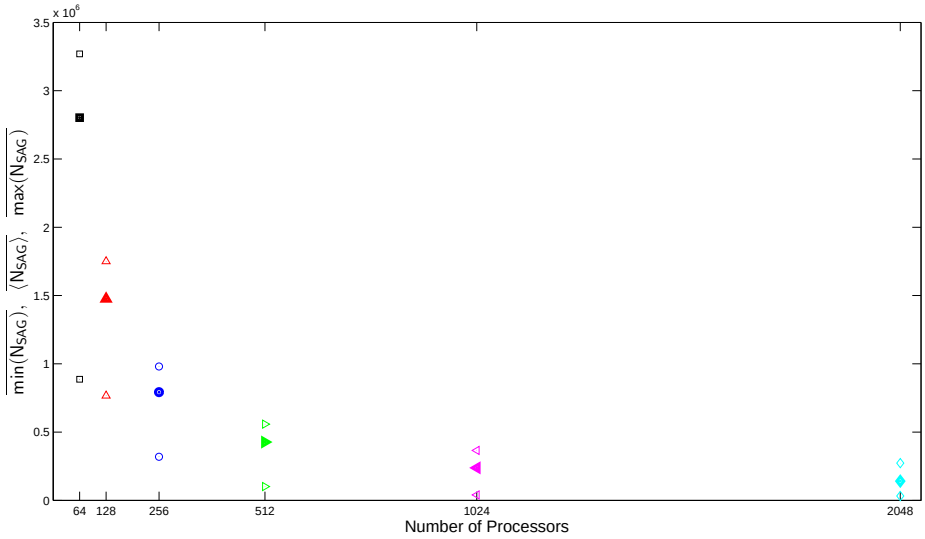

Figure 5.19: Statistics of $\overline{\min(\mathfrak{I}_{\mathrm{SAG}})}$, $\overline{\max(\mathfrak{I}_{\mathrm{SAG}})}$, and $\overline{\langle \mathfrak{I}_{\mathrm{SAG}} \rangle}$ for CVS $\epsilon = 0.2$ $\nu = 0.006$ $\mathrm{C_f} = 6.\bar{6}$ $\mathrm{Re}_\lambda = 320$ 2048^3 using Zoltan hypergraph partitioning.

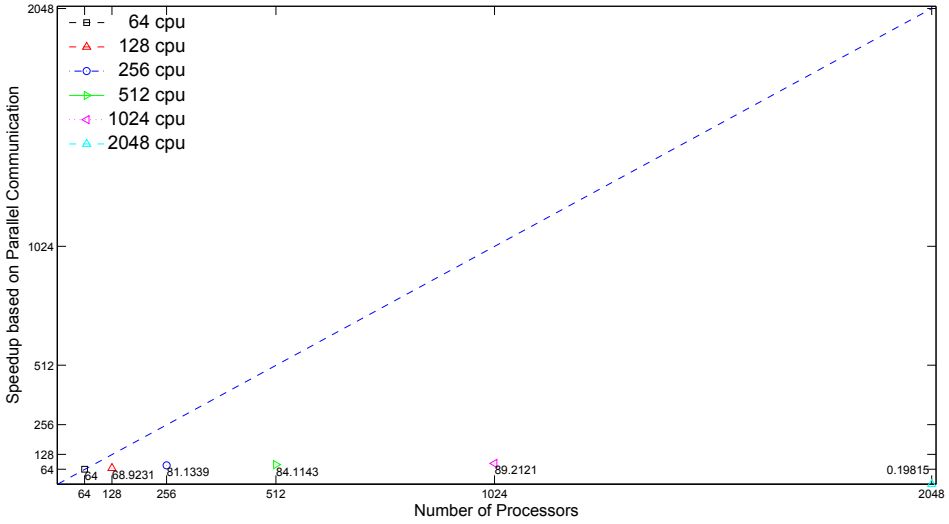

Figure 5.20: Parallel speedup for CVS $\epsilon = 0.2$ $\nu = 0.006$ $C_f = 6.\bar{6}$ $Re_\lambda = 320$ 2048^3 using Zoltan hypergraph partitioning based on parallel communications.

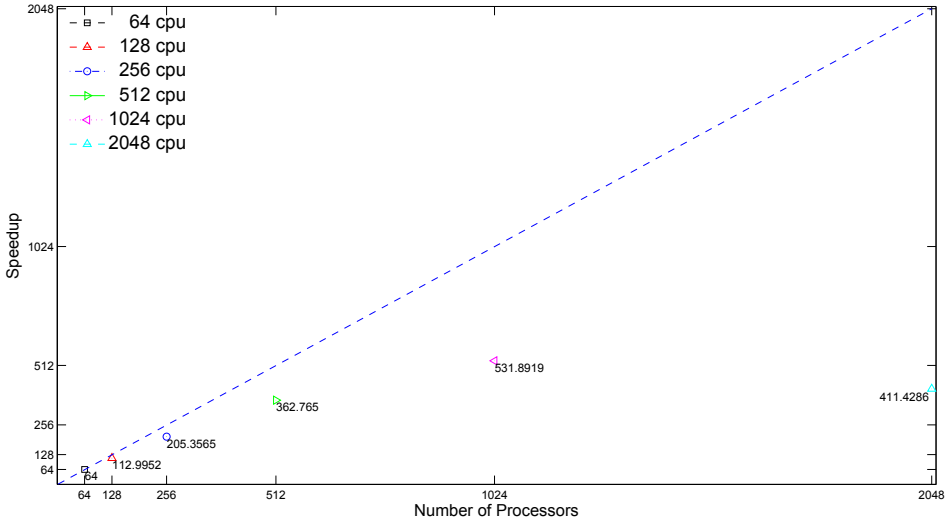

Figure 5.21: Parallel speedup for CVS $\epsilon = 0.2$ $\nu = 0.006$ $C_f = 6.\bar{6}$ $Re_\lambda = 320$ 2048^3 using Zoltan hypergraph partitioning with one-to-one communication.

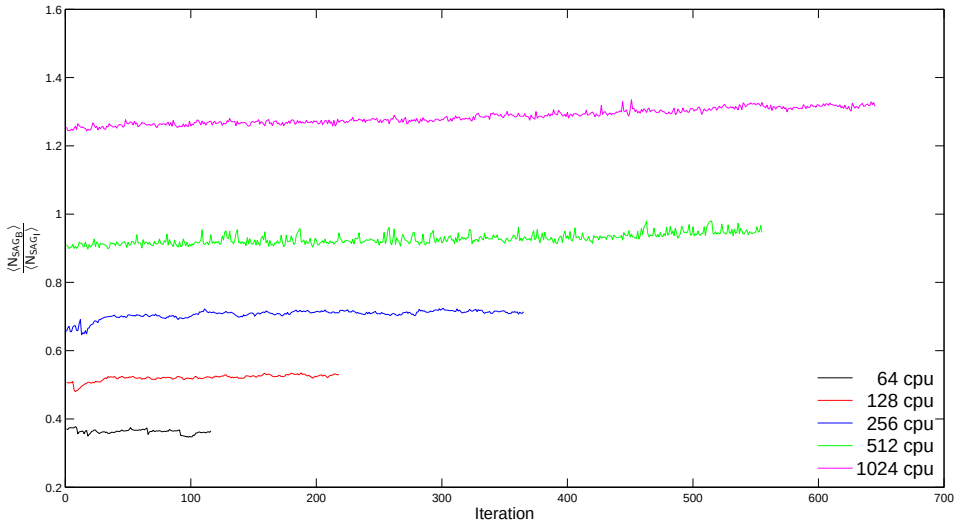

Figure 5.22: Ratio of number of SAG points in the boundary zone to the internal ghost points, $\frac{\langle \mathfrak{D}_{\mathrm{SAG_B}} \rangle}{\langle \mathfrak{D}_{\mathrm{SAG_I}} \rangle}$, for CVS $\epsilon = 0.2$ $\nu = 0.015$ $C_f = 6.\bar{6}$ $Re_\lambda = 190$ 1024^3 using Zoltan hypergraph partitioning.

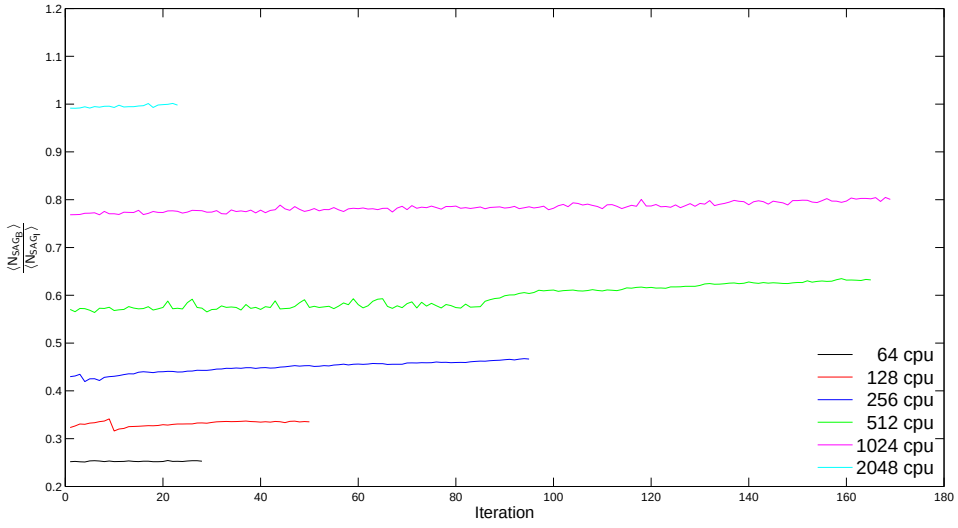

Figure 5.23: Ratio of number of SAG points in the boundary zone to the internal ghost points, $\frac{\langle \mathfrak{D}_{\mathrm{SAG_B}} \rangle}{\langle \mathfrak{D}_{\mathrm{SAG_I}} \rangle}$, for CVS $\epsilon = 0.2$ $\nu = 0.006$ $C_f = 6.\bar{6}$ $Re_\lambda = 320$ 2048^3 using Zoltan hypergraph partitioning.

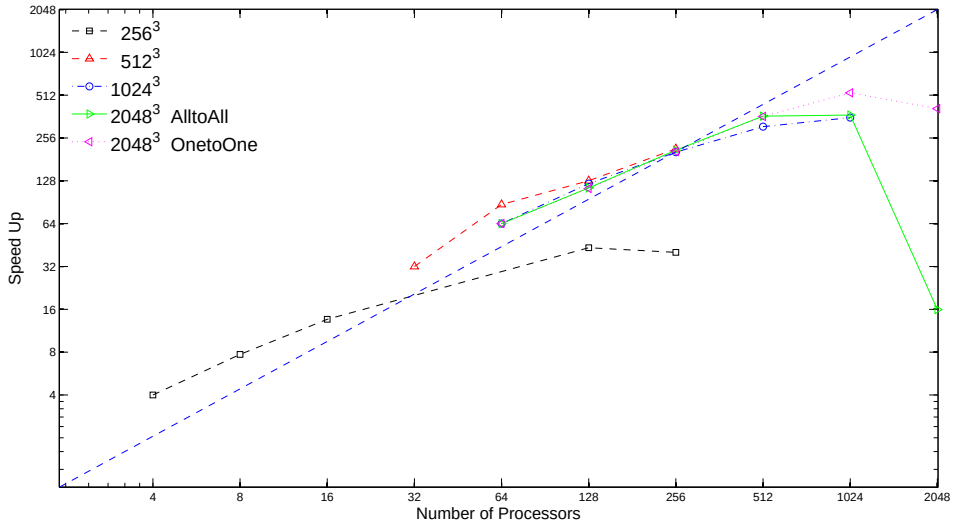

Figure 5.24: Comparison of parallel speedup for CVS on 256^3, 512^3, 1024^3, and 2048^3 using Zoltan hypergraph, ϵ= 0.2 ν= 0.006 C_f= $6.\bar{6}$ Re_λ= 320.

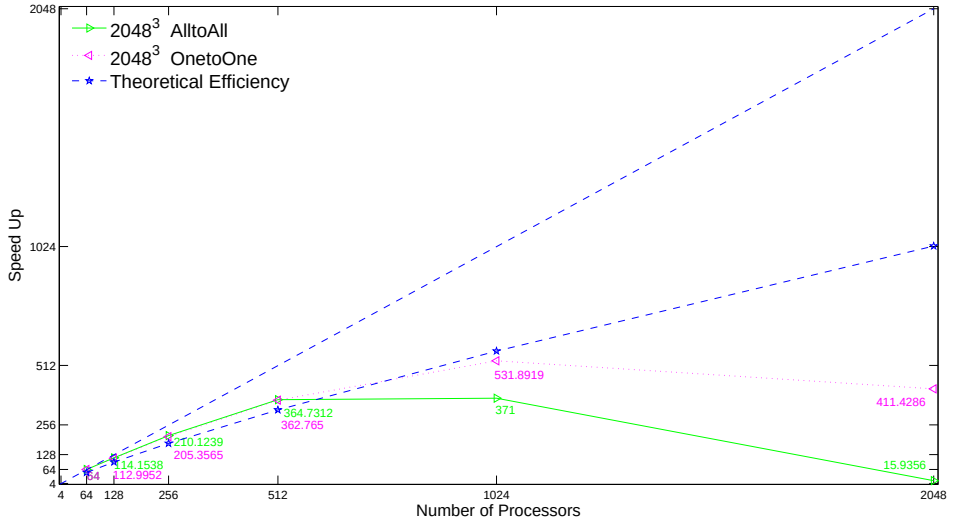

Figure 5.25: Comparison of theoretical and actual parallel speedup for CVS on 2048^3 using Zoltan hypergraph, ϵ= 0.2 ν= 0.006 C_f= $6.\bar{6}$ Re_λ= 320.

Chapter 6

Computational Complexity of CVS and SCALES

Direct Numerical Simulation (DNS) [17], despite four decades of its existence, still remains only a tool for turbulence research [34], since it is virtually impossible to resolve all the physically meaningful scales within the limit of continuum mechanics from integral length scale L (the characteristic length-scale of the physical domain) all the way down to the smallest dissipative Kolmogorov length scale η. This daunting range of spatial scales that increases with Reynolds number, $\frac{L}{\eta} \approx Re^{3/4}$, implies an enormous computational complexity for spatial modes that scales like $Re^{9/4}$ or $Re_\lambda^{9/2}$ in terms of Taylor microscale Reynolds number. Thus, total number of floating-point operations (considering both spatial and temporal modes) scales like Re^3. For instance, for typical aeronautical applications where Re is at least of the order of few millions, DNS requires more than 10^{18} number of operations making it impractical for real flow applications, at least until quantum computers become a reality.

However, this scaling is too pessimistic, since the bounds neglect spatial and temporal intermittency [27]. In reality, the turbulent flows are highly intermittent and active degrees of freedom (DOFs) extend over many "limited" number of scales. As a result, turbulent structures can be uniquely determined by a finite number of spatial modes at each time [16, 21, 27]. On the other hand, according to recent observations by Yakhot and Sreenivasan [48], if the strongest and rarest fluctuations are resolved then intermittency may indeed increase the number of required DOFs. Based on their studies, total number of operations (space-time DOFs) scales like Re^4 instead of Re^3; however, once again, their investigation was performed on a uniform computational grid and

they commented that the space-time DOFs could in fact be smaller than Re^3 if only the "interesting" parts of the flow were resolved.

Large Eddy Simulation (LES), despite its success in modeling flows of engineering interest [e.g., 33, 38], does not address these challenges, mainly because the computational affordability is achieved by modeling the effect of high wavenumbers and not resolving the small-scale physics. On the other hand, marginally resolved LES, where the ratio of SGS and resolved dissipations is relatively small, scales similarly to DNS, $Re_\lambda^{9/2}$, mainly because the requirement of resolving most of the dissipation results in the filter width close to the actual peak of energy dissipation.

Thus, the only feasible alternative in the quest for methodologies that capture interesting/important physics of high Reynolds number turbulent flows is the use of adaptive numerical approaches that can extract only the essential DOFs in order to make such simulations feasible for practical design purposes. Wavelet-based multi-resolution variable fidelity schemes for simulations of turbulence [40] are great candidates for resolving highly intermittent turbulent flows, decomposing turbulent flow into deterministic coherent and stochastic incoherent structures, and extracting energetic structures.

The compression accomplished by wavelets has been proved by the existing efforts using CVS and SCALES and it is widely believed and accepted within the turbulence community; however, no work has yet proposed exactly how the number of active wavelets (DOFs) scales as Reynolds number increases. The only available Reynolds scaling statistics of wavelet-based methods is for 2-D decaying turbulence by Kevlahan et al. [27] who presented the scaling of this kind of flow using a space-time adaptive WDNS technique in order to take into account both spatial and temporal intermittency. That is to say, prior to this work, it was unknown how quantitatively the wavelet-based multi-resolution techniques improve the Reynolds scaling of spatial modes in DNS.

Hence, this study for the first time, attains the Reynolds scaling of the number of active spatial modes in 3-D linearly forced homogeneous turbulence – i.e. by taking into account the spatial intermittency – using both CVS and SCALES. It should be emphasized that in addition to the wavelet compression, known as the most prominent strength of wavelets in turbulence, the capability

of CVS and SCALES in controlling the desired flow-physics information to-be-modeled is even more unique. The wavelet based methods in general, and SCALES in particular, offer techniques to not only achieve high compression but more importantly to control the physical phenomena, which is desired to be captured. Therefore, this work is not just presenting the Reynolds scaling of the CVS and SCALES but it is an attempt to prove how wavelet based methods can resolve more flow-physics yet using profoundly smaller number of spatial modes.

As discussed in Chapter 4, this work refers to CVS in velocity-pressure formulation, i.e. this velocity-pressure based CVS and SCALES both solve the wavelet-threshold filtered Navier-Stokes equations without and with SGS models respectively though at different threshold levels. Unlike the original CVS where the ideal threshold can be calculated based on the variance of the incoherent modes, in this velocity-based CVS, the optimal threshold should be found by numerical experiment.

6.1 Reynolds Scaling Case Study

To construct the Reynolds scaling statistics, a series of simulations where the Reynolds number is progressively increased are performed. The CVS and SCALES of linearly forced homogeneous turbulence [6] with linear forcing constant coefficient $Q = 6.66667$ are performed in the computational domain of $[0, 2\pi]^3$ on an adaptive grid with the base grid size of $\mathbf{M} = [m_x, m_y, m_z] = [8, 8, 8]$, which is dyadically refined/coarsened as needed such that the effective spatial grid resolution would be $\mathbf{M}2^{j-1}$ at the j level of resolution where the coarsest (minimum) level of the resolution is 2 and the highest level of resolution is 6,7,8,9. These correspond to adaptive grids with nonadaptive effective resolutions of 256^3, 512^3, 1024^3, and 2048^3 at Taylor micro-scale Reynolds number of $Re_\lambda \cong 72, 120, 190, 320$ based on viscosities of $\nu = 0.09, 0.035, 0.015, 0.006$. These choices of viscosity are based on maintaining the ratio of Kolmogorov length-scale to the smallest grid-spacing constant, i.e. $\frac{\eta}{\Delta_{\min}} = 2$, to ensure the resolution adequate for a well-resolved DNS (analogous to the spectral DNS). This implies that by doubling the effective resolution the viscosity should be decreased by a factor of $2^{4/3}$ ($\Delta_{\min} \sim \mathfrak{D}_{1D}{}^{-1}$, $\eta \sim \nu^{3/4}$, $\Delta_{\min} \sim \eta \Rightarrow \nu \sim \mathfrak{D}_{1D}{}^{-4/3}$), since in linearly forced homogeneous turbulence $\frac{\varepsilon}{\kappa}$ is kept constant.

6.2 Results

The broad objective of the present study is to understand better the scaling of the number of spatial modes as a function of Reynolds number and the fidelity of the model, i.e. to estimate the exponent α in the relation, $\mathfrak{D} \sim Re^{\alpha}$, where $\mathfrak{D}$ is the number of spatial computational degrees of freedom of the turbulence. In order to quantify the model fidelity, it is useful to define "turbulence resolution", the quantity that measures the level to which one would like to resolve the most energetic/dynamically important structures of turbulence. As explained in Chapter 3, turbulence resolution, can be quantified differently. One way to define turbulence resolution is to use a ratio of sub grid scale and total turbulent kinetic energies, i.e. $\frac{k_{\text{sgs}}}{k_{\text{res}}+k_{\text{sgs}}}$, where k_{res} is the resolved turbulent kinetic energy and k_{sgs} is the SGS kinetic energy. However, since the energy spectrum decays with the increase of wave numbers, the SGS kinetic energy characterization of turbulence is not well suited for high Reynolds number flows, simply because it is mostly based on large-scale contribution and is not sensitive to the Reynolds number changes. The SGS dissipation characterization, on the

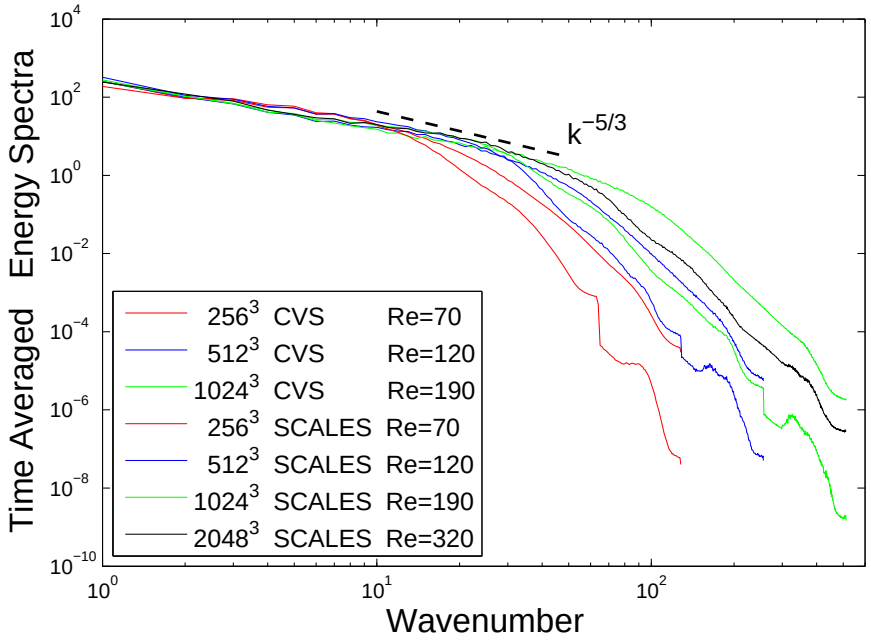

Figure 6.1: Energy spectra for CVS and SCALES at four different Reynolds numbers.

other hand, is a more objective measure, since dissipation spectrum increases with the wavenumber and the changes in molecular viscosity and correspondingly Reynolds number would result in shifting the peak of the resolved dissipation. Moreover, the SGS dissipation can also be related to enstrophy. For that reason, analogous to Chapter 4, the turbulence resolution is measured by the ratio of dissipations rather than the ratio of kinetic energies of modeled and resolved structures, i.e. by means of the local fraction of SGS dissipation, $\mathcal{F} = \frac{\Pi}{\varepsilon_{\text{res}}+\Pi}$ ($\varepsilon_{\text{res}} = 2\nu\,\overline{S}_{ij}^{>\epsilon}\,\overline{S}_{ij}^{>\epsilon}$, $\Pi = -\tau_{ij}^{*}\,\overline{S}_{ij}^{>\epsilon}$).

In the light of this broad objective, the CVS and SCALES simulations are first performed with constant threshold levels $\epsilon = 0.2,\ 0.43$ respectively, which are set to based on earlier works on 256^3 turbulent simulations [24, 25]. The performed simulations demonstrate consistency with $K^{-5/3}$ for the energy-spectra in particular at larger Reynolds number, where the inertial range is more pronounced, Figure 6.1. The vorticity magnitude and the adaptive computational mesh for SCALES simulations are illustrated in Figure 6.2. It is evident that how sparse is the adaptive grid of SCALES while it is able to resolve the energy-containing structures with such low number of spatial modes. The fixed scale for all vorticity field volume-rendered images, shows the augmentation of vorticity magnitude while the the Reynolds number increases. The number of active wavelets ($\mathfrak{D}$) and the time-average of "fraction of volume-averaged SGS dissipation (total FSGSD)" are listed in Table 6.1. Similar to Chapter 4, total FSGSD is defined as $\langle\mathcal{F}\rangle = \frac{\langle\Pi\rangle}{\langle\varepsilon_{\text{res}}\rangle+\langle\Pi\rangle}$, where $\langle\Pi\rangle = \langle -\tau_{ij}^{*}\,\overline{S}_{ij}^{>\epsilon}\rangle$ and $\langle\varepsilon_{\text{res}}\rangle = 2\nu\langle\,\overline{S}_{ij}^{>\epsilon}\,\overline{S}_{ij}^{>\epsilon}\rangle$.

Method	Re_λ	Resolution ($\mathfrak{D}_{\max}$)	$\overline{\langle\mathcal{F}\rangle}$	$\mathfrak{D}$
CVS	70	256^3	-	1 100 000
CVS	120	512^3	-	5 000 000
CVS	190	1024^3	-	20 000 000
CVS	320	2048^3	-	90 000 000
SCALES	70	256^3	0.323178	115 000
SCALES	120	512^3	0.475869	437 000
SCALES	190	1024^3	0.594733	1 000 000
SCALES	320	2048^3	0.745060	1 850 000

Table 6.1: Reference Parameters

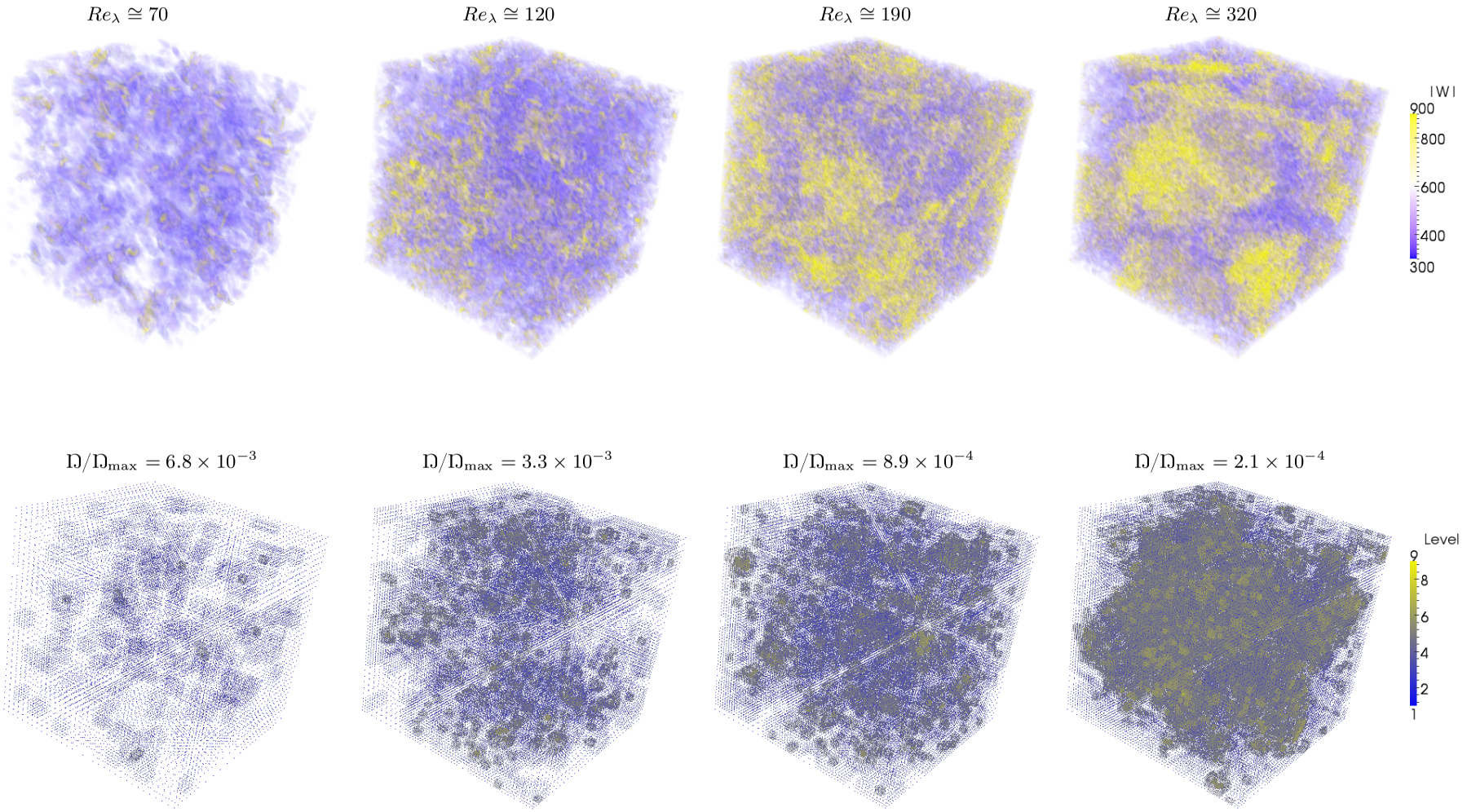

Figure 6.2: Vorticity magnitude and the adaptive computational mesh for SCALES of linearly forced homogeneous turbulence on effective non-adaptive resolutions of 256^3, 512^3, 1024^3, 2048^3 at $Re_\lambda \cong 72, 120, 190, 320$.

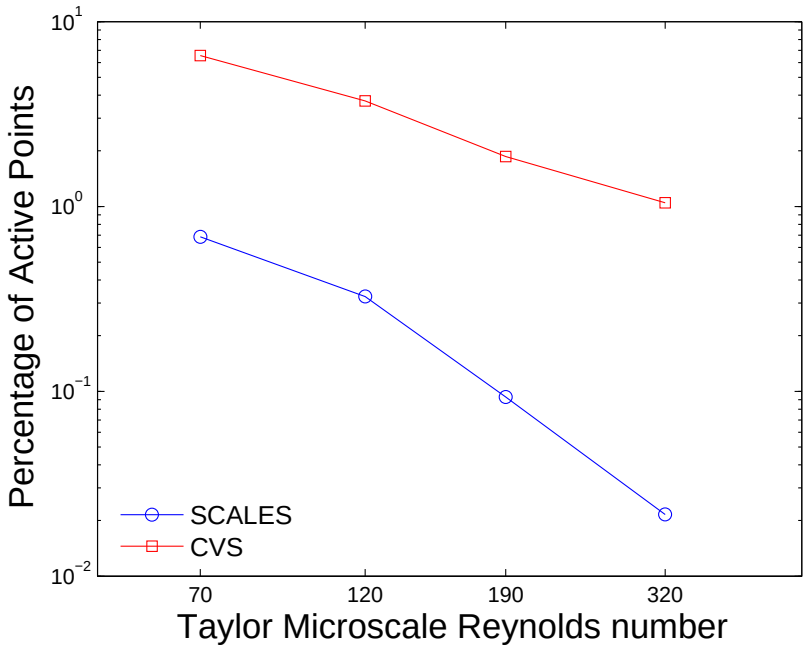

Figure 6.3: Percentage of active wavelets, $\mathfrak{N}/\mathfrak{N}_{\max}$, for CVS and SCALES with constant-threshold.

Figure 6.3 illustrates the percentage of active wavelets, which is $\mathfrak{N}$ divided by the corresponding nonadaptive effective resolution, $\mathfrak{N}_{\max}$. It is evident that the percentage of active spatial modes even decreased as Reynolds number increases; the compression ratio is increasing as Reynolds increases, which makes SCALES even more appealing for high Reynolds number flows. The computational complexity can be seen from the Re scaling presented in Figure 6.4, which includes the DNS scaling as well. This study demonstrates that the spatial modes for CVS and SCALES scale slower than $Re_\lambda^{3.25}$ and $Re_\lambda^{2.75}$ respectively, which compared with DNS scaling of $Re_\lambda^{9/2}$ implies $4.5 - 3.25 = 1.25$ and $4.5 - 2.75 = 1.75$ times smaller Reynolds scaling exponent.

It is important to emphasize, that both in CVS and SCALES, the scaling deviates from the constant slope as Reynolds increases. In SCALES, the main reason for this deviation is the increase of $\mathcal{F}$, reported in Figure 6.5. This implies that as Re_λ increases, the fidelity of the simulations decreases and the flow is relatively less resolved since the threshold-level was kept constant. The choice of $\epsilon = 0.43$ [24] was based on optimum threshold for 256^3 simulation that is the maximum threshold at which SCALES matches the $\text{CVS}_{\epsilon_{\text{opt}}}$ spectra up to inertial range. Therefore, using the

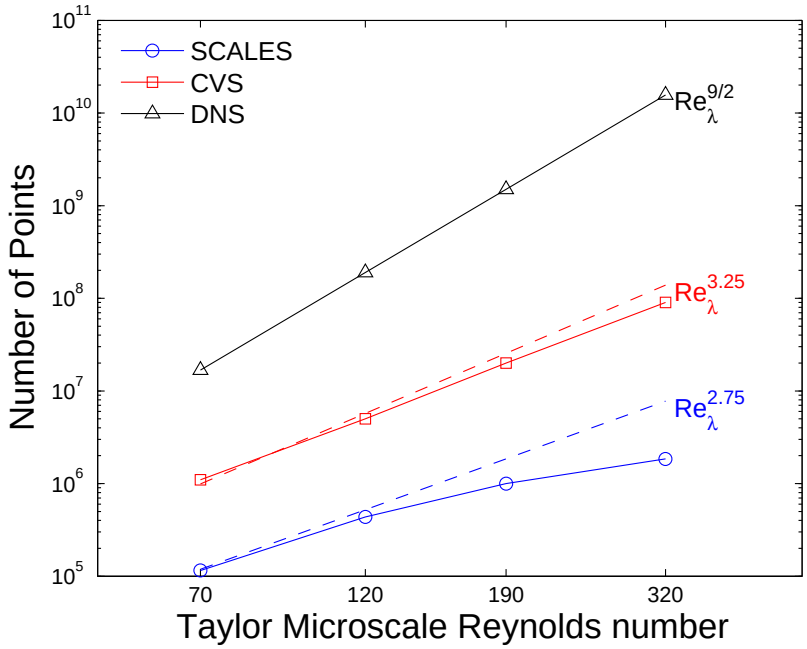

Figure 6.4: Reynolds scaling of CVS and SCALES with constant-threshold.

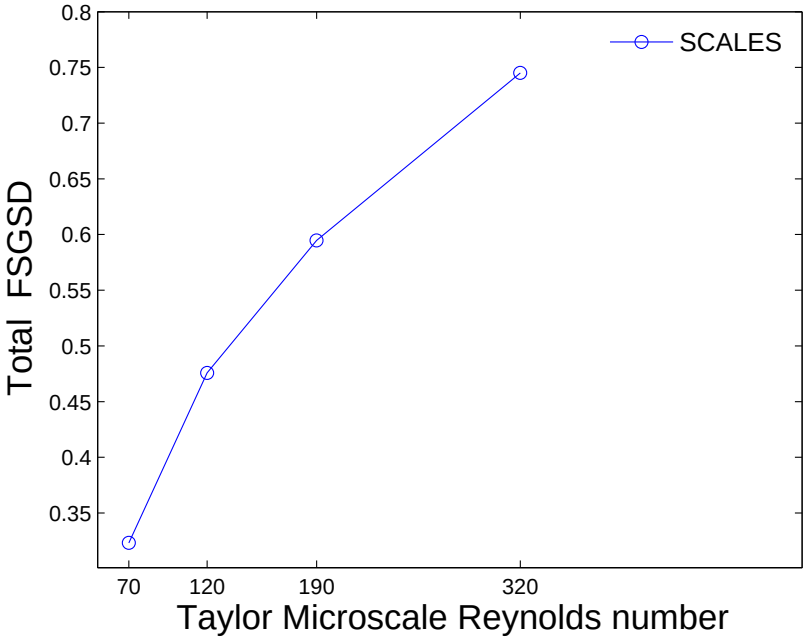

Figure 6.5: Time-average of "fraction of volume-averaged SGS dissipation", $\overline{\langle \mathcal{F} \rangle} = \overline{\left(\frac{\langle \Pi \rangle}{\langle \varepsilon_{\text{res}} \rangle + \langle \Pi \rangle} \right)}$, for constant-threshold SCALES.

same threshold for larger Re_λ implies that the level of resolving the velocity field and consequently kinetic energy would be constant. In other words, the percentage of resolved kinetic energy is kept constant by using the same threshold value. As indicated at the begging of this section, the kinetic energy characterization of turbulence resolution is not well suited for high Reynolds number flows, because the kinetic energy classification is mainly based on the large-scale contribution and is not sensitive to the Reynolds number variations. Thus, the curve for SCALES with constant thresholding will eventually flatten out with further increase of Reynolds number.

It must be noted that the performed CVS with constant threshold value $\epsilon = 0.2$ on resolutions larger than 256^3 indeed are not the true CVS, mainly because it corresponds to the optimal threshold value for 256^3 case reported by Goldstein and Vasilyev [24], Goldstein et al. [25]. As explained before, the true CVS uses an optimal threshold to ensure that the unresolved field is the Gaussian white noise and as a result its effect on the resolved field can be ignored. The use of larger threshold value result in additional mode truncation that removes the energy for the resolved field and, thus, acts as dissipative mechanism. This dissipation is responsible for slowing down of the scaling curve. Since the current study is based on velocity-pressure formulation of CVS, in order to find optimal threshold value for CVS, one would need to conduct similar numerical experiments as in [24], therefore, performing true CVS based on the ideal/optimal threshold is not practical for large Reynolds number turbulent flows.

When studying the Reynolds scaling, it is important to maintain the fidelity of the simulations as Reynolds number changes. This can be achieved by keeping the fraction of the SGS dissipation, $\mathcal{F}$, constant, which would in turn ensure that the percentage of resolved dissipation or the turbulence resolution is approximately the same. Therefore, variable thresholding is utilized to maintain a constant level for $\mathcal{F}$. Both time varying [7] and spatially variable thresholding [35] approaches, are used to maintain $\mathcal{F}$ for all Re_λ at the average value of $\mathcal{F}$ corresponding to the $Re_\lambda = 70$, i.e. $\mathcal{G} = \overline{\langle \mathcal{F} \rangle}_{256^3 \text{ with } \epsilon=0.43} \cong 0.32$, where $\mathcal{G}$ stands for the desired goal value for $\mathcal{F}$. Time varying thresholding was used only for $Re_\lambda = 70, 120$ and spatially variable thresholding was utilized for $Re_\lambda = 70, 120, 190, 320$. For $Re_\lambda = 70, 120, 190$ the spatially variable thresholding using

first-order interpolation along characteristics was performed. While for $Re_\lambda = 320$, the spatially variable thresholding methodology, by directly solving the Lagrangian Path-Line Diffusive Averaging equation of threshold with diffusion coefficient of $\nu_\epsilon = 0.1$, was exploited. The results of both time and spatial variable thresholding are consistent and reported in Figure 6.6. Contrary to constant thresholding SCALES where the slope of Reynolds scaling was reducing, SCALES with this variable thresholding results in approximately constant slope. Comparison of percentage of number of active wavelets using spatially variable thresholding with constant thresholding as well as CVS is illustrated in Figure 6.7. It is important to discuss the fundamental difference between constant turbulence resolution Reynolds scaling of SCALES with Reynolds scaling of marginally resolved LES, discussed earlier. Substantial decrease of the scaling exponent is a strong indication of the effective utilization of spatial intermittency by SCALES, contrasted to nearly DNS scaling of $Re_\lambda^{9/2}$ of marginally resolved LES.

In order to study the influence of the fidelity of simulation on the Reynolds scaling of SCALES, a series of simulations of different turbulence resolution is conducted. The different fidelity is achieved by using spatially variable thresholding approach with different goal values of $\mathcal{F}$, namely $\mathcal{G} = 0.2, 0.25, 0.4, 0.5$ (Figure 6.8).[1] It is observed that in the logarithmic scale the slope of Re_λ scaling of SCALES spatial modes at least up to 1024^3 remains nearly the same while changing the level of turbulence resolution, Figure 6.9. In other words, the Reynolds scaling of constant-dissipation SCALES at different fidelity levels are parallel lines in the logarithmic scale. The percentage of active spatial modes initially either increases slightly or remains approximately constant as Reynolds number increases though eventually reduces similar to the constant-thresholding case, Figure 6.10. Thus, it can be concluded that the compression ratio is increasing as Reynolds increases regardless of constant-kinetic-energy or constant-dissipation simulation.

The true CVS can be also seen as a coherent vortex simulation by which the enstrophy or truncation-dissipation is maintained at an approximately constant level. However, in current

[1] It should be noted that at the time of reporting these results, the simulations of 1024^3 with $\mathcal{G} = 0.25$ and 2048^3 with $\mathcal{G} = 0.32$ were still in progress; as it is clear from Figures 6.9 and 6.8, the number of active wavelets for these two cases were still growing and $\langle \mathcal{F} \rangle$ had not yet converged to the corresponding goal values.

investigation, similar to constant-threshold SCALES, the resolved kinetic energy level is kept approximately constant. Therefore, similar to performed constant-dissipation SCALES, it is planned to extend the CVS scaling based on constant-truncation-dissipation. This can be done by means of spatially variable thresholding technique, where the ratio of truncation-dissipation to the resolved-dissipation is maintained at a constant reference level. This goal value could be the corresponding ratio for 256^3 CVS with $\epsilon = 0.2$ since this threshold level was found [24, 25] as an optimal value at which the 256^3 CVS spectra (visually) matches the DNS spectra and a nearly Gaussian PDF for unresolved incoherent structures is achieved. However, It should be noted that the achieved slope for CVS Reynolds scaling is the lower bound of the true CVS since by performing the aforementioned constant-truncation-dissipation CVS, for any resolution larger than 256^3, the threshold will be for sure smaller than 0.2 by average. Besides, the constant-dissipation SCALES even at very small goal value is still requiring smaller number of spatial modes compared with the constant-threshold CVS. Thus, constant-truncation-dissipation CVS will make SCALES even more competitive.

The fractal dimension and consequently the intermittency of the active regions of the flow can be estimated analogously to the analysis of Paladin and Vulpiani [36] and Kevlahan et al. [27] who utilized the $\beta-$model of Frisch et al. [19], which shows that the spatial degrees-of-freedom of an intermittent turbulent flow should scale like $Re^{3D_F/(D_F+1)}$, where $D_F \leq 3$ is the fractal dimension of the active part of the turbulent flow. It is observed that the fractal dimension for CVS and SCALES are $D_{F_{\text{CVS}}} \lesssim \frac{13}{11}$ and $D_{F_{\text{SCALES}}} \lesssim \frac{11}{13}$ respectively. The most intriguing part about these finding is very low, close to unity fractal dimension of the energy containing structures.

Scrutinizing the SCALES results reveals that in the linear-scale instead of logarithmic-scale, the number of spatial modes for SCALES with constant threshold-level is growing linearly. This implies that the number of flow structures at a constant percentage of resolved kinetic energy is linearly increasing as Reynolds number grows, Figure 6.11. This interesting physical phenomenon demonstrates the potential of extracting new physical thoughts in turbulence through physics-based simulations of SCALES.

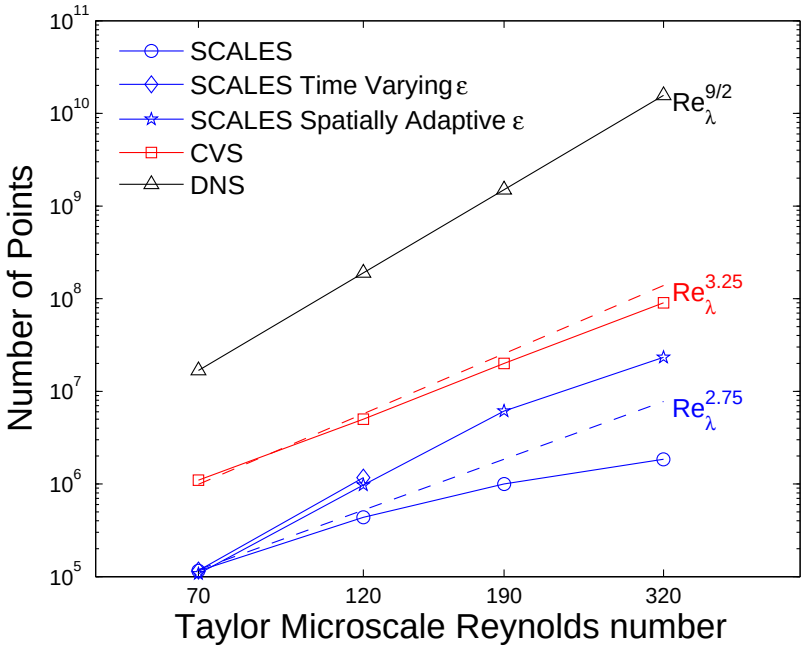

Figure 6.6: Reynolds Scaling of constant-threshold CVS, constant-threshold SCALES, as well as both time- and spatially-adaptive ϵ SCALES.

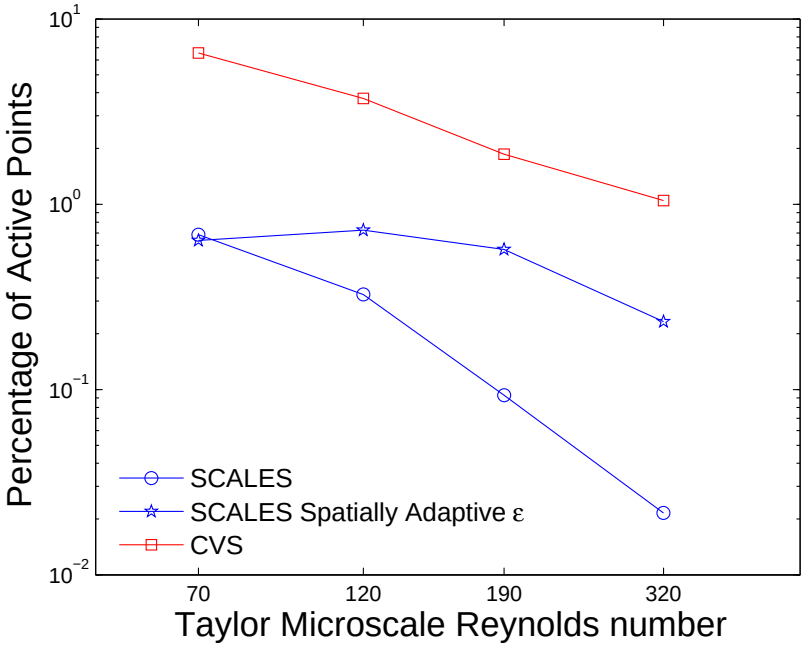

Figure 6.7: Percentage of active wavelets, $\mathfrak{D}/\mathfrak{D}_{\max}$, for constant-threshold CVS, constant-threshold SCALES, and spatially-adaptive ϵ SCALES.

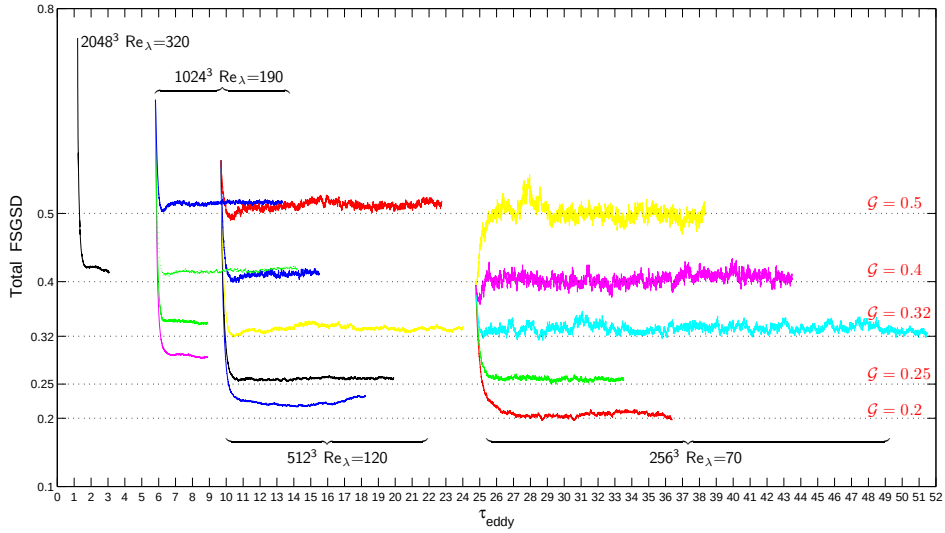

Figure 6.8: Time-history of fraction of volume-averaged SGS dissipation, $\langle \mathcal{F} \rangle$, for constant-dissipation SCALES at various goal values.

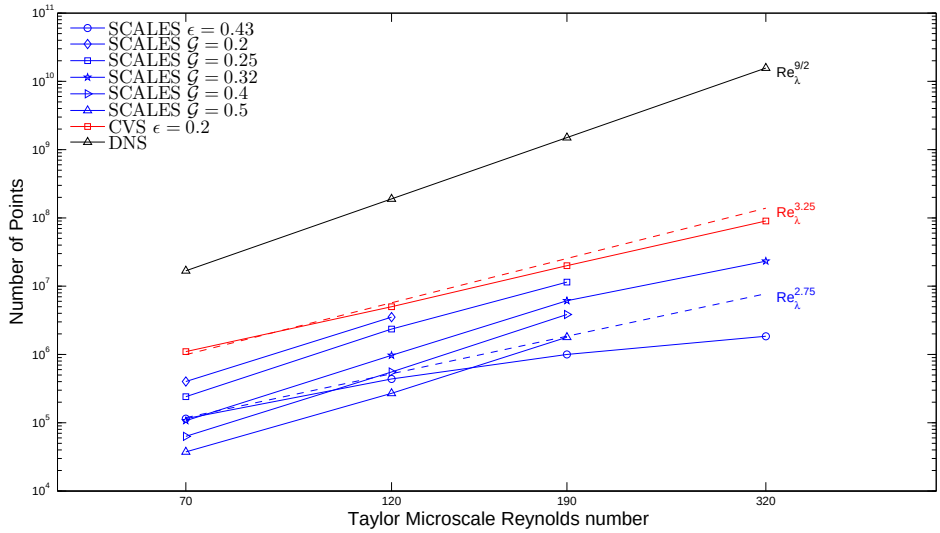

Figure 6.9: Reynolds scaling of constant-threshold CVS, constant-threshold SCALES, and constant-dissipation SCALES at various goal values.

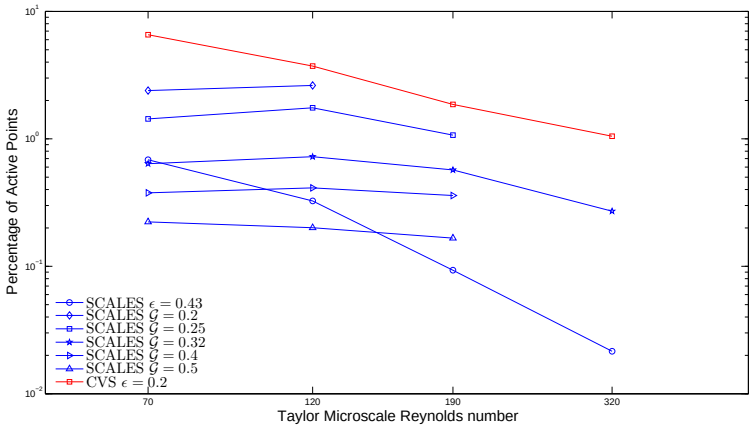

Figure 6.10: Percentage of active wavelets, $\mathfrak{D}/\mathfrak{D}_{\max}$, for constant-threshold CVS, constant-threshold SCALES, and constant-dissipation SCALES at various goal values.

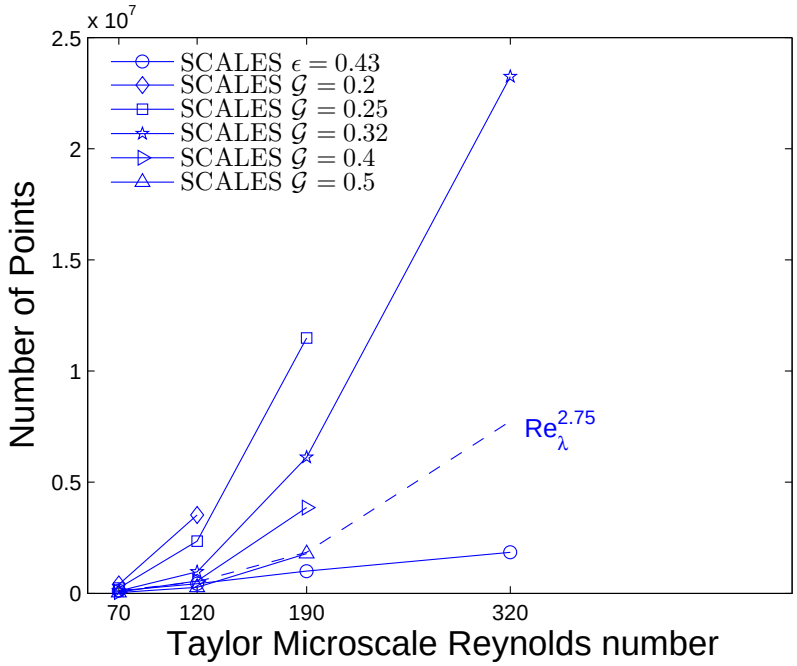

Figure 6.11: Reynolds scaling of constant-threshold CVS, constant-threshold SCALES, and constant-dissipation SCALES at various goal values in linear scale.

Chapter 7

Conclusion and Perspective

The most notable achievements throughout the course of this numerical effort can be addressed as follows:

(1) this work represents the first attempt to develop a hybrid wavelet-based multiscale adaptive variable fidelity turbulence modeling approach through the notion of spatio-temporal threshold-level for the wavelet thresholding filter;

(2) this is the first effort to present Reynolds scaling of Coherent Vortex Simulations and Adaptive Wavelet-based Large Eddy Simulations to quantitatively justify the power of the wavelet-based multi-resolution techniques, in particular the strength of SCALES in resolving high Reynolds number flows at a desired level of fidelity for any dynamically important flow characteristics with a significantly small number of spatial modes; besides

(3) the first, to the best of author's knowledge, parallel adaptive wavelet-based PDE solver, which has been under development since 2005, has been completed and extensively tested on various architectures.

The proposed "Hierarchical Multiscale Adaptive Variable Fidelity Wavelet-based Turbulence Modeling" methodology, which is based on Lagrangian Spatially Variable Thresholding, is a very robust single solver/framework for performing hybrid simulations analogous to hybrid RANS/LES/DNS. However, within this framework only one solver is utilized and challenges corresponding to overlapping multiple solvers and AMR are irrelevant.

This work materializes the very long time dream of a fully adaptive hybrid turbulence simulation using a well established wavelet-based method (SCALES). The current framework makes it possible to perform wavelet-based fully adaptive LES as well as hybrid WDNS/CVS/SCALES on very large domain and at large Reynolds numbers, with the aim of enormous compression of wavelets, e.g. 99%.

This methodology provides an automatic transition from WDNS – which resolves all flow structures via a direct solution of wavelet-filtered Navier-Stokes equations – to coherent/incoherent flow decomposition in the CVS limit to SCALES regime, where the coherent energy containing turbulent motions are resolved while the effect of less energetic coherent/incoherent motions is modeled: namely, a hierarchical space/time dynamically adaptive automatic smooth transition from resolving the Kolmogorov length-scale to decomposing deterministic-coherent/stochastic-incoherent modes to capturing more/less energetic structures. This defines a new concept of model-refinement, which is named **m**-refinement.

The performed Reynolds scaling study shows that in SCALES even with preserving a constant level of turbulence resolution while increasing the Reynolds number, required number of DOFs is still smaller than CVS and DNS for relatively large Reynolds numbers. This computational complexity study utilizes extensively the capability of the proposed spatially variable thresholding technique in order to accomplish the scaling based on constant level of SGS dissipation to the total dissipation, i.e. a constant level of turbulence resolution.

This Reynolds scaling study has also drawn two insightful physical conclusions: the fractal dimension – which provides a qualitative measure of how intermittent the turbulent flow is – in both SCALES and CVS is close to unity. A fractal dimension of slightly larger than one is observed for the coherent structures, while the fractal dimension of the energy containing structures is found to be even less than unity. Furthermore, the number of flow structures at a constant percentage of resolved kinetic energy – i.e. number of fixed-energy containing structures (energy containing structures at a fixed level of kinetic energy) – scales linearly as Reynolds number.

The perspective of proposed ideas for future progresses can be classified into eight major categories as follows:

- **Spatially Varying $\mathcal{G}$** The proposed benchmark in this work utilizes a goal value for turbulent resolution, which is varying in time. A very realistic test case is a spatial varying $\mathcal{G}$ whose immediate and best application is the hybrid full simulation of jet engines: this will be an attempt analogous to the longtime effort at Stanford University to perform hybrid RANS/LES simulation of full scale Pratt & Whitney engines. The required machinery for such simulations has been implemented; it is only required to define the realistic spatially varying mask for $\mathcal{G}$.

- **Stochastic SGS Models** As discussed in Chapter 1, in the current implementation of the SCALES methodology, only the effect of the "minority deterministic coherent SGS modes" on the "deterministic most energetic coherent structures" are modeled by the "deterministic SGS models". However, it is of great interest to be able to model the effect of the "majority stochastic incoherent SGS modes" on the "deterministic most energetic coherent structures" as well by means of "stochastic SGS models". Hence, hereby it is proposed to perform studies toward understanding the Stochastic SGS models and their implementation within SCALES framework.

- **Uncertainty Quantification Studies** It is said that among the the future directions of the computational sciences, main concern will be uncertainties issues. Keeping this in mind, another dream is to be able to fine-tune the deterministic SGS models based on the Uncertainty Quantification (UQ) concepts. Therefore, it is envisioned to exploit possible advantages of UQ in instantaneous corrections/adjustments of the SGS models. The UQ based adjustment of the time-relaxation-parameter and forcing-term of the threshold-factor Lagrangian evolution, as well as UQ based adjustment of hybrid model transition algorithm (when/where to switch among WDNS/CVS/SCALES) are also on the wish-list for future endeavors.

- **Extension of Complexity Study to True CVS** Akin to the performed constant-dissipation SCALES, it is planned to extend the CVS scaling based on constant-truncation-dissipation. This can be done by means of spatially variable thresholding technique, where the ratio of truncation-dissipation to the resolved-dissipation is maintained at a constant reference level.

- **Extension of Complexity Study to Very High Reynolds Numbers and WDNS** Upon access to much more computational resources, this study needs to be extended to very high Reynolds number: it is possible that at higher Reynolds, at each constant goal value of turbulence resolution, i.e. at a certain $\mathcal{G}$, the slope may reduce, which would make the SCALES even more promising at high Reynolds numbers. With more computational resources, the previous scaling of 2-D WDNS also can be extended to 3-D.

- **Extension of Complexity Study to Space-Time Adaptive WDNS, CVS and SCALES in 3-D** The current effort presents Reynolds scaling of only spatial modes of 3-D linearly forced homogeneous turbulence. As addressed in Chapter 6, an existing previous effort also attained Reynolds scaling of space-time modes in 2-D only using space-time adaptive WDNS. With the framework and solver developed during this work, it is now feasible to perform the Reynolds scaling of space-time modes of 3-D linearly forced homogeneous turbulence using space-time adaptive WDNS, CVS and SCALES.

- **Parallel Solver Improvements** Even the currently developed parallel algorithm is capable of performing the largest turbulence simulation ever, which is what it has been envisioned as the last goal of the current effort. However, further improvements on the tree-structure search algorithms, the parallel wavelet-transform algorithm, and the buffer-zone communication strategies can significantly improve the efficiency and postpone the saturation up to many times more number of processors. This will make the aforementioned final goal feasible within more realistic wall-time.

- **SCALES Data Mining** The energy-containing-structures related physical phenomena observed through the Reynolds scaling study are only a glimpse of what SCALES is capable of. With the use of the developed hybrid multiscale adaptive variable fidelity method and parallel machinery, SCALES is going into its ultimate goal of data mining phase and it is anticipated that it would be able to extract very insightful new physical observations in turbulence.

Finally, in words of Marcel Lesieur [28],

> It might finally happen that this would be only a necessary transition stage toward the definition of new fluid dynamical concepts which would render obsolete and useless the complicated analytical and numerical techniques which helped create them.

Bibliography

[1] George Papanicolaou from stanford university in an interview with science watch correspondent Gary Taubes.

[2] Erik Boman, Karen Devine, Lee Ann Fisk, Robert Heaphy, Bruce Hendrickson, Vitus Leung, Courtenay Vaughan, Umit Catalyurek, Doruk Bozdag, and William Mitchell. Zoltan home page. `http://www.cs.sandia.gov/Zoltan`, 1999.

[3] Erik Boman, Karen Devine, Lee Ann Fisk, Robert Heaphy, Bruce Hendrickson, Courtenay Vaughan, Umit Catalyurek, Doruk Bozdag, William Mitchell, and James Teresco. Zoltan 3.0: Parallel Partitioning, Load-balancing, and Data Management Services; Developer's Guide. Sandia National Laboratories, Albuquerque, NM, 2007. Tech. Report SAND2007-4749W, `http://www.cs.sandia.gov/Zoltan/dev_html/dev.html`.

[4] Erik Boman, Karen Devine, Lee Ann Fisk, Robert Heaphy, Bruce Hendrickson, Courtenay Vaughan, Umit Catalyurek, Doruk Bozdag, William Mitchell, and James Teresco. Zoltan 3.0: Parallel Partitioning, Load-balancing, and Data Management Services; User's Guide. Sandia National Laboratories, Albuquerque, NM, 2007. Tech. Report SAND2007-4748W `http://www.cs.sandia.gov/Zoltan/ug_html/ug.html`.

[5] U.V. Catalyurek, E.G. Boman, K.D. Devine, D. Bozdag, R.T. Heaphy, and L.A. Riesen. Hypergraph-based dynamic load balancing for adaptive scientific computations. In Proc. of 21st International Parallel and Distributed Processing Symposium (IPDPS'07). IEEE, 2007. Best Algorithms Paper Award.

[6] Giuliano De Stefano and Oleg V. Vasilyev. Stochastic coherent adaptive large eddy simulation of forced isotropic turbulence. Journal of Fluid Mechanics, 646:453–470, 2010.

[7] Giuliano De Stefano and Oleg V. Vasilyev. A fully adaptive wavelet-based approach to homogeneous turbulence simulation. Journal of Fluid Mechanics, DOI:10.1017/jfm.2012.6, 2012.

[8] Giuliano De Stefano, Daniel E. Goldstein, and Oleg V. Vasilyev. On the role of sub-grid scale coherent modes in large eddy simulation. Journal of Fluid Mechanics, 525:263–274, 2005.

[9] Giuliano De Stefano, Oleg V. Vasilyev, and Daniel E. Goldstein. Localized dynamic kinetic-energy-based models for stochastic coherent adaptive large eddy simulation. Physics of Fluids, 20:045102.1–045102.14, 2008.

[10] J. W. Deardorff. A numerical study of three-dimensional turbulent channel flow at large reynolds numbers. Journal of Fluid Mechanics, 41(2):453–480, 1970.

[11] Karen Devine, Erik Boman, Robert Heaphy, Bruce Hendrickson, and Courtenay Vaughan. Zoltan data management services for parallel dynamic applications. Computing in Science and Engineering, 4(2):90–97, 2002.

[12] Karen D. Devine, Erik G. Boman, Robert T. Heaphy, Rob H. Bisseling, and Umit V. Catalyurek. Parallel hypergraph partitioning for scientific computing. IEEE, 2006.

[13] Marie Farge and Gabriel Rabreau. Transformee en ondelettes pour detecter et analyser les structures coherentes dans les ecoulements turbulents bidimensionnels. C. R. Academie des Sciences de Paris, serie II(307):1479–1486, 1988.

[14] Marie Farge and Kai Schneider. Coherent vortex simulation (CVS), a semi-deterministic turbulence model using wavelets. Flow, Turbulence and Combustion, 6:393–426, 2001.

[15] Marie Farge, Kai Schneider, and Nicholas K.-R. Kevlahan. Non-Gaussianity and coherent vortex simulation for two-dimensional turbulence using an adaptive orthogonal wavelet basis. Physics of Fluids, 11(8):2187–2201, 1999.

[16] C. Foias and G. Prodi. Sur le comportement global des solution non stationnaires des quations de Navier-Stokes en dimension deux. Rend. Sem. Math. Univ. Padova, 39:1–34, 1967.

[17] DG. Fox and DK. Lilly. Numerical simulation of turbulent flows. Rev. Geophys. Space. Phys., 10:51–72, 1972.

[18] Rodney O. Fox. Large-Eddy-Simulation Tools for Multiphase Flows. Annual Review of Fluid Mechanics, 44:47–76, 2012.

[19] U. Frisch, M. Nelkin, and P.-L. Sulem. A simple dynamical model of intermittent fully developed turbulence. Journal of Fluid Mechanics, 87:719–736, 1978.

[20] Jochen Fröhlich and Kai Schneider. Numerical simulation of decaying turbulence in an adaptive wavelet basis. Applied and Computational Harmonic Analysis, 3:393–397, 1996.

[21] G. P. Galdi. Determining modes, nodes and volume elements for stationary solutions of the Navier-Stokes problem past a three-dimensional body. Arch. Rat. Mech. Anal., 180:97–126, 2006.

[22] M. Germano, U. Piomelli, Parviz Moin, and W. H. Cabot. A dynamic subgrid-scale eddy viscosity model. Physics of Fluids A, 3(7):1760–1765, 1991.

[23] S. Ghosal, Thomas S. Lund, Parviz Moin, and K. Akselvoll. A dynamic localization model for large-eddy simulation of turbulent flows. Journal of Fluid Mechanics, 286:229–255, 1995.

[24] Daniel E. Goldstein and Oleg V. Vasilyev. Stochastic coherent adaptive large eddy simulation method. Physics of Fluids, 16(7):2497–2513, 2004.

[25] Daniel E. Goldstein, Oleg V. Vasilyev, and Nicholas K.-R. Kevlahan. CVS and SCALES simulation of 3D isotropic turbulence. Journal of Turbulence, 6(37):1–20, 2005.

[26] L. Jameson. A wavelet-optimized, very high order adaptive grid and order numerical method. SIAM J. Sci. Comput., 19(6):1980–2013, 1998.

[27] Nicholas K.-R. Kevlahan, Jahrul M. Alam, and Oleg V. Vasilyev. Scaling of space-time modes with Reynolds number in two-dimensional turbulence. Journal of Fluid Mechanics, 570:217–226, 2007.

[28] Marcel Lesieur. Turbulence in Fluids. 4th edition.

[29] Qianlong Liu and Oleg V. Vasilyev. Hybrid adaptive wavelet collocation-brinkman penalization method for DNS and URANS simulations of compressible flow around bluff bodies. AIAA Paper No. 2006-3206, 2006.

[30] T.S. Lundgren. Linearly forced isotropic turbulence. Annual Research Briefs, pages 461–473, 2003.

[31] Charles Meneveau and Thomas S. Lund. The dynamic smagorinsky model and scale-dependent coefficients in the viscous range of turbulence. Physics of Fluids, 9:3932, 1997.

[32] Charles Meneveau, Thomas S. Lund, and William H. Cabot. A lagrangian dynamic subgrid-scale model of turbulence. Journal of Fluid Mechanics, 319:353–385, 1996.

[33] Parviz Moin. Advances in large eddy simulation methodology of complex flows. Int. J. Heat Fluid Flow, 23:710–720, 2002.

[34] Parviz Moin and Krishnan Mahesh. Direct numerical simulation: A tool in turbulence research. Annual Review of Fluid Mechanics, 30:539–578, 1998.

[35] AliReza Nejadmalayeri, Oleg V. Vasilyev, Alexei Vezolainen, and Giuliano De Stefano. Spatially variable thresholding for stochastic coherent adaptive LES. In Hans Kuerten, Bernard Geurts, Vincenzo Armenio, and Jochen Fröhlich, editors, Proceedings of Direct and Large-Eddy Simulation Workshop 8: Eindhoven University of Technology, the Netherlands, July 7-9, 2010, pages 95–100. Springer, 2011.

[36] G. Paladin and A. Vulpiani. Degrees of freedom of turbulence. Phys. Rev. A, 35:1971–1973, 1987.

[37] J. Blair Perot and Jason Gadebusch. A self-adapting turbulence model for flow simulation at any mesh resolution. Physics of Fluids, 19(11):115105.1–115105.11, 2007.

[38] Ugo Piomelli and Elias Balaras. Wall-layer models for large-eddy simulations. Annual Review of Fluid Mechanics, 34:349–374, 2002.

[39] Heinz G. Pitsch. Large-Eddy simulation of turbulent combustion. Annual Review of Fluid Mechanics, 38:453–482, 2006.

[40] Kai Schneider and Oleg V. Vasilyev. Wavelet methods in computational fluid dynamics. Annual Review of Fluid Mechanics, 42:473–503, 2010.

[41] Joseph Smagorinsky. General circulation experiments with the primitive equations, I. The basic experiment. Monthly Weather Review, 91(3):99–164, 1963.

[42] W. Sweldens. The lifting scheme: A custom-design construction of biorthogonal wavelets. Appl. Comput. Harmon. Anal., 3(2):186–200, 1996.

[43] W. Sweldens. The lifting scheme: A construction of second generation wavelets. SIAM J. Math. Anal., 29(2):511–546, 1998.

[44] Oleg V. Vasilyev. Solving multi-dimensional evolution problems with localized structures using second generation wavelets. Int. J. Comp. Fluid Dyn., Special issue on High-Resolution Methods in Computational Fluid Dynamics, 17(2):151–168, 2003.

[45] Oleg V. Vasilyev and Christopher Bowman. Second generation wavelet collocation method for the solution of partial differential equations. Journal of Computational Physics, 165:660–693, 2000.

[46] Oleg V. Vasilyev and Nicholas K.-R. Kevlahan. An adaptive multilevel wavelet collocation method for elliptic problems. Journal of Computational Physics, 206(2):412–431, 2005.

[47] Oleg V. Vasilyev, Giuliano De Stefano, Daniel E. Goldstein, and Nicholas K.-R. Kevlahan. Lagrangian dynamic SGS model for SCALES of isotropic turbulence. Journal of Turbulence, 9(11):1–14, 2008.

[48] V. Yakhot and K. R. Sreenivasan. Anomalous scaling of structure functions and dynamic constraints on turbulence simulations. J. Stat. Phys., 121:823–841, 2005.

[49] M. Yokokawa, K. Itakura, A. Uno, T. Ishihara, and Y. Kaneda. 16.4-tflops direct numerical simulation of turbulence by a fourier spectral method on the earth simulator. Baltimore MD, 2002.